EFFECTS OF ATMOSPHERIC SCINTILLATION IN K_A-BAND SATELLITE COMMUNICATIONS

A Dissertation presented to
The Faculty of the Division of Graduate Studies

by

Scott A. Borgsmiller

In partial fulfillment of the requirements for the degree of
Doctor of Philosophy in Electrical Engineering

Georgia Institute of Technology

February 1998

EFFECTS OF ATMOSPHERIC SCINTILLATION IN K_A-BAND SATELLITE COMMUNICATIONS

Approved:

_____
Paul G. Steffes, Chairman

_____
David R. DeBoer

_____
Glenn S. Smith

Date Approved_____

ACKNOWLEDGMENTS

I would like to acknowledge some of the many people who have helped me during the course of this research. First, I would like to thank Dr. Paul G. Steffes, my thesis advisor. He gave me the opportunity to be a part of his research group and participate in the ACTS project. His guidance, support, and encouragement have been invaluable throughout the course of my doctorate program. I would also like to thank his co-investigator for the ACTS research program, Daniel Howard of the Georgia Tech Research Institute. In addition, I would like to acknowledge the efforts of the other engineers who have worked on this project: Mohamed-Slim Alouini, Mark Hoover, Jason Collins, Lewis Roberts, and Shahid Sheikh. This research has been supported in part by the NASA Lewis Research Center, under contract NAS3-27361. Additional support for my research assistantship was provided by Raytheon TI Systems of Plano, TX.

I would also like to thank my friends at Georgia Tech for making my years in Atlanta so enjoyable, including other members of Dr. Steffes' research group: David DeBoer, James Hoffman, Marc Kolodner, and Shady Suleiman. And last, but not least, I would like to thank my family, especially my wife, Karen Borgsmiller, and my parents, Richard and Nancy Borgsmiller, for their unending love and support.

TABLE OF CONTENTS

LIST OF TABLES

LIST OF FIGURES

GLOSSARY

A-D	Analog-to-Digital conversion
ACTS	Advanced Communication Technology Satellite
Az	Azimuth angle of satellite from ground station
a	Coefficient in general BER equation
B	Noise bandwidth
BER	Bit Error Rate
BERT	Bit Error Rate Tester
BPSK	Binary Phase Shift Keying
b	Coefficient in general BER equation
CDM	Code Division Multiplexing
CDMA	Code-Domain Multiple Access
C	Polar angle between ground station and subsatellite longitudes
$\mathbf{C_n}$	Structure constant for the index of refraction
D	Diameter of antenna aperture
$\mathbf{D_n(r)}$	Structure function for the refractive index fluctuation
DS	Direct Sequence
d	Distance from ground station to satellite
dB	Decibel
dBc	Decibel with respect to the carrier

dBm	Decibel with respect to one milliwatt
dBw	Decibel with respect to one watt
E_b/N_o	Ratio of energy per bit to noise power density
EDT	Eastern Daylight Time (GMT - 4 hours)
EIRP	Effective Isotropic Radiated Power
El	Elevation angle of satellite from ground station
EST	Eastern Standard Time (GMT - 5 hours)
e	Atmospheric water vapor partial pressure
erfc()	Complementary error function
FEU	Feed Enclosure Unit
FFT	Fast Fourier Transform
f	frequency
f_c	corner frequency
f_o	Fresnel frequency
G(x)	Aperture antenna scintillation averaging factor
GEO	Geostationary (or Geosynchronous) Earth Orbit
GHz	Gigahertz
GMT	Greenwich Meridian Time
G_r	Receive antenna gain
G_t	Transmit antenna gain
h	Height of turbulent layer above the ground
IF	Intermediate Frequency

ISI	Inter-Symbol Interference
Ka-band	Satellite communications band (20GHz downlink, 30GHz uplink)
k	Boltzmann constant, 1.38×10^{-23} W/K/Hz
k	Wavenumber, $2\pi/\lambda$
kHz	Kilohertz
LEO	Low Earth Orbit
LeRC	NASA Lewis Research Center, Cleveland, OH
LNA	Low Noise Amplifier
LO	Local Oscillator
L	Path length through turbulent layer
$\mathbf{L_e}$	North latitude of ground station
$\mathbf{L_g}$	Path length from ground station to turbulent layer
$\mathbf{L_o}$	Outer scale of atmospheric turbulence
$\mathbf{L_p}$	Path loss (also called spreading loss)
$\mathbf{L_s}$	North latitude of subsatellite point
$\mathbf{l_e}$	West longitude of ground station
$\mathbf{l_o}$	Inner scale of atmospheric turbulence
$\mathbf{l_s}$	West longitude of subsatellite point
Mbps	Million (or Mega) bits per second
Mcps	Million (or Mega) chips per second
MEO	Medium Earth Orbiting
MHz	megahertz

MSM	Microwave Switch Matrix
mph	miles per hour
N	refractivity
NASA	National Aeronautics and Space Administration
n	refractive index
OMT	Ortho-Mode Transducer
P	atmospheric pressure (in millibars)
PC	Personal Computer
QPSK	Quadrature Phase Shift Keying
R	Path length
RF	Radio Frequency
rad	radians
$\mathbf{r_e}$	Radius of the Earth (6370km)
$\mathbf{r_s}$	Radius of satellite orbit
S(r)	Phase function of propagating E-field
SS	Spread Spectrum
T	air temperature (in Kelvin)
T	orbital period (in seconds)
T1	data rate of 1.544Mbps
$\mathbf{T_{sys}}$	System noise temperature
TTL	Transistor-Transistor Logic
TWT	Traveling Wave Tube

VSAT	Very Small Aperture Terminal
v	mean flow velocity of atmospheric turbulence
$W_\chi^0(f)$	Scintillation amplitude spectrum; low-frequency asymptote
$W_\chi^\infty(f)$	Scintillation amplitude spectrum; high-frequency asymptote
$Ws^0(f)$	Scintillation phase spectrum; low-frequency asymptote
$Ws^\infty(f)$	Scintillation phase spectrum; high-frequency asymptote
x	Distance from ground station east to subturbulence point
y	Distance from ground station north to subturbulence point
α	Azimuth angle offset from north-south meridian
$\chi(r)$	Log-amplitude function of propagating E-field
γ	Central angle between satellite and ground station
λ	Wavelength
η	Antenna aperture efficiency
μ	Kepler's constant (3.9861×10^5 km^3/sec^2 for Earth)
σ_χ^2	Scintillation log-amplitude variance
σ_S^2	Scintillation phase variance

ABSTRACT

This research is motivated by the need to characterize the effects of atmospheric scintillation on Ka-band satellite communications. The builders of satellite communications systems are planning to utilize Ka-band in more than a dozen systems that have been proposed for launch in the next decade. The NASA ACTS (Advanced Communication Technology Satellite) program has provided a means to investigate the problems associated with Ka-band satellite transmissions. Experimental measurements have been conducted using a very small aperture terminal (VSAT) to evaluate the effects of scintillation on narrowband and wideband signals. The theoretical background of scintillation theory is presented, noting especially the additional performance degradation predicted for wideband Ka-band systems using VSATs. Experimental measurements of the amplitude and phase variations in received narrowband carrier signals were performed, using beacon signals transmitted by ACTS and carrier signals which are relayed through the satellite. Measured amplitude and phase spectra have been compared with theoretical models to establish the presence of scintillation. Measurements have also been performed on wideband spread spectrum signals which are relayed through ACTS to determine the bit-error rate degradation of the digital signal resulting from scintillation effects. The theory and measurements presented for the geostationary ACTS have then been applied to a low-earth orbiting satellite system, by extrapolating the effects of the moving propagation path on scintillation.

CHAPTER I

1. INTRODUCTION

1.1 Background and Motivation

The builders of satellite communication systems are moving toward Ka-band and other higher frequency ranges as the allocations in the traditional satellite communications bands become crowded. Ka-band systems uplink at a frequency of about 30GHz and downlink near 20GHz. More than a dozen Ka-band systems have been proposed for launch in the next decade. One inherent drawback of Ka-band satellite systems is increased signal distortion resulting from propagation effects. Atmospheric attenuation in Ka-band can be severe, especially in the presence of rain or other precipitation. Tropospheric scintillation also increases with frequency, creating fast amplitude variations and additional phase noise in the transmission. Also, scintillation is generally enhanced by smaller antenna apertures, and very small aperture terminals (VSATs) are becoming extremely popular.

Developers of many of the new Ka-band satellite systems are showing increased interest in using spread spectrum (SS) signals for channel diversity and secure communications. Spread spectrum signals are typically phase-modulated waveforms, which are susceptible to corruption in the presence of excess phase noise. Additionally, some of

the new systems plan to use low earth-orbiting (LEO) satellites. Since LEO satellites move with respect to ground-based users, the effects of scintillation are exacerbated by the motion of the propagation path through the atmosphere. These factors underscore the importance of understanding the effects of atmospheric phase scintillation in Ka-band satellite communications.

The NASA Advanced Communication Technology Satellite (ACTS) program has provided a means to investigate the problems associated with Ka-band satellite transmissions. ACTS is the first Ka-band communications satellite in geostationary earth orbit (GEO) over the western hemisphere. A diagram of the satellite identifying many of the key subsystems is shown in Figure 1.1.(1) ACTS has served as a testbed for many of the new technologies needed for Ka-band systems, such as multiple hopping antenna beams and regenerative transponders. The ACTS Propagation Experiments Program was instituted to investigate the effects of atmospheric propagation on Ka-band transmissions. Since the satellite was launched in September of 1993, an ongoing propagation research program has characterized weather-produced attenuation of the ACTS satellite beacon signals in many locales spread throughout North America. These experiments continuously monitor the amplitude of the two ACTS beacon signals to generate long-term fade statistics. Since 1994, Georgia Tech has been a participant in this program, but instead of monitoring only the beacon signal amplitude, our experiment also monitors the atmosphere-induced phase variations of one beacon signal. Our experiment has also used the satellite in a loopback mode to examine the characteristics of wideband transmissions through the 1GHz bandwidth ACTS transponder.

1.2 Research Objectives and Organization

This research has three major components. The first involves measurement of the scintillation present in a carrier wave signal received from ACTS. Two types of carrier signals are used. One is a beacon signal continuously transmitted by the satellite, the other is a carrier which originates from the Georgia Tech ACTS terminal and is relayed back through one of the satellite transponders. In both cases, the objective has been to determine the strength of the amplitude and phase scintillation under a variety of weather conditions, and to analyze how closely the observed behavior conforms to theoretical predictions.

The second component of this research has involved transmitting direct-sequence spread spectrum signals through ACTS to determine the effect of atmosphere-induced scintillation noise on digitally modulated transmissions. The bit-error rate (BER) has been measured for many different weather events to understand the effects of Ka-band scintillation on phase-modulated digital signals. The predictions of theoretical models are compared with the measured performance.

The third component of this research is the application of the measurements taken with a GEO satellite system to a LEO system environment. An analysis is presented that shows how the motion of a LEO satellite with respect to the receiving ground station will seriously exacerbate the effects of scintillation.

The remainder of this dissertation is organized as follows. Chapter 2 summarizes the theoretical background of tropospheric scintillation, and discusses the physical processes responsible for scintillation at Ka-band. The experimental hardware systems used to perform the scintillation measurements are detailed in Chapter 3. The measurements that were obtained are presented in Chapter 4. Chapter 5 contains a discussion and analysis of the scintillation effects which would be expected for a satellite in low-earth orbit. Last, the unique contributions of this work are summarized and conclusions are drawn in Chapter 6.

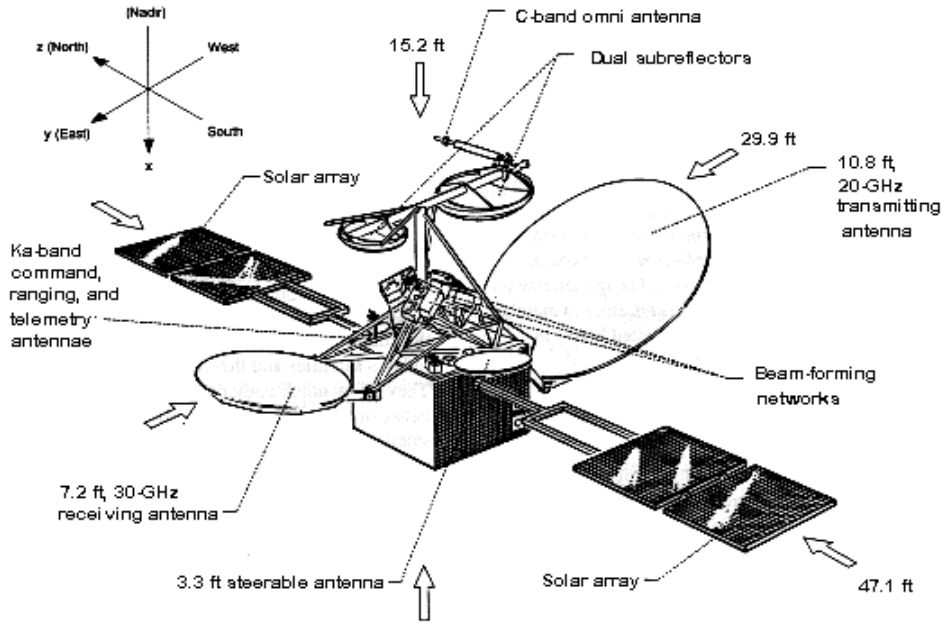

Figure 1.1 ACTS Components (1)

CHAPTER II

2. THEORETICAL BACKGROUND

The following chapter summarizes the theory of atmospheric scintillation at Ka-band frequencies. The physical processes which cause tropospheric scintillation are described, and several types of scintillation are defined. The mathematical expressions for the scintillation variance and spectrum are presented, and the effects of antenna aperture size on scintillation intensity are explained. The effects of atmospheric propagation on wideband signals are also discussed.

2.1 Physical Causes of Atmospheric Scintillation

Scintillation is one of the many effects the Earth's atmosphere may have on a propagating microwave signal. Both the amplitude and the phase of a signal can be affected by these rapid temporal fluctuations. Scintillation occurs as the wave travels through regions of the atmosphere exhibiting slight spatial and temporal variations in the dielectric parameters affecting propagation. These variations cause an alternating focusing and scattering of the transmitted wave which is perceived by the receiver as scintillation.

In general, it is possible for electromagnetic waves to experience scintillation in any region of the atmosphere. For frequencies below 3GHz, ionospheric scintillation is significant. However, at Ka-band frequencies, scintillation primarily originates in the troposphere. Variations in temperature, barometric pressure, and water vapor content cause the variations in refractive index which result in scintillation (2). The refractivity, N, and the index of refraction, n, in the Earth's troposphere at microwave frequencies are given by (2)(3)

$$N = (n-1)\times 10^6 = \frac{77.6}{T}\left(P + \frac{4180e}{T}\right), \qquad (2.1)$$

where T is the temperature in Kelvin, P is the total pressure in millibars, and e is the partial pressure of water vapor in millibars. At the tropopause (about 15km in temperate latitudes), N is about 40, down from over 300 at the surface. The relative differences resulting from humidity variations are much stronger near the surface. This explains why scintillation

generally originates in the lower levels of the troposphere. Even when turbulence does occur in the upper levels of the atmosphere, the relative differences in refractive index between adjacent air masses are insignificant compared with that seen near the surface in the atmospheric boundary layer.

The atmosphere is generally stratified into parallel layers by temperature and humidity differences. Turbulence within a layer will generate very little scintillation because the air is fairly well mixed within the layer and refractive differences are small. However, at the boundaries between layers, turbulence can mix air masses with very different characteristics. This phenomenon allows scintillation to be modeled to a first approximation as occurring in a thin layer or layers, with the rest of the propagation path assumed to be scintillation free (4).

Tropospheric scintillation can occur under several distinct circumstances. Turbulence in the lower troposphere can cause random mixing between air masses, resulting in dry scintillation (also referred to as clear air scintillation). Note that "dry" in this context does not mean that water vapor is not present; there is always a finite amount of water vapor in the troposphere. Rather, "dry" merely means that the air is not saturated by water vapor. When water vapor saturation does occur, clouds are formed. As the clouds pass through the propagation path, scintillation can occur at the boundary between the cloud and the clear atmosphere. Since this involves air which is saturated by water vapor, this is called wet (or moist) air scintillation (5). Given the right conditions, cloud droplets condense to

produce rain within the propagation path. Variations in rainfall within the propagation path cause signal variations which constitute another source of scintillation (6).

Regardless of the cause, scintillation-induced signal variations generally have a period of a few seconds. This distinguishes scintillation from slow-fading rain attenuation events which have periods of several minutes (7). Also, in contrast to rain fading, it should be noted that scintillation is not a loss process. The scintillation variations cause both enhancement and attenuation of the propagating signal, but the average signal level remains unchanged. Scintillation may occur simultaneously with rain attenuation, but the two effects are caused by different mechanisms (8). Clear-air scintillation is the result of turbulent mixing in the troposphere, while rain attenuation is caused by the absorption and scattering of electromagnetic energy by liquid raindrops.

The most common model for atmospheric turbulence is based on the Komolgorov description of homogeneous and isotropic turbulence (9). Large turbulent eddies, created by wind shear or convective heating from the earth's surface, break down into smaller eddies. The vortices will continue to break down until the scale of the turbulent eddies are small enough that viscous damping dissipates the kinetic energy of air motion as heat. This process defines an outer (L_o) and inner (l_o) scale of turbulence. In the range between L_o and l_o, the turbulence can be considered isotropic: the spectral distributions of eddy sizes and turbulent velocities are not dependent on position within the turbulent zone. This is also referred to as the inertial subrange, as there is no energy added or dissipated by turbulent eddies in this size range. Eddies smaller than l_o are quickly dissipated by the viscosity of the

atmosphere. The magnitude of outer scale L_o depends on the intensity of the turbulence. In the troposphere boundary layer, L_o can vary from a few meters (10) up to hundreds of meters (3)(11), while l_o is on the order of a millimeter (12).

The magnitude of the variations in the local refractive index are related to the differences in local temperature and humidity, and to the intensity of the turbulence. In the Komolgorov theory this is quantified by C_n, the structure constant for the index of refraction. The value of the structure constant indicates the magnitude of the local variation in the index of refraction. In the troposphere, the value of C_n is generally between $10^{-6}m^{-1/3}$ and $10^{-9}m^{-1/3}$. The structure constant is defined by the structure function, $D_n(r)$, for the refractive index fluctuation (3),

$$D_n(\mathbf{r}) = \left\langle \left| n_1(\mathbf{r}+\mathbf{r}_1) - n_1(\mathbf{r}_1) \right|^2 \right\rangle = C_n{}^2 r^{2/3}, \tag{2.2}$$

where n_1 is the first-order fluctuation in the refractive index n, defined by

$$n = \langle n \rangle \left(1 + n_1\right), \tag{2.3}$$

where $\langle n \rangle$ is the average refractive index. The vector $\mathbf{r_1}$ identifies a random point with in the turbulence, while $\mathbf{r}$ is the vector from $\mathbf{r_1}$ to another nearby point separated by a distance r. The structure function is valid throughout the inertial subrange, when r is between L_o and l_o. The structure constant is related to the variance in refractive index fluctuation and the outer scale of turbulence by (3)

$$C_n^{\,2} = 1.91\left\langle n_1^{\,2}\right\rangle L_o^{\,-2/3}. \tag{2.4}$$

Turbulence is not always homogenous, but the Komolgorov theory has been shown to describe atmospheric turbulence very accurately in many situations. For turbulence occurring within a layer of the troposphere, the turbulent motions tend to be homogeneous and isotropic. To a good approximation, turbulent parameters such as the structure parameter and the inner and outer scale lengths remain constant (3). Turbulence is not stationary in the long-term sense, but scintillation events tend to be stationary over 10 to 15 minute intervals (13). As this is much greater than the period of the scintillations, the effects of turbulence can be modeled as a quasistationary process.

2.2 Scintillation Variance

The theory explaining the effects of homogeneous turbulence on a propagating electromagnetic wave was developed by Tatarski (14). The propagating E-field is expressed in the form

$$E(\mathbf{r}) = \exp(\chi(\mathbf{r}) + jS(\mathbf{r})), \tag{2.5}$$

where χ is the log-amplitude function and S is the phase function. Using the Komolgorov description of turbulence, Tatarski developed expressions for the auto-correlation and variance of the log-amplitude and phase. The variance of the log-amplitude χ is

$$\sigma_\chi^2 = 0.167\left(\frac{2\pi}{\lambda}\right)^{7/6} \int_0^L C_n{}^2(z) z^{5/6} dz\,. \tag{2.6}$$

If the structure constant C_n does not vary along the turbulent path length L, this simplifies to

$$\sigma_\chi^2 = 23.2 C_n{}^2 \left(\frac{2\pi}{\lambda}\right)^{7/6} L^{11/6} \text{ (dB)}^2. \tag{2.7}$$

If the turbulence is confined to a thin layer between z_1 and z_2, the structure constant is zero elsewhere and the variance reduces to (15)

$$\sigma_\chi^2 = 41.3\left(\frac{2\pi}{\lambda}\right)^{7/6} C_n{}^2 (z_2 - z_1)\left(\frac{z_2 + z_1}{2}\right)^{5/6} \text{ (dB)}^2. \tag{2.8}$$

The Tatarski derivation assumes that the scintillation is relatively weak; this is satisfied when σ_χ is less than 5dB (16). This condition is applicable to microwave propagation in almost every case. The derived $7/6^{th}$-power frequency dependence of σ_χ^2 is valid assuming

$$l_o < \sqrt{\lambda L_g} < L_o\,. \tag{2.9}$$

In this case, L_g is the path length from the transmitter or receiver to the turbulent region. This condition is equivalent to stating that the diameter of the first Fresnel zone is between the inner and outer scale of turbulence. Physically, the first Fresnel zone is a circle that

encompasses all paths less than $\lambda/2$ longer than the direct path. This is illustrated in Figure 2.1. The phase of signals traveling along these paths will be within 180 degrees of the direct signal and may add constructively at the receiver.

For Ka-band, the wavelength is generally somewhat larger than the inner scale of turbulence, so the lower bound of the condition is easily met. However, for an Earth-space link, the distance from the ground station to the turbulent layer is on the order of a few kilometers. Thus, for Ka-band wavelengths, the Fresnel zone in the turbulent zone may be as large as 10m. This means the outer scale of turbulence can be roughly the same size as the Fresnel zone.

If the outer scale of turbulence is much less than the Fresnel zone size, the amplitude variance varies as k^2, where k is the wavenumber. Measurements show that when the outer scale and the Fresnel zone are of similar size, the frequency dependence is intermediate, between $k^{7/6}$ and k^2 (10). Thus the frequency dependence of scintillation may be used to measure the outer scale of turbulence. This assumes that due to antenna near-field beamwidth constraints, the first Fresnel zone is the primary carrier of the received energy.

Unlike the amplitude spectrum, the phase spectrum depends strongly on the outer scale of turbulence, because of the fact that larger turbulent eddies affect the signal phase much more than small eddies. The general expression for the phase variance is (15)

$$\sigma_S^2 = 0.782 C_n^2 \left(\frac{2\pi}{\lambda}\right)^2 L_o^{5/3} L - 0.307 C_n^2 \left(\frac{2\pi}{\lambda}\right)^{7/6} L^{11/6} \text{(rad)}^2. \qquad (2.10)$$

Phase scintillation tends to be small at C-band and Ku-band frequencies, and most of the literature tends to concentrate on the effects of amplitude scintillation. But since phase scintillation does vary as f^2, it is expected to be much more noticeable at the higher Ka-band frequencies.

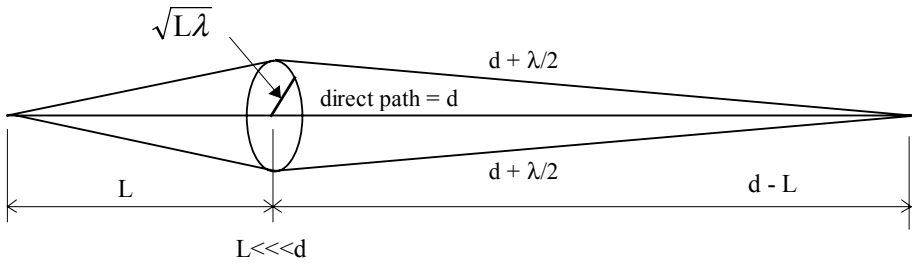

Figure 2.1 First Fresnel Zone

2.3 Scintillation Spectrum

The frequency spectrum of the scintillation amplitude variance is found by computing the power spectral density of χ, the log-amplitude function. The shape of the spectrum appears similar to low-pass filtered white noise. It is essentially flat up to a frequency f_o, where it rolls off with a $f^{-8/3}$ dependence. The roll-off frequency f_o is called the Fresnel

frequency. It is related to the mean flow velocity v of the turbulence orthogonal to the propagation path by (17)

$$f_o = \frac{v}{\sqrt{2\pi\lambda L_g}}. \tag{2.11}$$

The Fresnel frequency may be thought of as a measure of how quickly eddies the size of the first Fresnel zone move through the propagation path. The spectrum is generally expressed in terms of the asymptotic forms (3)(18)

$$W_\chi^0(f) = 64.17\frac{C_n{}^2 L^{7/3}}{v}\left(\frac{2\pi}{\lambda}\right)^{2/3} \quad dB^2/Hz, \quad (\text{as } f \to 0), \tag{2.12}$$

$$W_\chi^\infty(f) = 1.23 C_n{}^2 L\left(\frac{2\pi}{\lambda}\right)^2 v^{5/3} f^{-8/3} \quad dB^2/Hz, \quad (\text{as } f \to \infty). \tag{2.13}$$

The corner frequency f_c where the low and high frequency asymptotes meet is equal to $1.43f_o$. For typical conditions involved with microwave propagation, f_c is on the order of 0.1Hz to 1Hz.

The phase spectrum exhibits the same $f^{8/3}$ roll off at high frequencies, but it keeps the same frequency dependence for low frequencies as well. The form is the same as the amplitude scintillation high-frequency asymptote expressed in $(Np)^2/Hz$, with an elevated

magnitude below the Fresnel frequency. The asymptotic form of the spectrum for the phase scintillation variance is given by (3)(18)

$$W_S^0(f) = 0.0326 C_n^2 L \left(\frac{2\pi}{\lambda}\right)^2 v^{5/3} f^{-8/3} \quad \text{rad}^2/\text{Hz}, \quad (\text{as } f \to 0), \tag{2.14}$$

$$W_S^\infty(f) = 0.0163 C_n^2 L \left(\frac{2\pi}{\lambda}\right)^2 v^{5/3} f^{-8/3} \quad \text{rad}^2/\text{Hz}, \quad (\text{as } f \to \infty). \tag{2.15}$$

The general forms of the log-amplitude and phase scintillation spectra are shown in Figure 2.2, showing what is expected when scintillation is present. In the absence of scintillation, the amplitude noise spectrum appears flat throughout, and the phase noise spectrum maintains a constant frequency dependence. Without scintillation, there is no elevation in the amplitude or phase noise at the lower frequencies.

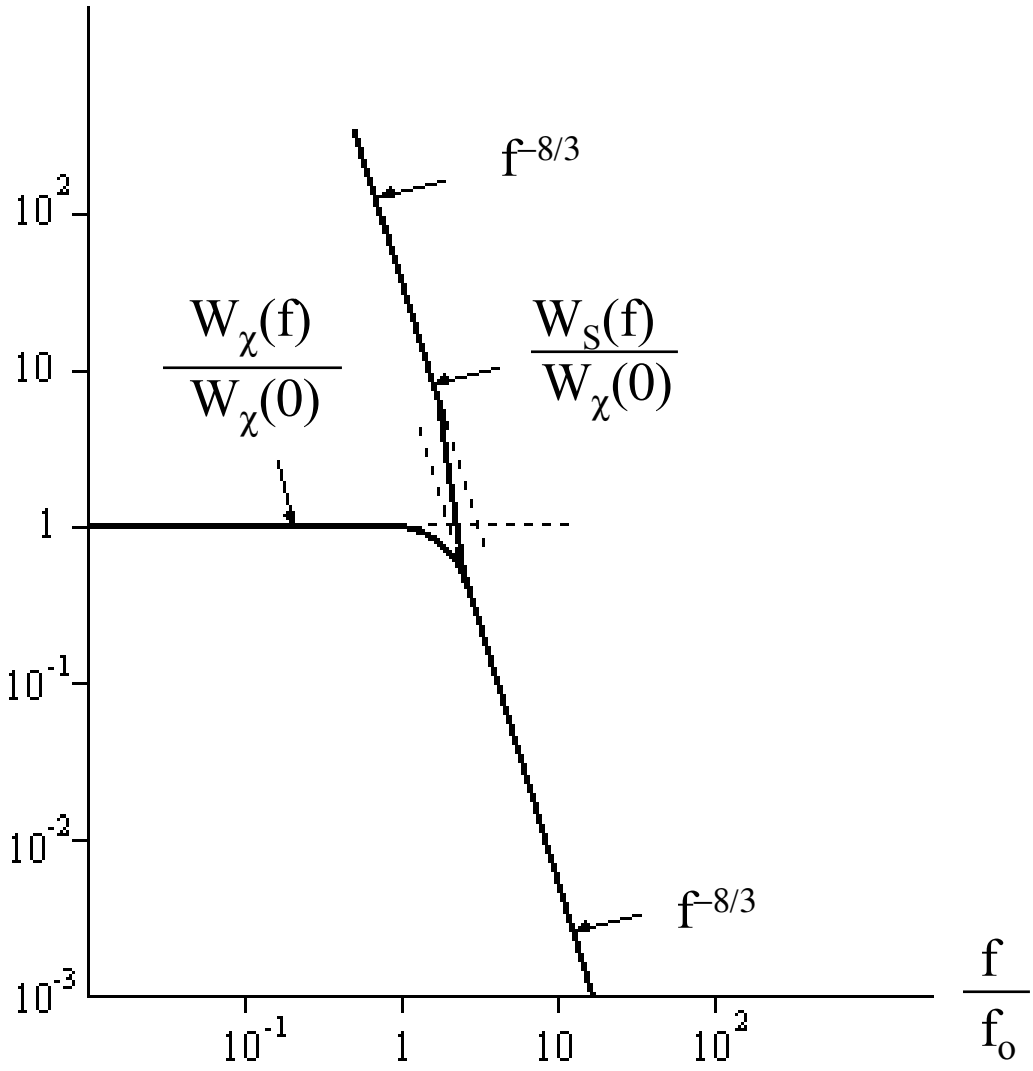

Figure 2.2 Theoretical Scintillation Amplitude and Phase Spectra

2.4 Effects of Antenna Aperture Size

The derivation shown in the previous section is based on a point receiver. It has been shown by Haddon and Vilar (17) that a finite aperture antenna has a smoothing effect on the scintillation statistics. This effect is significant when the antenna diameter is larger than the first Fresnel zone, $\sqrt{\lambda L_g}$. For an aperture antenna, the transition between near-field and far-field behavior occurs at a distance on the order of D^2/λ from the antenna (19). If $L_g >> D^2/\lambda$, then the turbulence is in the far field, and the antenna acts as a point receiver. However, when $L_g << D^2/\lambda$, the turbulence is in the near field of the antenna. If the size of the first Fresnel zone is less than the aperture size, the fluctuations in the received wavefront resulting from the turbulence are uncorrelated across the aperture and tend to interfere and reduce the total scintillation observed. In this case, the amplitude variance is scaled by an antenna aperture averaging factor, G(x), which is between zero and one. This averaging factor has been derived by Haddon and Vilar (17) as

$$G(x) = 3.8637(x^2+1)^{11/12}\sin\left(\frac{11}{6}\arctan\left(\frac{1}{x}\right)\right) - 7.0835x^{5/6}, \tag{2.16}$$

where x is defined as

$$x = 0.0584\frac{D^2\eta k}{L_g}. \tag{2.17}$$

The antenna diameter is denoted by D, and the aperture efficiency is η. In Figure 2.3, G(x) is plotted versus the ratio of the effective aperture diameter to the diameter of the first Fresnel zone, $D\sqrt{\eta/\lambda L_g}$. For the ACTS VSAT antenna at Georgia Tech, this ratio is approximately 0.25 or less, depending on the value assumed for L_g. This corresponds to an aperture weighting factor of about 0.85. In other words, since a VSAT antenna is relatively small, the turbulent region tends to be in the far field of the antenna, and very little aperture smoothing occurs.

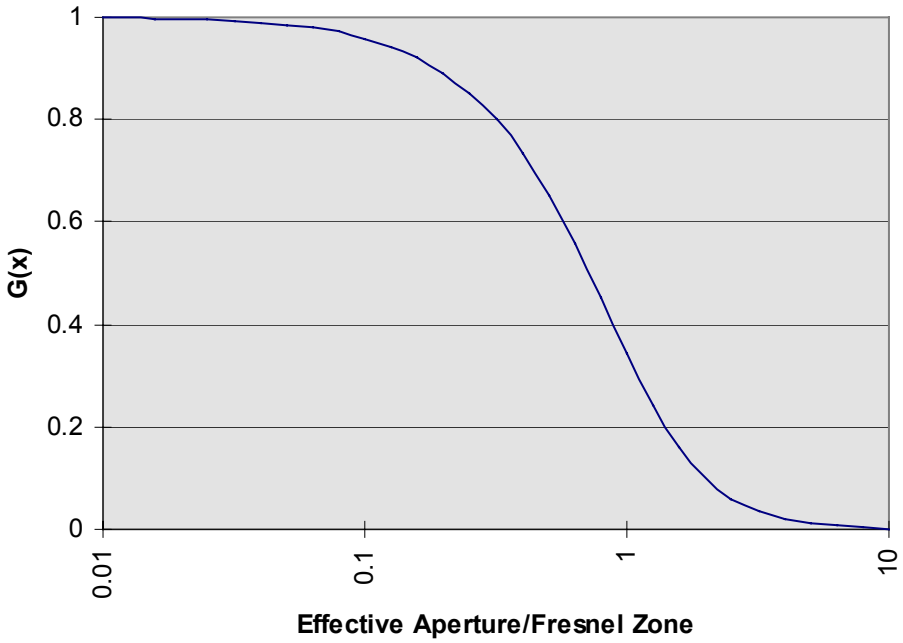

Figure 2.3 Aperture Weighting Function

2.5 Propagation Effects on Digital Signals

In the atmospheric propagation of digital signals (such as CDMA spread spectrum), new issues become important that are not generally considered for narrowband carrier signals. Variations in the dielectric parameters as a function of frequency can result in signal dispersion. This leads to distortion of the transmitted signal and a degradation in the overall system performance. Also, the effects of scintillation on the link bit-error rate (BER) need to be taken into account for a CDMA (or any digitally modulated) signal.

Several studies have looked at the bulk dispersive properties of the atmosphere for Ka-band communications systems. Measurements of phase and amplitude dispersion have been conducted at 28GHz and 19GHz, and the only frequency dependencies found were those resulting from the bulk properties of water in rain (20). Simulations performed on QPSK (quadrature phase shift keying) signals in the 10-30GHz range modeled the dispersive effects of the atmosphere on the link BER. For a quiet atmosphere (no scintillation), the dispersion in phase and amplitude was nearly linear with frequency (21) and had no significant effect on the system performance.

The effects of scintillation and turbulence in a VSAT system are not as predictable, as the effects of scintillation do not vary linearly with frequency. Fast variations in the received signal amplitude can cause deviations in the system BER performance from the expected values. Since scintillation involves both signal enhancement and attenuation, the BER of the system can fluctuate both above and below the theoretical BER versus carrier-to-noise (or E_b/N_o) curve. Models of cloud-induced scintillation demonstrate that the

transfer function of the atmosphere can vary greatly with frequency. This is due to the interaction between the different frequency dependencies of the Fresnel zone radius and the antenna radiation pattern (22). Applying this cloud scintillation model to a broadband QPSK transmission confirmed that scintillation can have a profound effect on the link BER. For high E_b/N_o levels, cloud scintillation can cause variations in the BER of several orders of magnitude. The level of degradation is strongly dependent on the transmission frequency and the bandwidth of the signal (23). Based on the simulation, higher frequency and wider bandwidth signals are both more prone to inter-symbol interference in the presence of scintillation. Therefore, Ka-band spread-spectrum transmissions are expected to be impaired by strong scintillation effects.

The combined effects of rain and scintillation on the outage time for a Ka-band satellite link have been modeled by Alouini et. al. (24). For a low-margin VSAT system, the presence of scintillation results in increased outage time on the link. However, for a higher margin system, it was found that scintillation actually reduces the outage time. This is due to the symmetric nature of scintillation, which results in both signal enhancements and fades, as well as the asymmetric performance of a digital modem.

CHAPTER III

3. EXPERIMENTAL HARDWARE

The hardware used to perform this research can be configured as three different systems depending on the measurement to be made, although many components are common to more than one configuration. The simplest arrangement is the receive-only system for monitoring the beacon signals from the ACTS satellite. By adding a microwave transmitter, the second system is also capable of sending a carrier wave through ACTS. The third system uses a CDMA modem to send and receive spread spectrum-signals at Ka-band. Each of the three systems is described in detail in the following sections. Also, the weather monitoring system is explained.

3.1 Beacon Receiver System

The ACTS satellite continuously transmits beacon signals on two different frequencies, 20.185GHz and 27.505GHz, as detailed in Table 3.1 (25). A third beacon signal at 20.195GHz is available on the satellite, but is seldom transmitted. As part of the ACTS Propagation Campaign, several research groups throughout the country monitor these beacons in order to characterize the Ka-band propagation channel. All of these groups use a standardized receive-only terminal that records fluctuations in the amplitude of the received beacon signals at one second intervals. However, information on phase fluctuations cannot be measured by these terminals.

To completely characterize the effects of the atmosphere on propagation at Ka-band, measurements of both amplitude and phase fluctuations are necessary. By tracking the variations in the received phase of the beacon signal during different atmospheric conditions, the limitations of the Ka-band channel may be determined. These measurements also determine the performance limitations of the ACTS beacon transmitter and the receiving system.

Data have been collected by downconverting the received beacon signal at 20.185GHz to the audio frequency range (near 2kHz), then filtering to isolate the beacon carrier wave from the modulated sidebands. The signal is digitally sampled using a personal computer (PC), then digital signal processing is used to measure the phase variations and compute the scintillation spectra. The short-term standard deviation of the amplitude and phase fluctuations have been computed and monitored under different atmospheric

conditions, along with the spectral distribution of the amplitude and phase variations. The amplitude and phase spectra measured during turbulent weather conditions have been examined for enhanced scintillation effects.

The beacon receiver hardware system is illustrated in Figure 3.1. This system receives the ACTS telemetry beacon signal at 20.185GHz, then downconverts and amplifies it through several stages to a 2.0kHz signal. This audio signal is digitally sampled at 20kHz, then Matlab signal processing is used to analyze the spectral characteristics.

The system uses a 1.2m diameter VSAT dish antenna that is on loan from NASA LeRC and currently resides on the roof of the Van Leer Building at Georgia Tech. ACTS is positioned in geostationary orbit at a longitude of 100°W. From Atlanta, at longitude 84.4°W and latitude 33.8°N, the satellite is located at an elevation of 47.3° and an azimuth of 206.7°. The dish uses an offset feed, with most of the microwave components residing in the outdoor feed enclosure unit (FEU). Connected to the feed horn is an ortho-mode transducer (OMT), which isolates the orthogonal receive and transmit waves. The incoming beacon signal is routed to the low-noise amplifier (LNA). The LNA has a gain of 30dB and a noise figure of 3dB (or equivalently a noise temperature of 290K). The overall receiving system noise temperature (T_{sys}) has been measured at roughly 400K in clear air conditions.

The received C/N ratio can be computed given the effective isotropic radiated power (EIRP) of the ACTS beacon, the path loss L_p, the receive antenna gain G_r, and the system noise temperature T_{sys}. The equation is (26)

$$\frac{C}{N} = \frac{(EIRP)G_r}{L_p(kT_{sys}B)}, \tag{3.1}$$

where k is the Boltzmann constant and B is the noise bandwidth. The product $kT_{sys}B$ represents the total noise power. The path loss is given by (26)

$$L_p = \left(\frac{4\pi R}{\lambda}\right)^2, \tag{3.2}$$

where R is the path length from the satellite to the ground station, and λ is the transmission wavelength. For this project, the distance from ACTS to the Atlanta terminal is 37,340km, and the beacon wavelength is 0.0149m. The result is a path loss of 210dB. The receive antenna gain is computed using (26)

$$G_r = \eta\left(\frac{\pi D}{\lambda}\right)^2, \tag{3.3}$$

where D is the antenna diameter (1.2m in this case) and η is the antenna aperture efficiency. Assuming an aperture efficiency of 50%, the receiving antenna gain is 45dB.

In the Atlanta area, the EIRP of the ACTS beacon is 17.0dBw. If a noise bandwidth of 1kHz is used (which is the resolution used with the spectrum analyzer for the measurement), the noise power is -172.58dBw. Since there is no image rejection filter in the second stage of the downconversion, the noise power is effectively doubled by the combination of noise band images. So the noise power level used is -169.58dBw. Combining all of the terms, the computed C/N for the beacon is

$$\left(\frac{C}{N}\right)_{downlink} = 17.0\text{dBw} + 45\text{dB} - 210\text{dB} - (-169.6\text{dBw}) = 21.6\text{dB}. \qquad (3.4)$$

There are other losses not included in this calculation such as the atmospheric attenuation loss and antenna pointing loss. Under clear weather conditions, these are fairly small (<1.0dB each) and have a minimal effect on the result.

A phase-locked oscillator at 17.62554GHz within the FEU is used to downconvert the beacon to an IF of 2.55946GHz. This IF signal is amplified and sent to the satellite communications laboratory, where it is downconverted to a second IF of 342.0MHz. Then, the signal is amplified further to provide a sufficient signal level for the A-D conversion and is passed through a filter with a 1MHz bandwidth to remove unwanted downconversion products. A final downconversion results in a signal in the audio frequency range near 2kHz. As shown in Figure 3.2, the ACTS beacon includes modulated telemetry data offset 32kHz and 64kHz from the main carrier signal. A simple 10kHz low-pass filter is used to remove the modulated subcarriers, leaving only the beacon carrier wave.

Using a personal computer, the 2kHz beacon carrier is digitally sampled at a 20kHz rate with twelve-bit resolution. The data acquisition card and computer are used to store six million sample points, which corresponds to five minutes of data at this sampling rate. The digital data is then processed using Matlab by breaking the five-minute sample sequences into shorter segments of 15 seconds each, then averaging the spectral characteristics of the segments. Magnitude and phase fluctuations from a best-fit carrier frequency are computed, then the spectral distributions of those fluctuations is found. Digital fast Fourier transforms (FFTs) are performed on the data using 280,000 points. The resulting spectra have a frequency resolution of 0.071Hz. This resolution is sufficient to detect the Fresnel frequency of the scintillation. The measured Fresnel frequency of the scintillation spectrum tends to be in the range of 0.1Hz to 1.0Hz.

Table 3.1 ACTS Beacon Characteristics (25)

Frequency	27.505GHz ± 0.3MHz	20.195GHz ± 0.5MHz	20.185GHz ± 0.3MHz
Polarization	vertical	horizontal	vertical
Modulation	none	FM and PCM	FM and PCM
RF Power	20 dBm	23 dBm	23 dBm
EIRP (in GA)	18.0 dBw	17.0 dBw	17.0 dBw

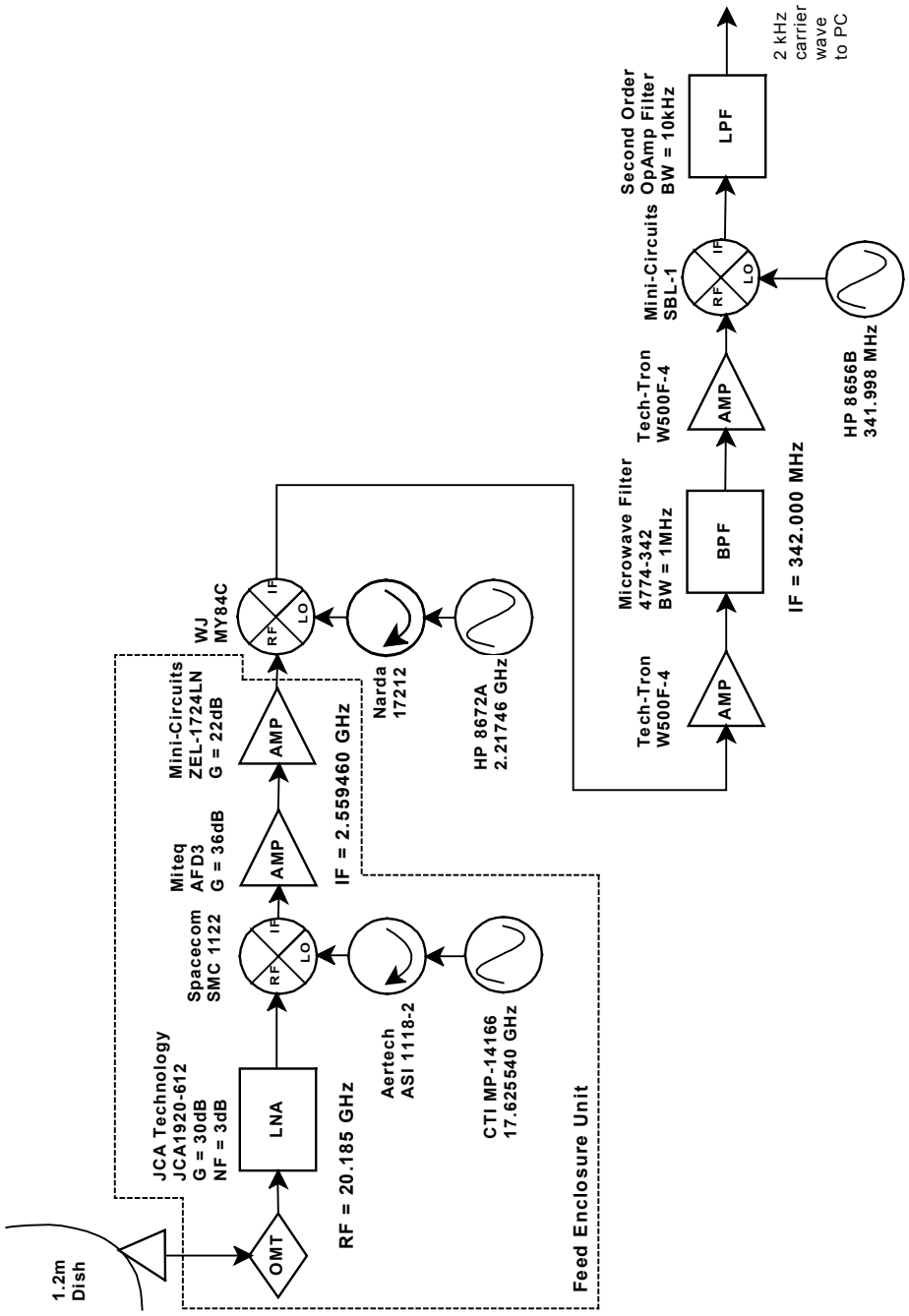

Figure 3.1 Beacon Receiver Hardware System

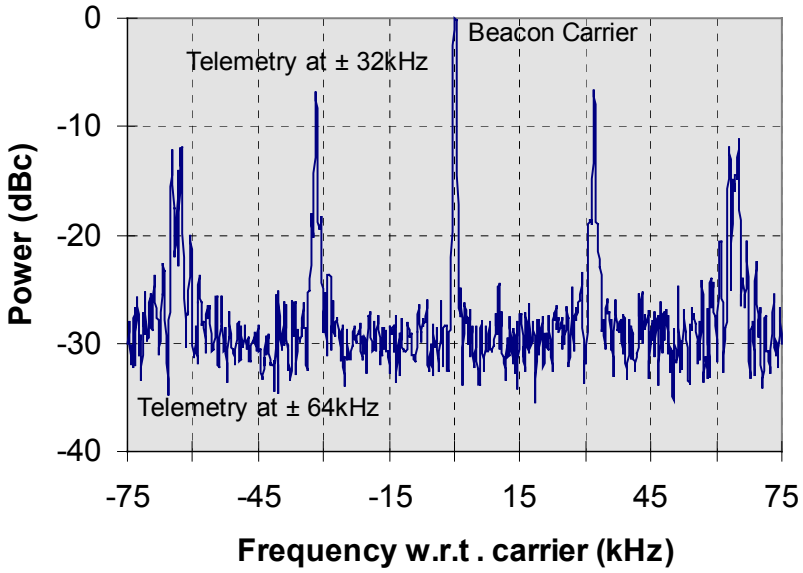

Figure 3.2 Spectrum of ACTS Telemetry Beacon

3.2 Carrier Transceiver System

The approximate EIRP of the ACTS beacon is 17.0dBw. In clear air conditions, the received carrier-to-noise ratio (C/N) for the beacon is computed to be 21.6dB at the Georgia Tech ACTS terminal. In order to measure the scintillation produced during rain events when attenuation is considerable, additional link margin is needed. This can be accomplished by monitoring a carrier signal transmitted from the Georgia Tech terminal and then relayed back though the ACTS microwave switch matrix (MSM) in loopback mode. Ideally, the clear-sky carrier level in this mode is over 18dB higher than the received beacon carrier level.

The carrier transceiver system is shown in Figure 3.3. This system includes a transmitter capable of broadcasting a Ka-band signal to the ACTS satellite in geostationary orbit. A carrier wave tone generated by a laboratory signal synthesizer is upconverted in two stages to 29.64588GHz. After amplification to a power level of 1watt, the signal is transmitted to ACTS. A transponder on the satellite downconverts the signal by 9.72GHz (to 19.92588GHz) before retransmitting the signal back to Atlanta. The receiver described in the previous section is used to downconvert the signal to a 2kHz carrier wave for digital processing.

Both oscillators used to upconvert the carrier wave for transmission are located in the FEU. An oscillator operating at 11.75034GHz is used in the first stage to convert the incoming 270MHz signal to 12.02034GHz. This IF signal is filtered and amplified prior to the second stage. The same oscillator that is used for the receiver's first downconversion is

also used in the second and final upconversion. This LO signal and the IF signal are routed to the amplifier unit, which houses the Ka-band mixer and power amplifier. Originally, the uplink power amplifier was a traveling wave tube (TWT) amplifier on loan from NASA LeRC. Preliminary measurements were made using this system amplifier, but the TWT amplifier had several reliability problems. As a result, the TWT was replaced with a solid-state power amplifier. This solid-state amplifier has the same 30dBm rated power output as the TWT, so the predicted performance of the system remained essentially unchanged. Measurements of the system performance for this transmitter system are presented in a later chapter.

The uplink C/N ratio can be computed, given the uplink transmitter power P_t, the transmit antenna gain G_t, the path loss L_p, the satellite receive antenna gain G_r, and the satellite system noise temperature T_{sys}. The equation used is (26)

$$\frac{C}{N} = \frac{P_t G_t G_r}{L_p (kT_{sys} B)} . \tag{3.5}$$

Because of the shorter wavelength (0.0101m), the path loss on the uplink (213.3dB) is greater than the path loss computed for the downlink. But for the same reason, the gain of the 1.2m VSAT antenna (48.4dB) is also greater on the uplink than for the downlink. The rated power for the uplink amplifier is 1W (or 0dBw). The ACTS receive antenna gain for the Atlanta beam is 50dB. The system noise temperature for the ACTS receiver is 1130K, much higher than the ground station noise temperature. This is mainly due to the relative

noisiness of space-qualified Ka-band LNAs produced during the time ACTS was being built. The antenna temperature is also much higher because of the earth surface noise emission. The noise power that is input to the 1GHz bandwidth ACTS transponder is -108.1dBw. For a 1kHz noise bandwidth, the noise power level is -168.1dBw.

Combining all of the terms, the computed clear-air C/N at the satellite for the uplink is

$$\left(\frac{C}{N}\right)_{uplink} = 0\text{dBw} + 48.4\text{dB} + 50\text{dB} - 213.3\text{dB} - (-168.1\text{dBw}) = 53.2\text{dB}. \qquad (3.6)$$

The noise input to the transponder is sufficient to saturate the downlink amplifier. Since the carrier level at the satellite is below this noise floor by 6.8dB, the downlink EIRP will be below the rated downlink EIRP by the same margin. The rated downlink EIRP for ACTS is 61dBw, so the downlink EIRP for the carrier is 54.2dBw. The carrier loopback system uses the same front-end (antenna and LNA) as the beacon receiver system. So the downlink C/N for this system (again in a 1kHz bandwidth) is found by substituting this EIRP into the equation used for the beacon system, yielding

$$\left(\frac{C}{N}\right)_{downlink} = 54.2\text{dBw} + 45\text{dB} - 210\text{dB} - (-172.6\text{dBw}) = 61.8\text{dB}. \qquad (3.7)$$

The total C/N for the loopback is found using (26)

$$\frac{C}{N} = \frac{1}{\frac{1}{\left(C/N\right)_{uplink}} + \frac{1}{\left(C/N\right)_{downlink}}} = 52.6\text{dB}, \tag{3.8}$$

with the C/N values expressed as ratios, not decibels. The aggregate C/N for this system is 52.6dB for a 1kHz noise bandwidth. Therefore, the calculated C/N for the loopback carrier system is over 30dB greater than the C/N for the beacon receiver system.

The remainder of the receiver portion of the carrier transceiver system is similar to the beacon receiver system presented in the previous section. One difference is the addition of extra filtering after each stage to remove noise outside of the frequency range of interest. This filtering limits the system bandwidth to 70MHz, and eliminates the problem of image noise power being added in by the downconverters. The filtering is also used for the spread-spectrum transceiver system described in the next section. The carrier signal transmitted through the ACTS transponder has a much higher signal level than the beacon, so less amplification of the received signal is needed prior to digital sampling.

As with the beacon signal, the received carrier signal is downconverted to a 2kHz tone. It is then digitally sampled for analysis of the scintillation properties of the signal. The processing used is identical to that used for the beacon signals. However, the enhanced C/N of the transmitted carrier allows for the analysis of more severe attenuation events.

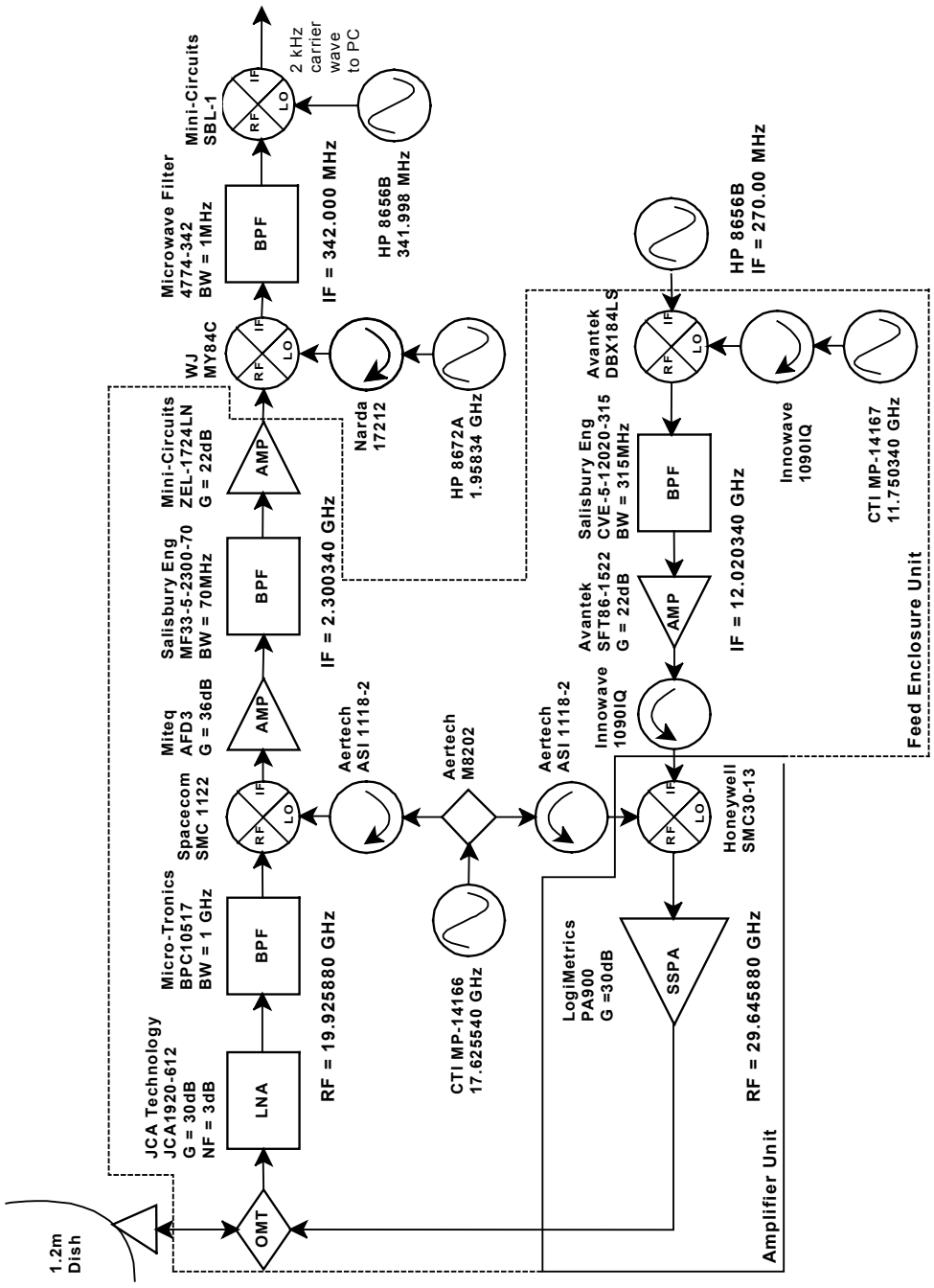

Figure 3.3 Carrier Transceiver Hardware System

3.3 Spread-Spectrum Transceiver System

A primary reason for measuring the scintillation generated by the Ka-band propagation channel is to ascertain the effect on phase-modulated digital transmissions. Code domain multiple-access (CDMA) systems are especially susceptible to phase noise interference because signal acquisition requires the convolution of the received signal with a digital code. The received signal is often below the noise floor level and spread over a large bandwidth, so excessive phase noise may corrupt the received waveform to the extent that signal acquisition is difficult or impossible. Amplitude scintillations can create instantaneous variations in the received C/N which result in a degradation in the signal BER.

A digital modem which produces a direct-sequence/spread-spectrum (DS/SS) signal has been used to test the ACTS system. The modem uses binary phase-shift keying (BPSK) modulation. The input data is spread by direct multiplication with the spreading code sequence. The highest chipping rate supported is 32Mcps, and data rates of up to 2Mbps are possible. A bit-error rate tester (BERT) is used to generate and monitor a digital data stream passed through the modem. A variable attenuator at the output of the modulator is used to control the transmitted carrier power level. This allows the monitoring of the BER as a function of C/N (or E_b/N_o, the ratio of energy per bit to noise power density) in a variety of different atmospheric conditions. The goal has been to determine if there is extra degradation in BER because of atmospheric effects which can be correlated to scintillation beyond the simple reduction in C/N caused by atmospheric attenuation.

For the spread-spectrum transceiver system, an L3 Communications (formerly Paramax) EB-100 CDMA modem is added to the carrier transceiver system. The modem includes a modulator and a demodulator, each with an RF section operating at 70MHz. An extra IF conversion stage is added to interface the CDMA modulator with the FEU. The modulator output is upconverted to 270.00MHz, and the demodulator input is downconverted from the 2.3GHz IF directly to 70MHz. This is illustrated in Figure 3.4.

For most of the testing performed during for this research, the data rate used was 1.544Mbps (T1). At this data rate, the chipping rate may be set to either 20 chips/bit or 5 chips/bit, for a total chip rate of 30.88Mcps or 7.72Mcps. Some testing was also performed with the spreading deactivated, for a normal BPSK signal. The modem has TTL-level clock output and data input and output connections. The bit-error rate tester (BERT) used has an RS-422 interface, so a converter is used to translate between TTL and RS-422 data signal levels. Since the modulation scheme is BPSK, the zero-ISI (inter-symbol interference) output bandwidth is double the data rate transmitted. For a T1 data stream encoded with 20 chips/bit, the bandwidth of the modem output is 61.8MHz, well within the IF filter bandwidth of 70MHz. A sample of the output spectrum of the modem is shown in Figure 3.5.

In order to relate the measurements made during different scintillation intensities, the changes in C/N and the effects of scintillation on a carrier need to be determined simultaneously. This was difficult to measure using the spread spectrum signal, as the received signal level is generally below the received noise floor. The method utilized was to

insert a pilot carrier signal into the transmitted CDMA waveform. The pilot carrier frequency is the first null frequency of the BPSK signal, which is determined by the chipping rate used by the modem. For a 30.88Mcps rate, the null is 30.88MHz below the center frequency of the signal. Using the carrier signal hardware described previously and a signal combiner, the pilot carrier can be generated at 39MHz and combined with the output of the modem centered at 70MHz. After the signal is received, the carrier signal is monitored separately from the CDMA signal using a signal splitter. This is also illustrated in Figure 3.4. Transmitting two signals on the same channel does introduce the possibility of 3rd-order intermodulation distortion. In order to avoid this, the combined power level of pilot carrier and spread spectrum signal must be set well below the saturation point of the uplink amplifier. This method does slightly reduce the maximum dynamic range of the system, but it also allows independent measurement of scintillation and BER to determine if the modem performance is impaired during scintillation events.

Measurements have been performed under a variety of atmospheric conditions to determine what conditions have the greatest effect on the system performance. By measuring the BER of the spread spectrum signal, along with the C/N ratio of the pilot carrier, any excess degradation of the modem performance can be monitored. When a degradation of the CDMA modem performance is observed, it is then possible to use the pilot carrier signal to determine if scintillation or excess phase noise is responsible. When spread spectrum BER measurements are performed, the pilot carrier is downconverted to the audio range and recorded. Then periods which show variations in the BER can be played back to check the C/N ratio of the pilot carrier. Using the methods described for

the previous carrier measurements, the amplitude and phase noise spectrum of the pilot carrier can be analyzed to check for the presence of scintillation on the channel. By correlating the BER performance measurements of the phase-modulated spread spectrum transmissions with the performance of the pilot carrier, the effects of the atmospheric scintillation on system performance can be resolved.

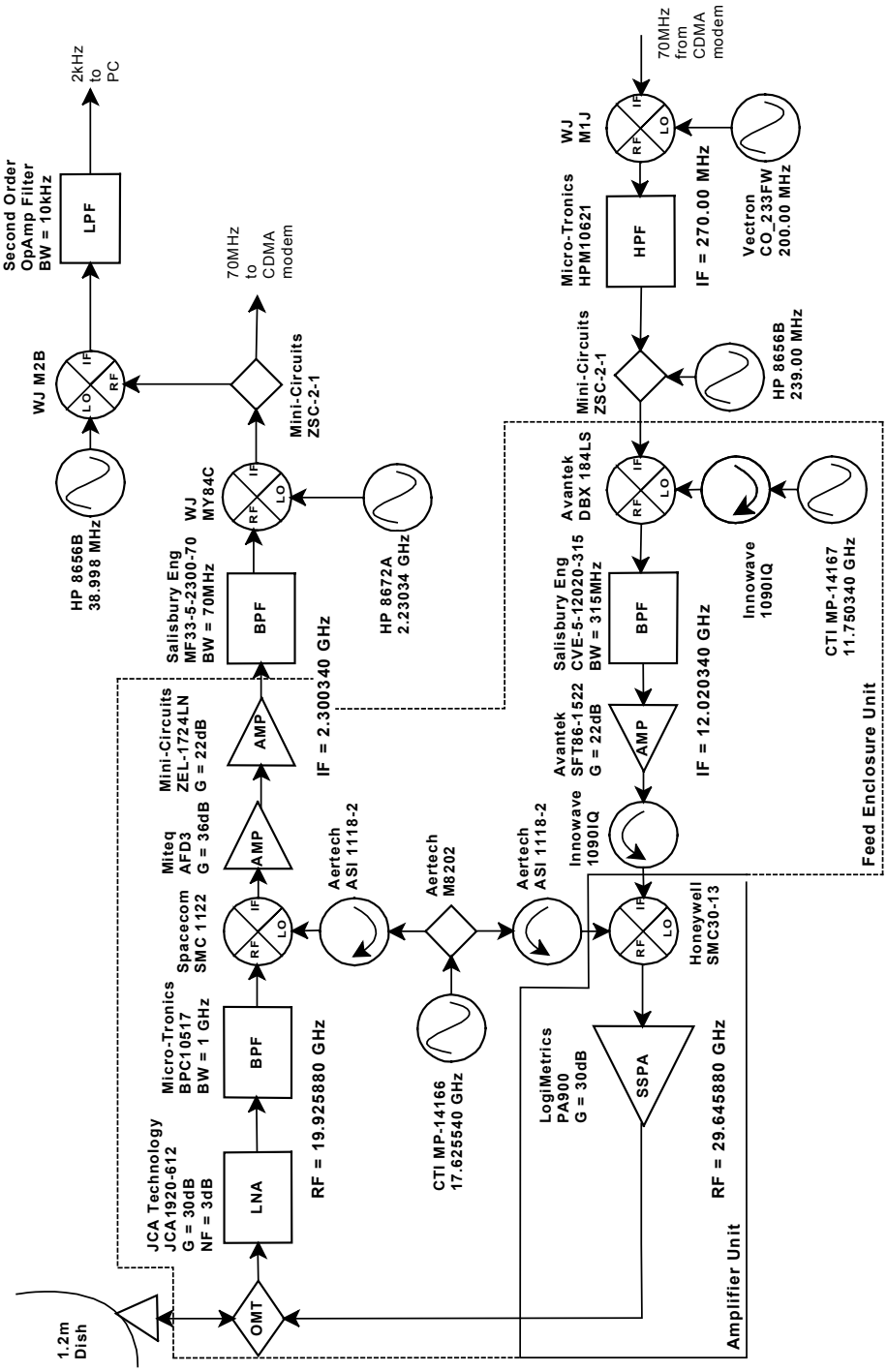

Figure 3.4 Spread Spectrum Transceiver Hardware System

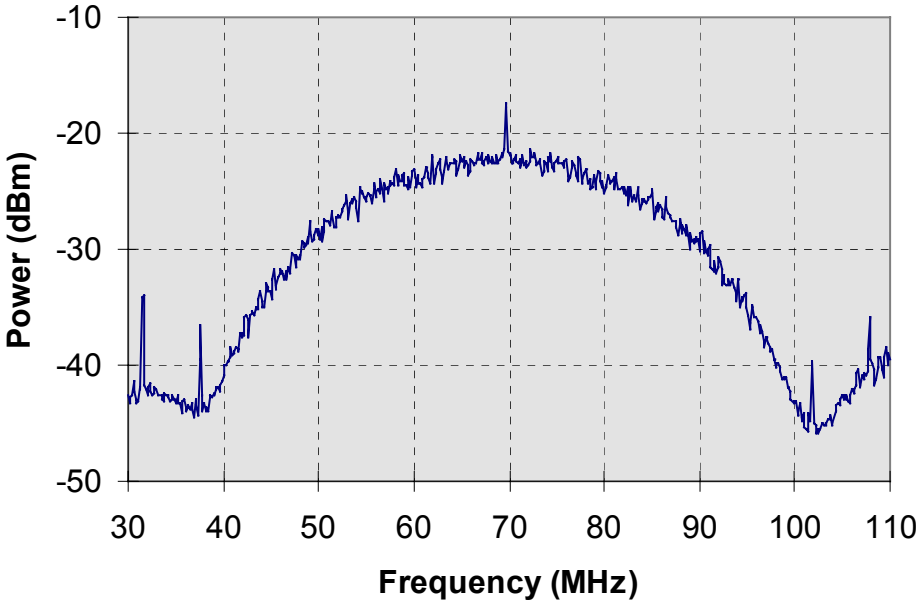

Figure 3.5 Sample CDMA Modem Output Spectrum

3.4 Weather Monitoring System

In order to track local weather conditions and correlate the measurements with atmospheric phenomena, a Davis Instruments weather monitor is used. This system has sensors for measuring temperature, humidity, accumulated rainfall, and wind speed and direction. The weather monitor takes readings every minute and stores the data on a PC. Estimates of rainfall rate may be obtained by dividing the accumulated rainfall by the appropriate time interval.

The rain gauge is of the 'tipping-bucket' type with a resolution of 0.01 inches. Coupled with the one-minute sampling time, this corresponds to a rainfall rate resolution of about 15mm/hr. This causes some difficulty in accurately measuring light rainfall, but most heavy rains have rates well above this resolution.

This monitoring station gives only the conditions locally at the site of the ground station. Although the scintillation is caused by turbulence higher in the troposphere than ground level, the data collected are useful in characterizing the overall weather environment at the time of a measurement. The weather station is also useful in identifying periods when turbulence is likely.

CHAPTER IV

4. EXPERIMENTAL MEASUREMENTS

This chapter describes the measurements that have been performed during the course of this research. The three system hardware configurations described in the previous chapter have been used to perform the experimental measurements. Receive-only measurements of the beacon carrier have been performed in clear conditions, in the presence of turbulence, and during rain events as well. Carrier tone transceiver measurements were performed using with the solid-state uplink system to characterize the performance of the transmitter, and to augment the measurements of atmospheric scintillation effects on the beacon. Also, the CDMA modem has been used with the transceiver system to characterize the effects of a turbulent atmosphere on phase-modulated wideband digital signals. Data collected during all of these experiments are presented in the following sections.

4.1 Beacon Signal Measurements and Processing

The most basic measurement performed for this research is the monitoring of the 20.185GHz beacon transmitted continuously by ACTS. From November 1996 through June 1997, daily observations of the beacon carrier in various weather conditions were conducted. The beacon was downconverted to approximately 2kHz, then digitally sampled at a 20kHz rate. The digital data were then processed using Matlab to extract the amplitude and phase variations in the signal in both the frequency and time domains. To accomplish this, a "best fit" sine wave was matched to the measured data, and then the variations in magnitude and phase from this ideal are computed and used to generated amplitude and phase spectra.

Many observers have measured the effects of amplitude scintillation in a Ka-band satellite system, and the results presented here confirm many of these observations, and agree well with the theory presented in Chapter 2. However, no measurements of phase scintillation due to tropospheric turbulence have been reported. The measurements we have made indicate that phase scintillation, along with amplitude scintillation, is present and detectable on Ka-band space-to-earth links.

Other research into the measurement of phase noise in Ka-band satellite systems indicates that a very low system phase noise floor is needed to be able to detect atmospheric phase scintillation (27). From the theoretical equations for scintillation phase spectra (Equations 2.14 and 2.15), the terms which are most uncertain for a given satellite system are C_n^2 and L, the structure constant and the turbulent path length, respectively.

Measurements by Vilar and Smith (17) constrain the product C_n^2L to be between 3.4×10^{-11} $m^{1/3}$ and 6.6×10^{-8} $m^{1/3}$. Using the Vilar et. al. (27) definition for the phase scintillation power spectral density

$$W_S(f) = 1.941\left(\frac{2\pi}{\lambda}\right)^2 v^{5/3}C_n^2Lf^{-8/3} \text{ rad}^2/\text{Hz}, \tag{4.1}$$

the phase scintillation spectra is constrained between $1.6f^{-8/3}$ rad^2/Hz and $0.00054f^{-8/3}$ rad^2/Hz The average phase noise level of our beacon receiving system is about $0.16f^{-8/3}$ rad^2/Hz; thus from a theoretical standpoint, our system should be sensitive enough to detect some instances of phase scintillation when they occur. The measurements which follow show that phase scintillation is often present and measurable.

The average clear-air C/N which was measured for the ACTS beacon carrier was about 24dB in a 1kHz noise bandwidth. This is within 2.5dB of the expected value computed in Equation 3.4, with the measured C/N slightly higher than the prediction. The most likely reasons for the small discrepancy are better than assumed system performance in terms of system noise temperature and aperture efficiency, plus variations in spacecraft performance.

All of the amplitude and phase spectrum measurements shown in this chapter represent the average spectra measured over a five minute interval. Spectral plots with a resolution of 0.071Hz are the spectral average of twenty 15-second intervals. For reference, all of the plots include a straight line representing an $f^{-8/3}$ slope. The computed values listed

in the tables for magnitude and angle deviations are based upon integrations of the spectra up to 10Hz. By comparing the mean deviation values for different measurements, and examining the spectra for elevation at the lower frequencies, instances of amplitude and phase scintillation may be identified. All measurement times listed are the local time in Atlanta.

4.1.1 Beacon Measurements from June 24

The weather on June 24 was hot and humid, a typical summer day in the southeastern United States. The skies were partly cloudy, with convective cumulus clouds forming throughout the afternoon. The scintillation observed on this day was intense in both amplitude and phase. Six measurements were conducted, and are summarized in Table 4.1. The phase scintillation deviation recorded during the five minutes beginning at 14:47EDT (233.58 rad) was the most intense measured on the ACTS beacon.

The six amplitude spectra plotted in Figure 4.1 and Figure 4.3 show two general forms. Three of the curves have spectra which flatten out below 0.4Hz, and approach the noise floor at very near the $f^{-8/3}$ rate. For the spectrum of the 14:47 data, the frequency dependence is actually $f^{-2.2}$. The other three curves tend to increase down to the lower limit of the measurement, with very little roll-off. It is likely that the first case is the "clear-air" situation, while the second case represents the effects of clouds passing through the propagation path. Of the six phase spectra shown in Figure 4.2 and Figure 4.4, four of the curves show a pronounced elevation in phase noise below 0.4Hz. The results from June 24

show scintillation which is very similar to theoretical model, with a Fresnel frequency near 0.4Hz.

Table 4.1 Beacon Measurement Data from June 24

Time (EDT)	Magnitude deviation	Angle deviation	Temperature	Dew point	High wind speed
13:32	0.111 dB	49.9 rad	90.5ºF	68.4ºF	8 mph
14:47	0.338 dB	233.6 rad	90.4ºF	68.1ºF	8 mph
15:15	0.111 dB	190.4 rad	91.4ºF	69.0ºF	9 mph
15:56	0.102 dB	97.0 rad	91.2ºF	68.2ºF	9 mph
17:07	0.153 dB	142.6 rad	91.0ºF	69.8ºF	8 mph
20:42	0.313 dB	20.1 rad	85.7ºF	69.7ºF	5 mph

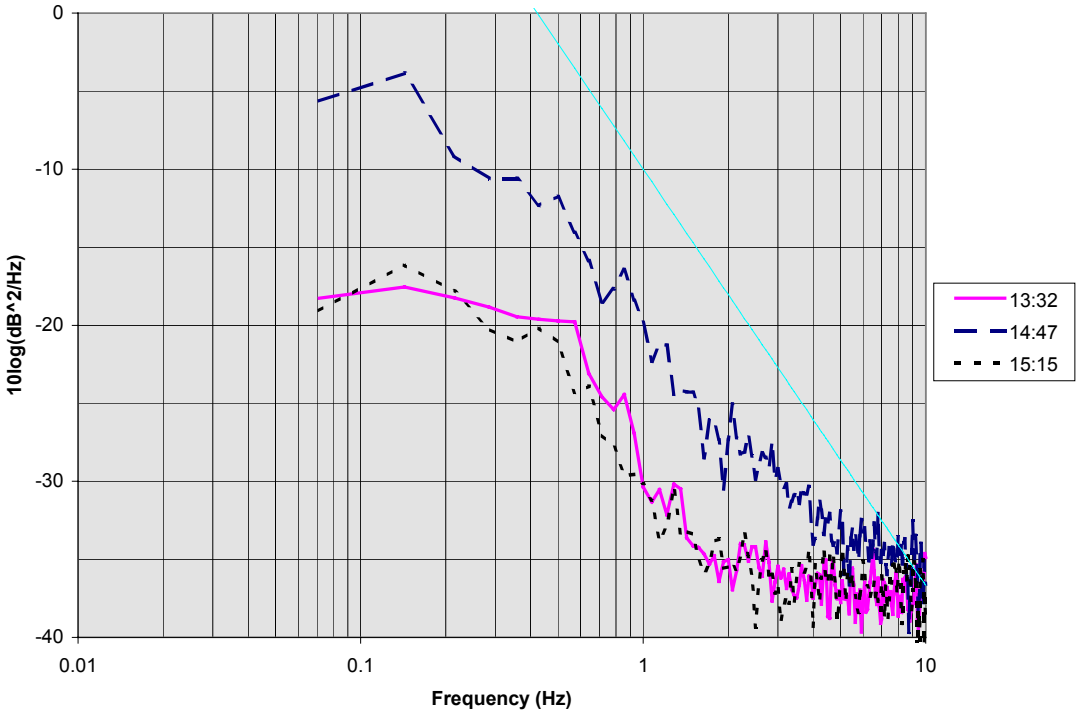

Figure 4.1 Beacon Amplitude Spectra from Midday June 24

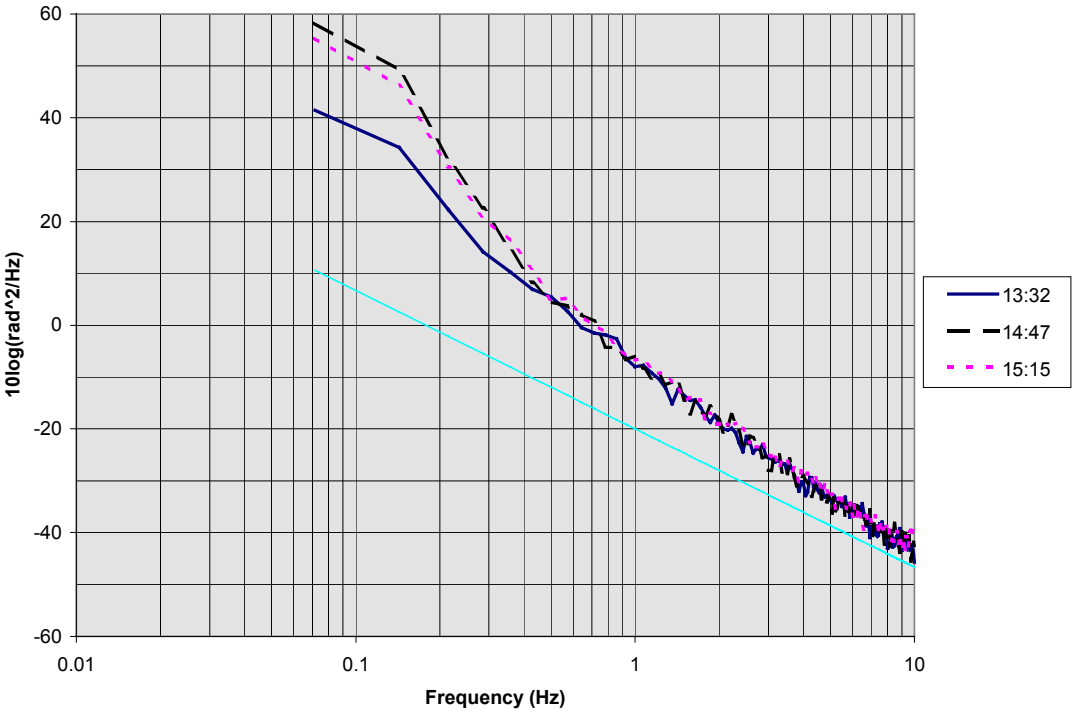

Figure 4.2 Beacon Phase Spectra from Midday June 24

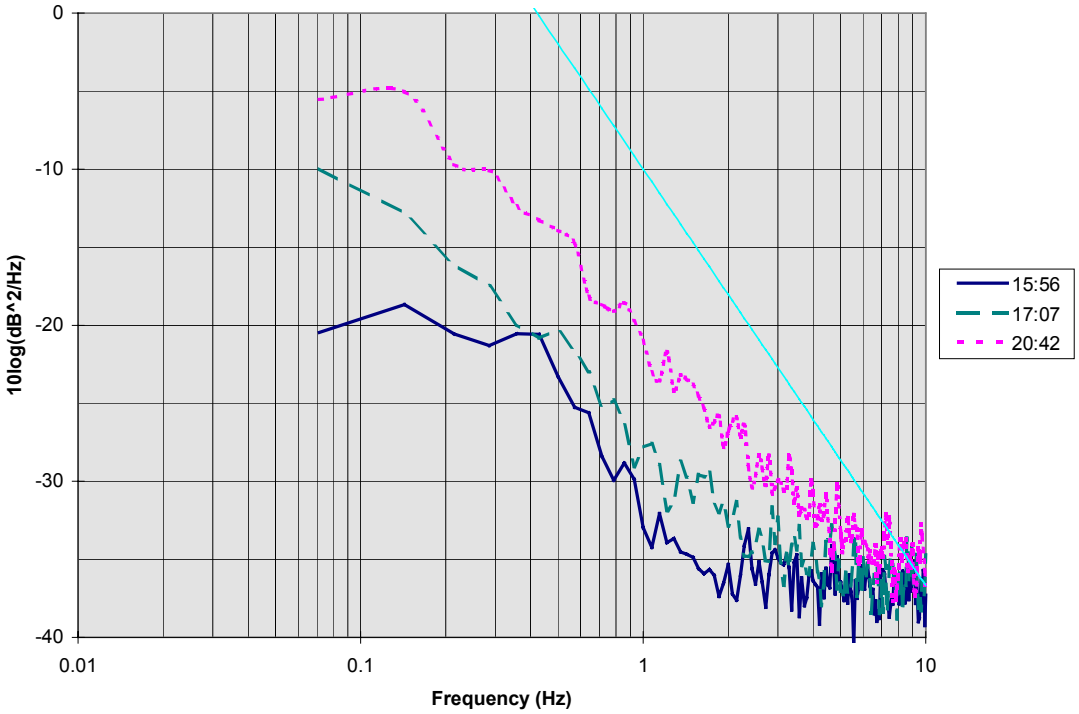

Figure 4.3 Beacon Amplitude Spectra from Afternoon June 24

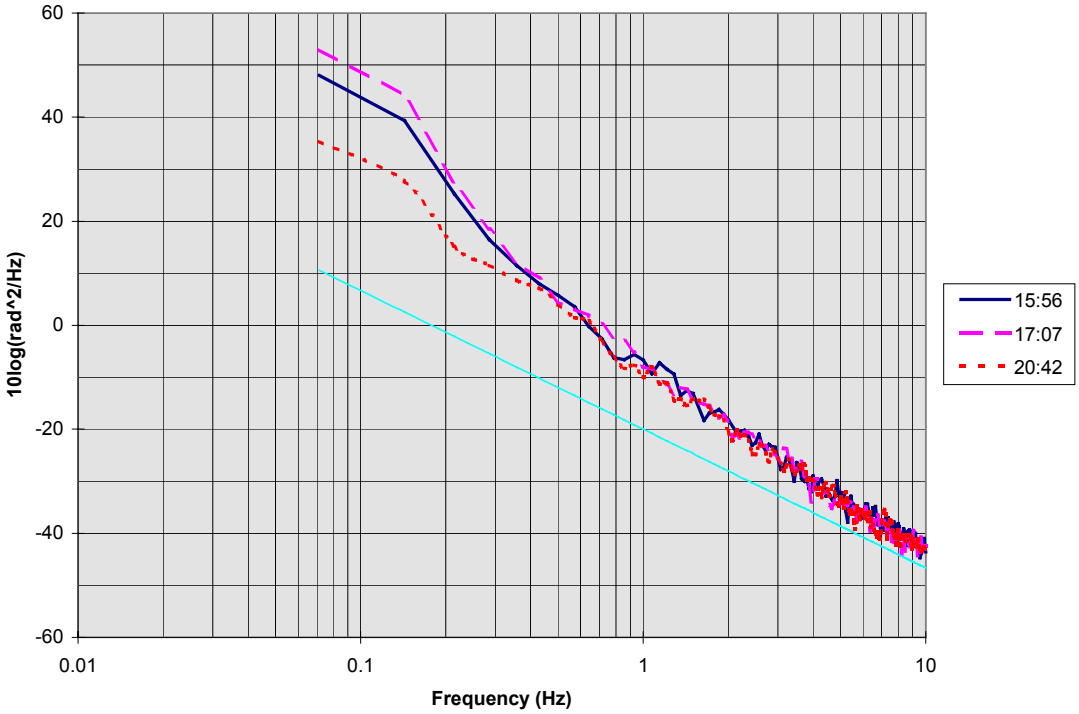

Figure 4.4 Beacon Phase Spectra from Afternoon June 24

4.1.2 Beacon Measurements from June 18

June 18 was a mostly overcast day in which the humidity was near 100% for much of the afternoon. A brief rain shower fell shortly after 11:00EDT, and the temperature and dew point remained quite steady throughout the afternoon hours. A summary of six measurements made on this day is given in Table 4.2. The scintillation observed near midday was quite mild with very little phase noise elevation. Figure 4.5 shows this mild amplitude scintillation, with a Fresnel frequency of about 1.0Hz. The phase noise in Figure 4.6 has approximately a $f^{-11/3}$ frequency dependence, and is nearly a straight line. This corresponds to the phase noise floor for this beacon receiver system. The phase noise deviation was measured in the range of 15-20rad.

Later in the day, as shown in Figure 4.7, the amplitude deviation increased to about 0.3dB. The Fresnel frequency dropped to near 0.2Hz. Figure 4.8 shows that there was some noticeable phase scintillation as well. The frequency roll-off for the 16:01 data was measured to be $f^{-1.4}$, which is significantly below the theoretical value due to the variable cloud cover. The overcast skies started to break up during this time, so this increased lower-frequency scintillation is most likely the effects of individual clouds. The more uniform overcast skies earlier in the day resulted in much less scintillation than the intermittent partly cloudy skies. This increase in the scintillation level may also be due to the increased solar heating, resulting in more atmospheric turbulence.

Table 4.2 Beacon Measurement Data from June 18

Time (EDT)	Magnitude deviation	Angle deviation	Temperature	Dew point	High wind speed
11:18	0.119 dB	18.3 rad	71.1°F	70.8°F	6 mph
12:12	0.102 dB	19.8 rad	70.5°F	70.5°F	9 mph
13:27	0.073 dB	14.9 rad	70.6°F	70.6°F	12 mph
14:12	0.246 dB	85.1 rad	71.1°F	71.1°F	14 mph
14:37	0.332 dB	49.0 rad	71.9°F	71.3°F	7 mph
16:01	0.315 dB	21.6 rad	76.7°F	71.3°F	9 mph

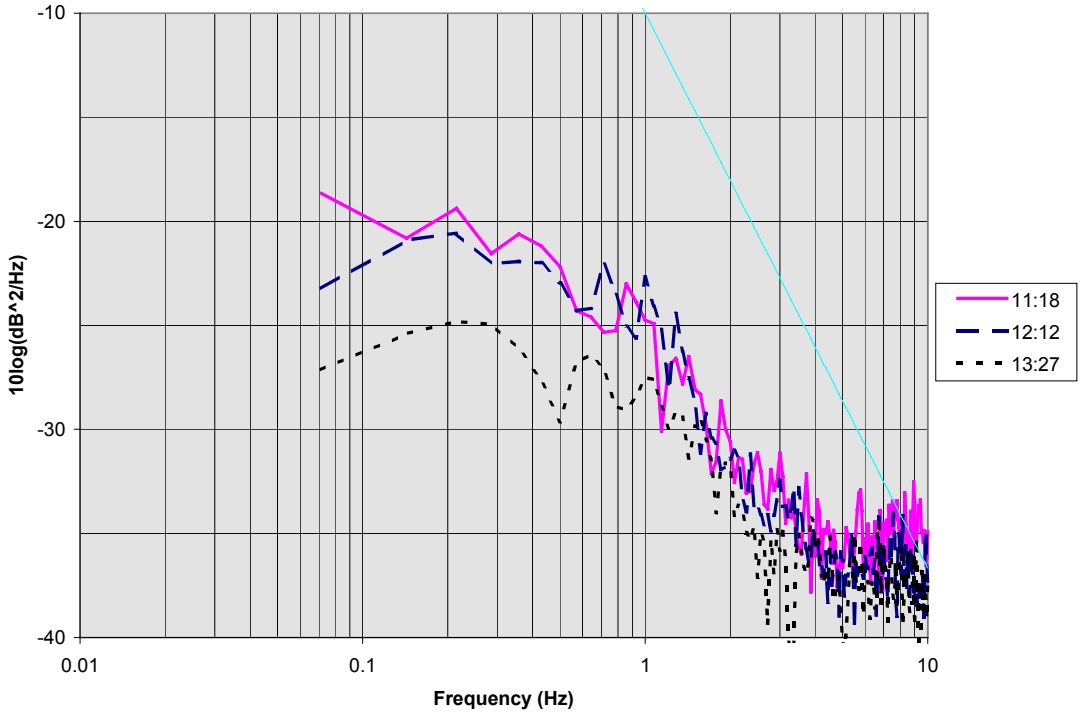

Figure 4.5 Beacon Amplitude Spectra from Midday June 18

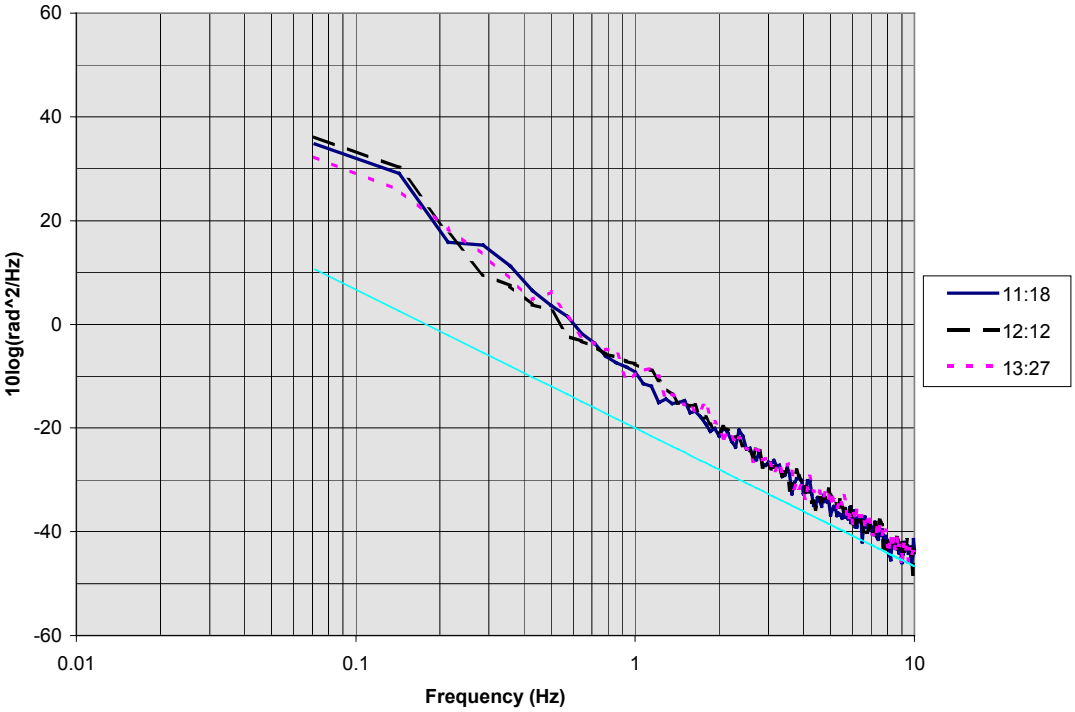

Figure 4.6 Beacon Phase Spectra from Midday June 18

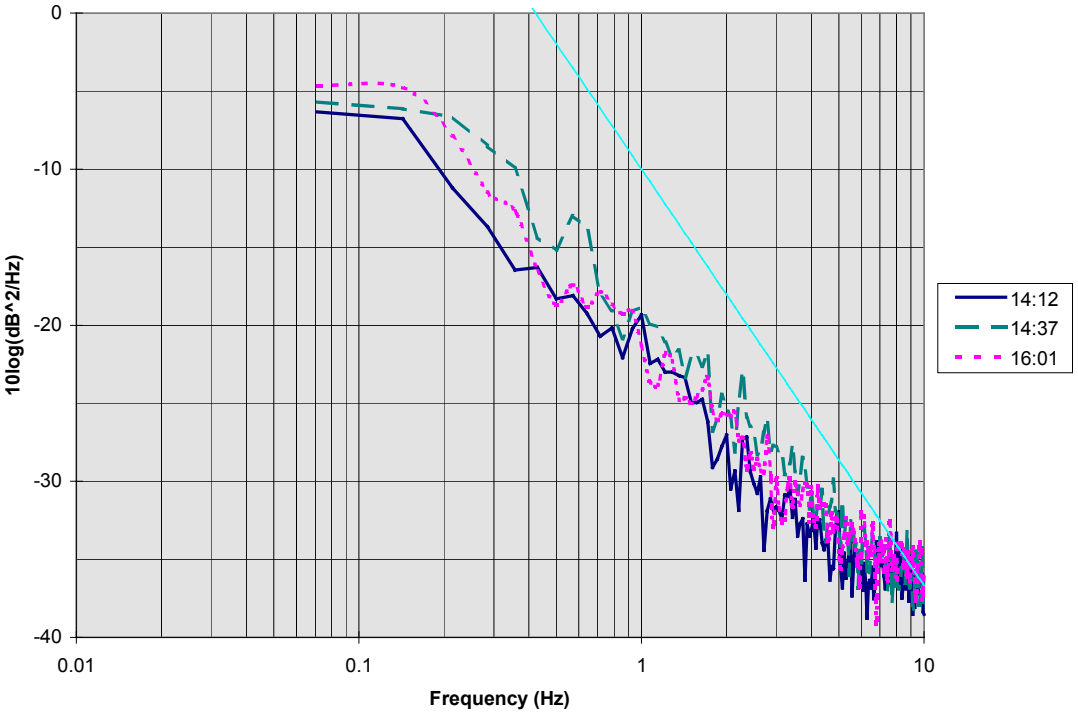

Figure 4.7 Beacon Amplitude Spectra from Afternoon June 18

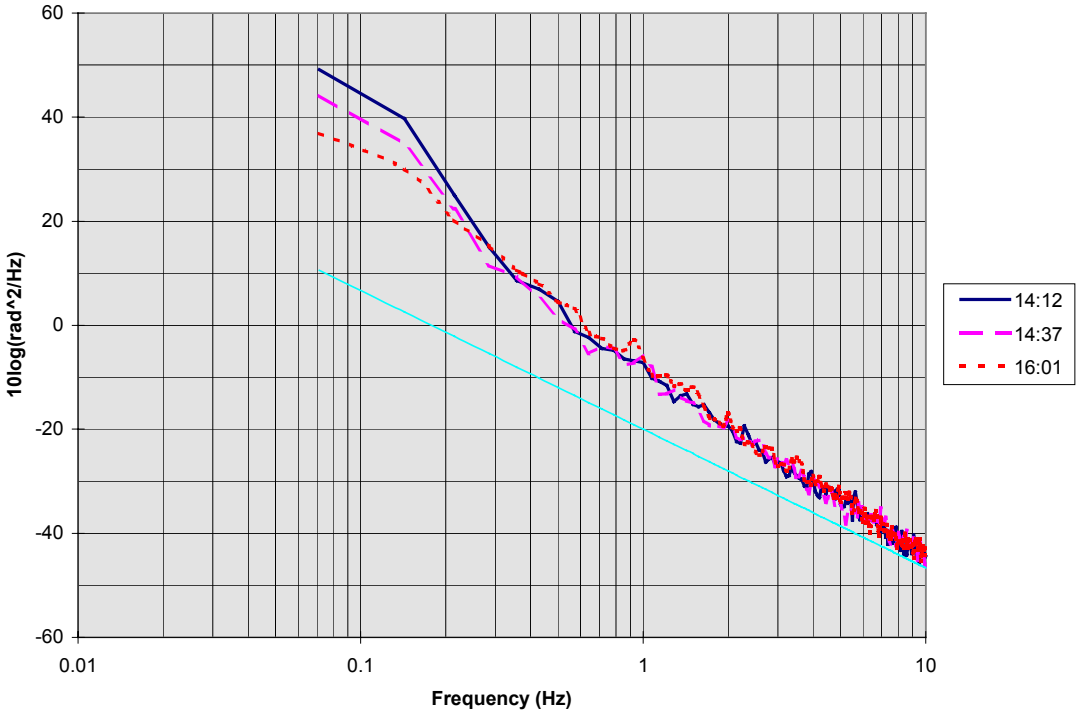

Figure 4.8 Beacon Phase Spectra from Afternoon June 18

4.1.3 Beacon Measurements from May 23

The weather on the afternoon of May 23 was warm and overcast. The scintillation observed on this afternoon tended to have very low Fresnel frequencies, which is typical during cloudy conditions. Three measurements are summarized in Table 4.3.

The three amplitude spectra plotted in Figure 4.9 show two general forms. Two of the curves have spectra which are still increasing at the lower frequency limit, with a rate which is somewhat shallower than the expected $f^{-8/3}$ rate. The actual measured rate for the 17:10 data is $f^{-1.9}$. The other curve levels off at about 0.2Hz, and shows a roll-off rate much closer to $f^{-8/3}$. We conclude that the first case (13:50 and 17:10) shows the effects of clouds on the scintillation spectral shape and Fresnel frequency, while the other case (15:31) is likely the "clear-air" situation. Of the three phase spectra shown in Figure 4.10, one of the curves shows a pronounced elevation in phase noise below 0.3Hz, which corresponds closely to the roll-off frequency observed in the corresponding amplitude spectrum.

Table 4.3 Beacon Measurement Data from May 23

Time (EDT)	Magnitude deviation	Angle deviation	Temperature	Dew point	High wind speed
13:50	0.085 dB	33.9 rad	77.9ºF	62.4ºF	9 mph
15:31	0.190 dB	161.4 rad	81.6ºF	61.5ºF	11 mph
17:10	0.086 dB	39.1 rad	80.0ºF	62.9ºF	11 mph

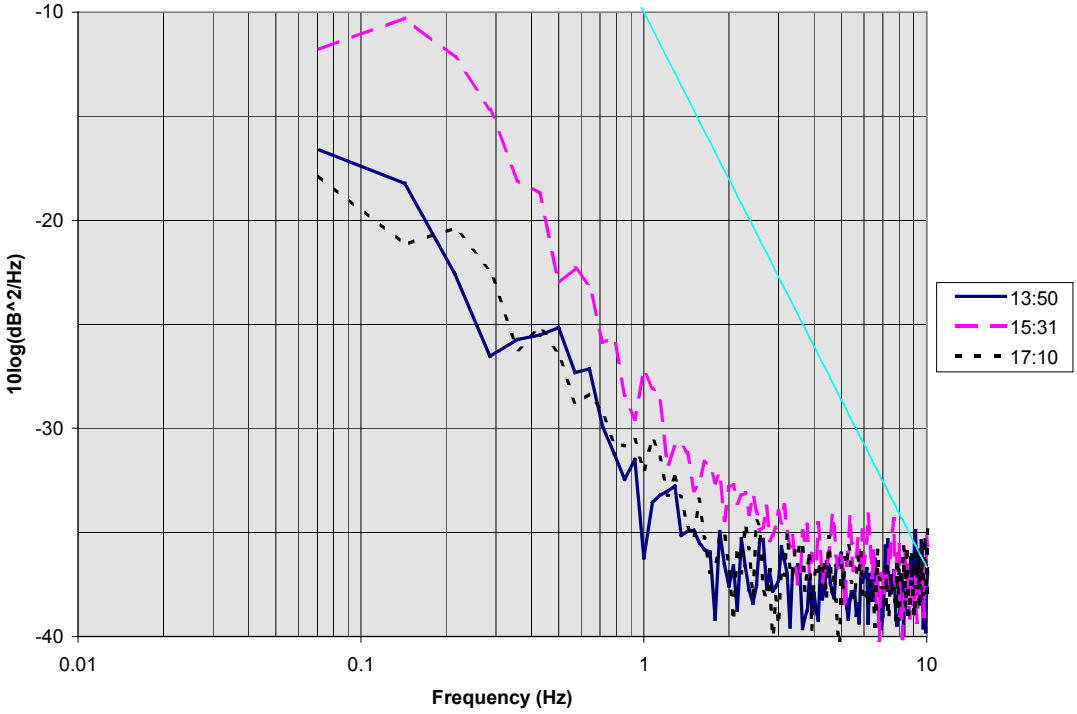

Figure 4.9 Beacon Amplitude Spectra from Afternoon May 23

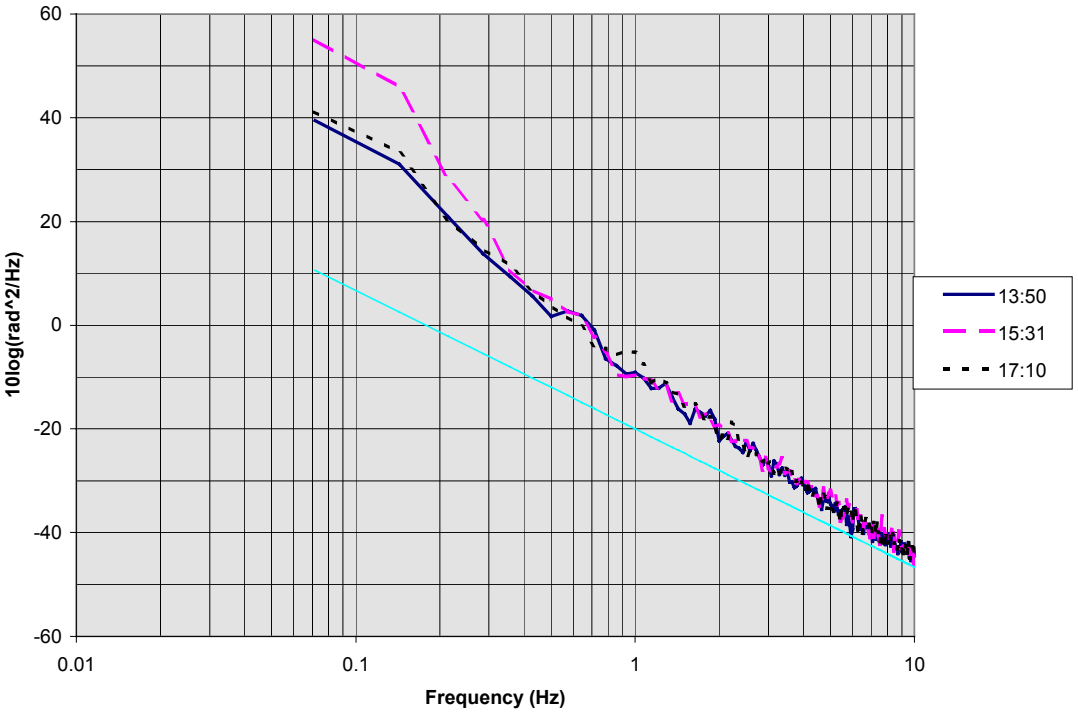

Figure 4.10 Beacon Phase Spectra from Afternoon May 23

4.1.4 Beacon Measurements from April 21

The measurements performed on April 21 are similar to the measurements recorded during midday on June 18. The weather on the afternoon of April 21 was warm and humid, with partly cloudy skies. The wind speeds recorded on the ground were relatively high, up to 18 mph. The high Fresnel frequency implies the combination of a low turbulent layer altitude, with a high transverse velocity.

A summary of three measurements made on this day is given in Table 4.4. The three amplitude spectra shown in Figure 4.11 are similar to those shown in Figure 4.5. All three spectra show a high Fresnel frequency near 1Hz, but with a very low peak level (below the $0.01 dB^2/Hz$ level). The measured frequency dependence for the 12:07 data was $f^{2.1}$. Phase scintillation was indicated by all three measurements, as shown in Figure 4.12. However the strength of the phase scintillation was variable, and not well correlated with the strength of the amplitude scintillation.

Table 4.4 Beacon Measurement Data from April 21

Time (EDT)	Magnitude deviation	Angle deviation	Temperature	Dew point	High wind speed
12:07	0.123 dB	41.7 rad	70.9ºF	61.0ºF	18 mph
12:16	0.093 dB	93.0 rad	71.2ºF	61.5ºF	13 mph
12:28	0.090 dB	18.5 rad	71.3ºF	61.4ºF	12 mph

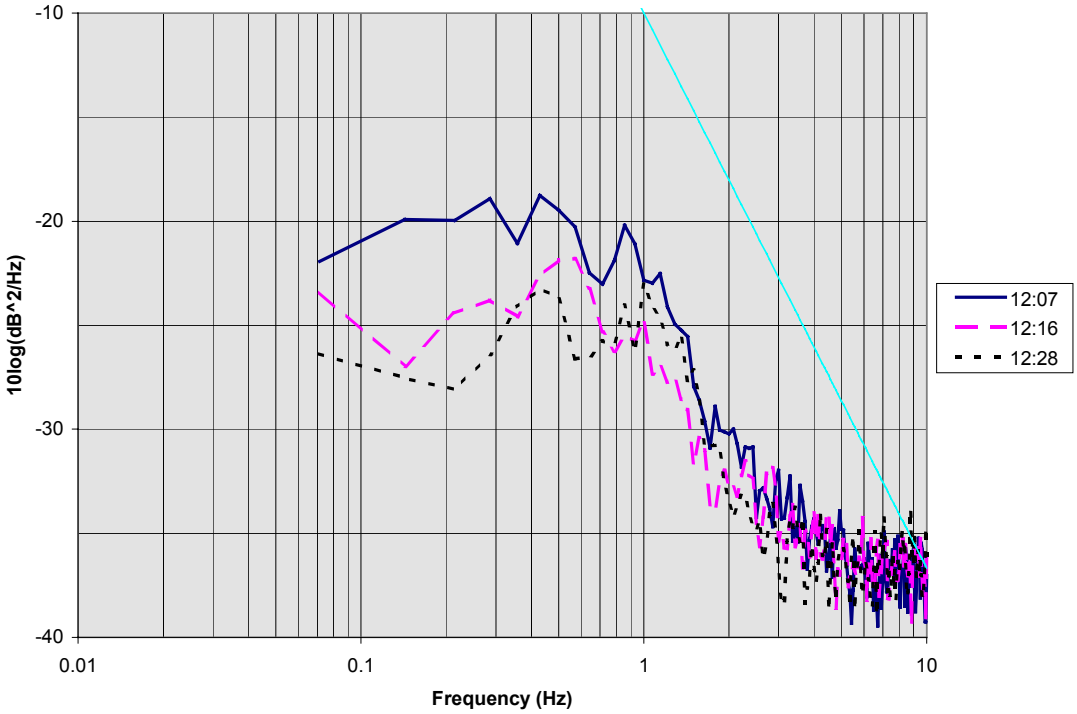

Figure 4.11 Beacon Amplitude Spectra from Midday April 21

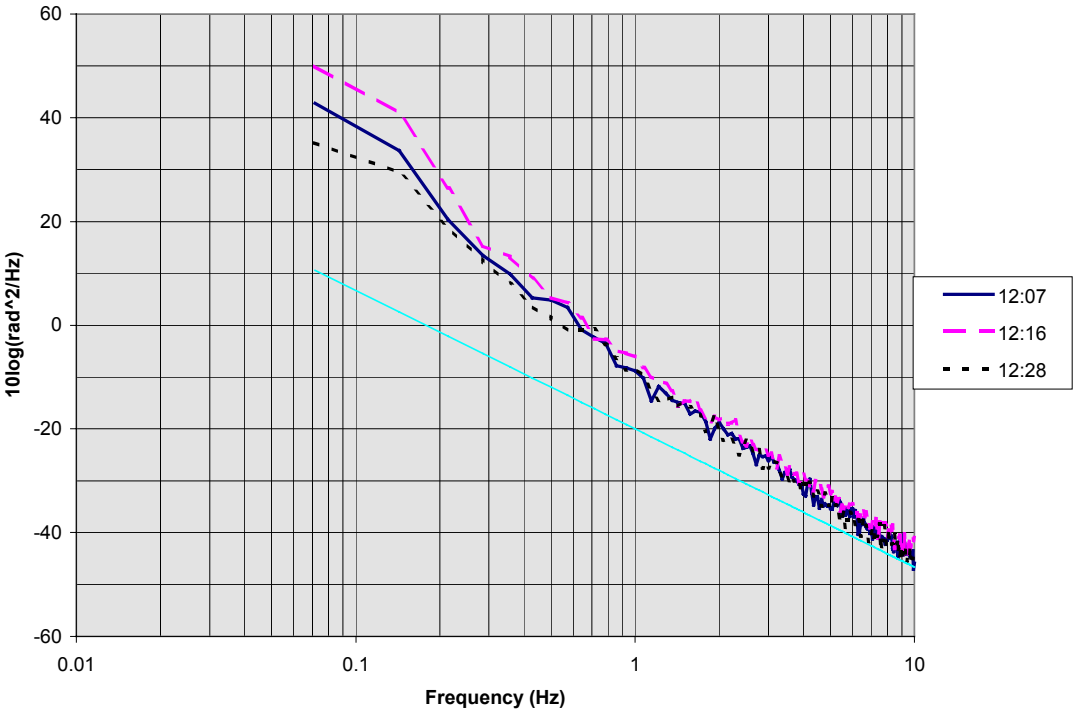

Figure 4.12 Beacon Phase Spectra from Midday April 21

4.1.5 Beacon Measurements from April 17

The measurements performed on April 17 demonstrate that high humidity levels are not necessary in order to have strong scintillation. The weather on the afternoon of April 17 was dry and clear, with strong gusty winds near 20mph. The high winds apparently created strong turbulence in the boundary layer. This turbulence was strong enough to create the most intense amplitude scintillation measured during this phase of the research.

A summary of three measurements made on this day is given in Table 4.5. The three amplitude spectra shown in Figure 4.13 are similar in shape and magnitude. All three spectra show a Fresnel frequency near 0.1Hz, and a peak level near 1dB^2/Hz.). The measured frequency dependence for the 14:34 data was $f^{-1.7}$. The strength of the phase noise shown in Figure 4.14 is inversely related to the strength of the amplitude variations. The strongest phase scintillation of the three measurements was recorded when the amplitude scintillation (and the wind) was weakest.

Table 4.5 Beacon Measurement Data from April 17

Time (EDT)	Magnitude deviation	Angle deviation	Temperature	Dew point	High wind speed
14:00	0.229 dB	133.0 rad	60.5°F	32.7°F	13 mph
14:34	0.458 dB	51.7 rad	61.5°F	30.6°F	20 mph
14:40	0.395 dB	41.4 rad	61.4°F	30.1°F	19 mph

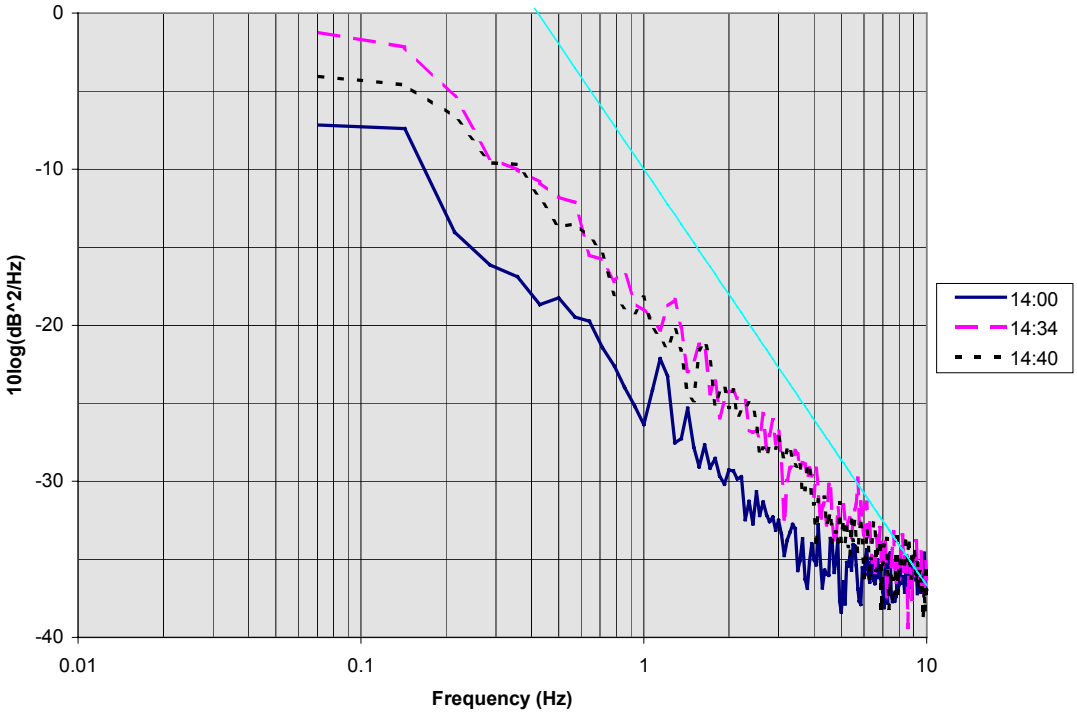

Figure 4.13 Beacon Amplitude Spectra from Midday April 17

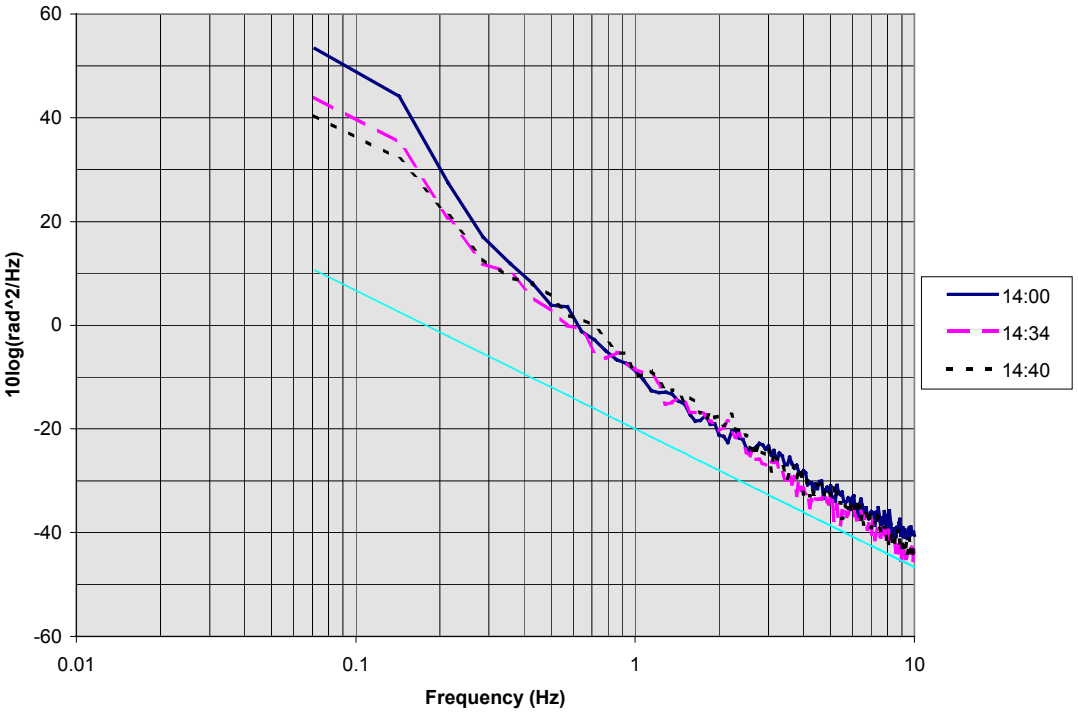

Figure 4.14 Beacon Phase Spectra from Midday April 17

4.1.6 Beacon Measurements from March 13

Several rain showers occurred during the afternoon of March 13. The first, at 12:30EST, resulted in 0.04in of accumulation. Later showers at 15:00 and 15:20 added an additional 0.02in and 0.01in, respectively. The skies remained overcast for most of the day, and wind speed increased as the day progressed. As indicated in Table 4.6, the temperature was nearly constant, but the dew point depression decreased throughout the day as more rain showers moved through the area.

The amplitude spectra shown in Figure 4.15 and Figure 4.17 indicate that the Fresnel frequency remained near 1.0Hz, but the overall scintillation level tended to increase as the day progressed. The shape of the spectra below the Fresnel frequency varies; flat in some cases and gently sloped in other cases. The measured frequency dependence for the 14:45 data was $f^{-2.2}$. This variation is the result of diversity in the overcast cloud layer. Of the phase spectra shown in Figure 4.16 and Figure 4.18, all show some phase scintillation effects except for the measurement at 15:20. This measurement was taken as a rain shower was ending, so this may demonstrate that the atmosphere is less turbulent after a rain shower has passed. As the rain was moving into the area, the measurement at 15:13 shows that the phase noise floor level increased slightly due to the reduction in the received carrier level.

Table 4.6 Beacon Measurement Data from March 13

Time (EST)	Magnitude deviation	Angle deviation	Temperature	Dew point	High wind speed
11:50	0.081 dB	60.4 rad	65.3°F	59.3°F	9 mph
12:05	0.127 dB	49.7 rad	65.1°F	59.5°F	7 mph
12:20	0.121 dB	25.5 rad	65.1°F	59.8°F	8 mph
14:45	0.248 dB	24.9 rad	62.9°F	60.2°F	7 mph
15:13	0.220 dB	25.2 rad	63.2°F	61.4°F	11 mph
15:20	0.144 dB	11.4 rad	63.3°F	61.5°F	17 mph

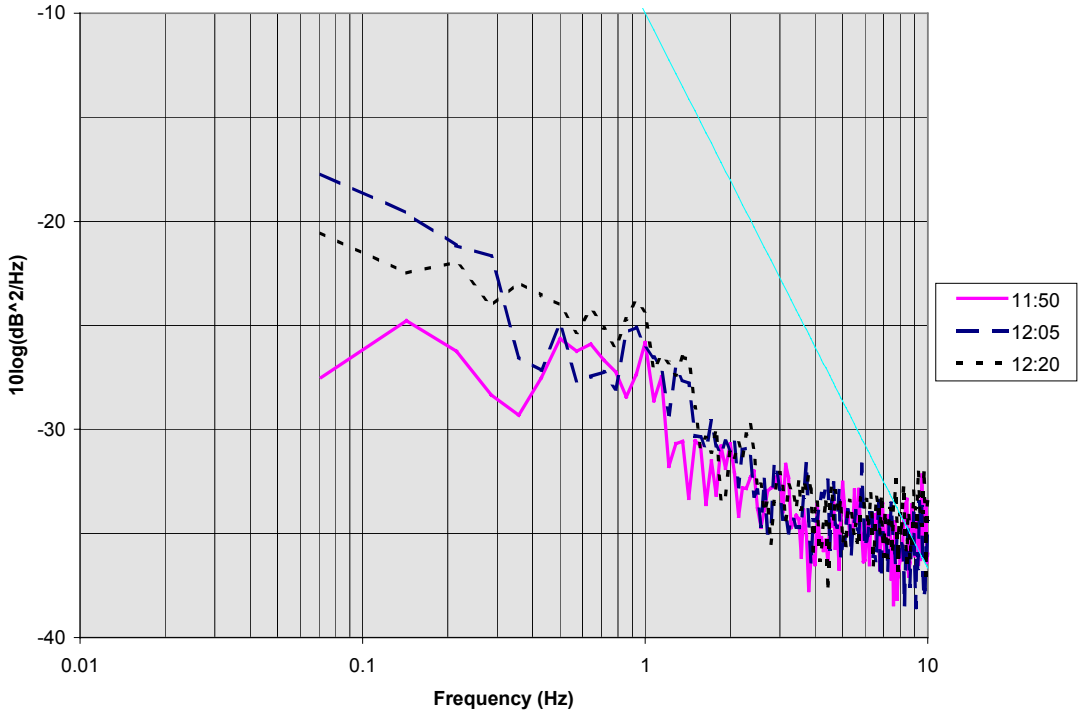

Figure 4.15 Beacon Amplitude Spectra from Midday March 13

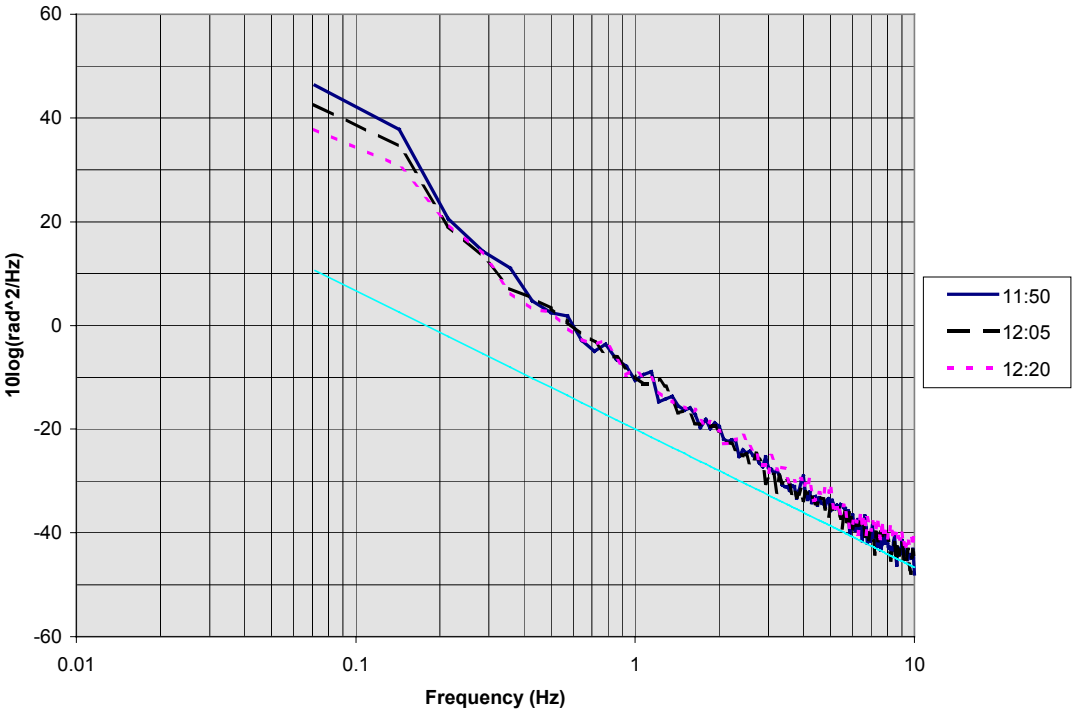

Figure 4.16 Beacon Phase Spectra from Midday March 13

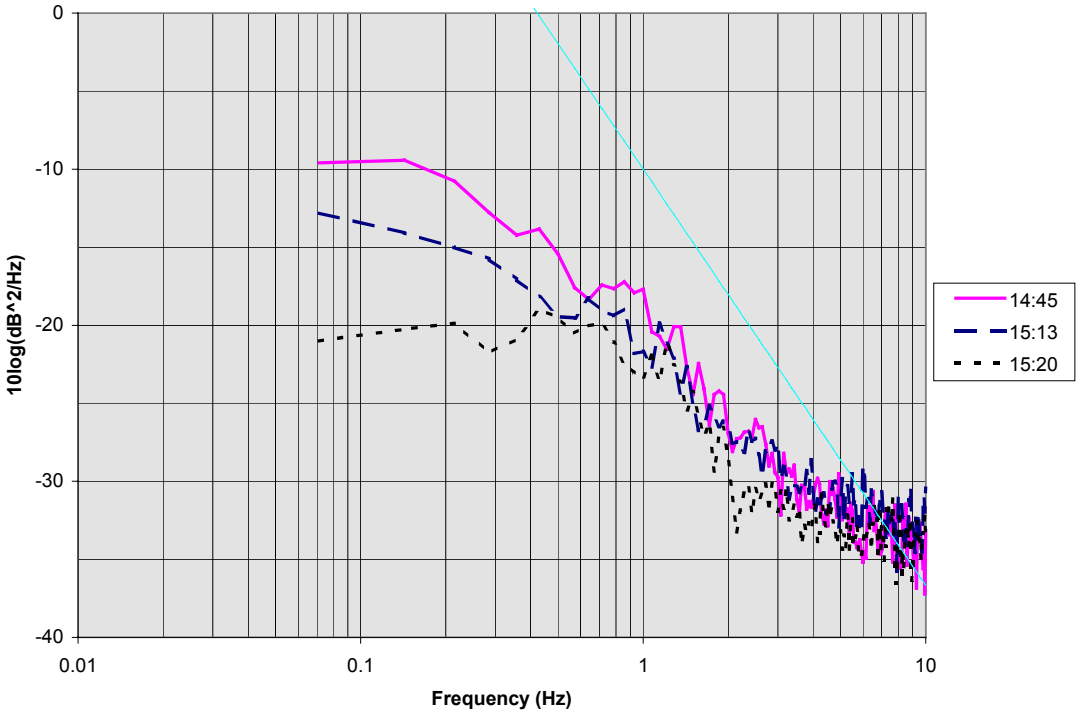

Figure 4.17 Beacon Amplitude Spectra from Afternoon March 13

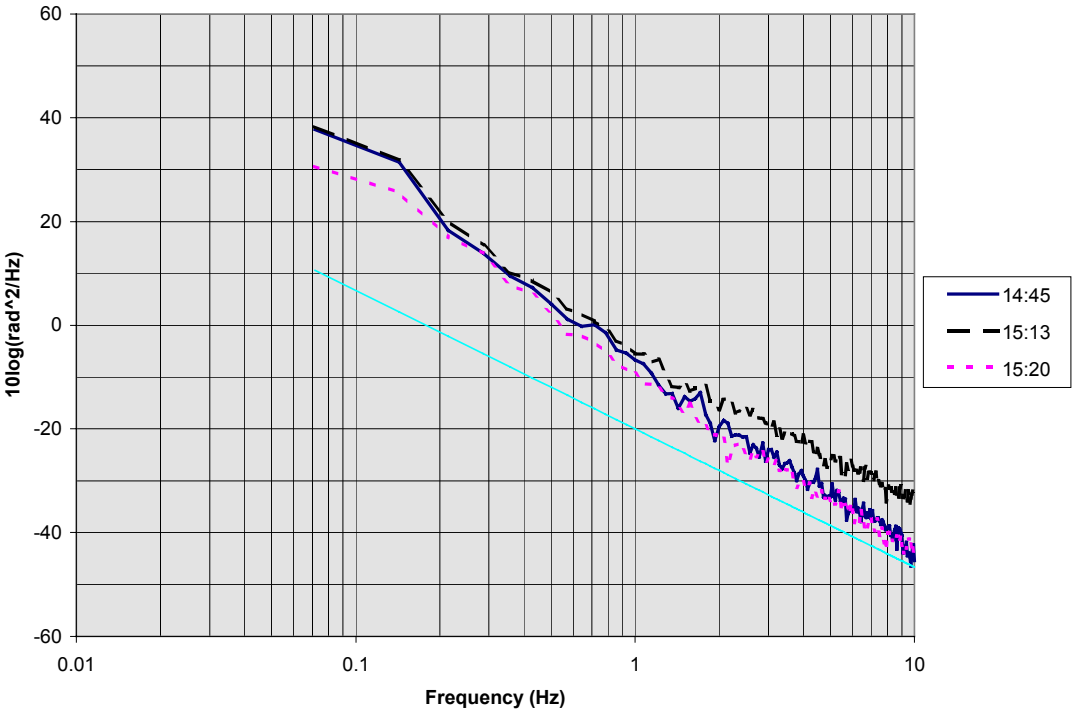

Figure 4.18 Beacon Phase Spectra from Afternoon March 13

4.2 Carrier Wave Measurements

The addition of the solid-state power amplifier allowed for carrier measurements to be performed of signals that are relayed through the ACTS MSM transponder. These measurements were conducted from July 1997 through December 1997, usually in conjunction with BER digital data measurements. As with the beacon, the carrier was downconverted to approximately 2kHz, then digitally sampled at a 20kHz rate. The same Matlab processing was used to derive amplitude and phase spectra of the carriers, along with monitoring of the carrier power level.

The original carrier transceiver hardware system utilized the 1W TWT power amplifier, along with the rest of the system shown in Figure 3.3. One key measurement performed with this system initially was a characterization of the power compression curve of the TWT amplifier. The gain response of the amplifier is measured by varying the power level of the input 270MHz signal and monitoring the received C/N ratio. The maximum measured C/N ratio with this system was 51dB (in a 1kHz noise bandwidth). This measurement is very near the theoretical value computed in Section 3.2.

When the uplink amplifier is replaced with a solid-state model, additional measurements were performed to verify the system performance. With the new power amplifier, the maximum received C/N was reduced to 47dB, due to two factors. The solid-state power amplifier is rated for a 1W output, but in reality this power level is only reached by driving the amplifier into hard saturation. Also, the input mixer to the power amplifier is only capable of providing a -10dBm signal. An input signal of 0dBm is required to achieve

a 1W (30dBm) output, but a -10dBm input will still produce an output signal over 26dBm. The power response characteristic for the transceiver system is shown in Figure 4.19.

In the following sections, carrier measurements are presented from several different days to illustrate some of the differences observed in scintillation characteristics. The presentation format is identical to that used for the beacon data. All of the spectra shown are the averages of twenty 15-second power spectral densities.

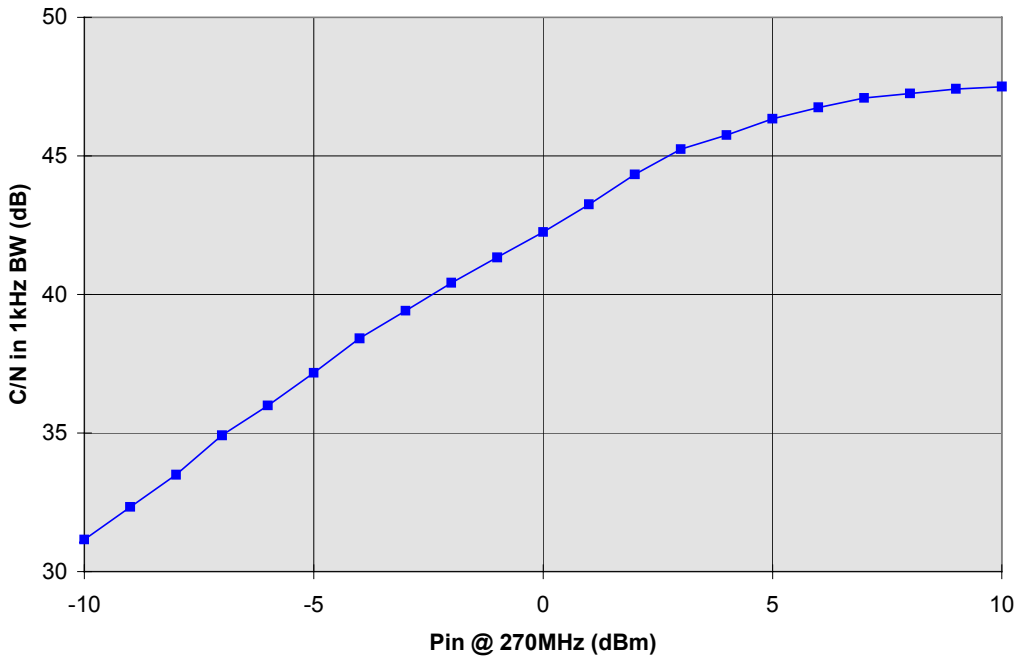

Figure 4.19 Transceiver System Uplink Amplifier Power Response

4.2.1 Carrier Measurements from July 22

On the evening of July 22, the remnants of a hurricane passed though the Atlanta area. Fortunately, ACTS transponder time was available during this event. The weather during the afternoon and evening was overcast and humid. Rain was recorded at the site during the hour of 15:00EDT, then again at 21:00. Six measurements are presented here from the period between the two rainstorms. During the first three measurements, the local winds were fairly strong, but the latter three measurements were taken when the surface winds were very calm. Conditions during the six measurements are summarized in Table 4.7.

The amplitude spectra for these measurements are presented in Figure 4.20 and Figure 4.22. All of the measurements show fairly strong amplitude scintillation. The measured frequency dependence for the 20:10 data was $f^{2.4}$. The earlier set of measurements tend to show more variance, while the latter set appears more consistent. The phase spectra for these measurements are shown in Figure 4.21 and Figure 4.23. The phase variance observed is near normal for these carrier measurements, and little elevation is seen in the lower frequencies of the phase spectra. So while there was appreciable amplitude scintillation, phase scintillation was not obvious.

Table 4.7 Carrier Measurement Data from July 22

Time (EDT)	Magnitude deviation	Angle deviation	Temperature	Dew point	High wind speed
18:40	0.057 dB	12.9 rad	75.0ºF	75.0ºF	8 mph
19:10	0.181 dB	8.63 rad	75.1ºF	75.1ºF	11 mph
19:40	0.247 dB	9.16 rad	75.3ºF	75.3ºF	10 mph
20:10	0.123 dB	8.09 rad	75.5ºF	75.5ºF	1 mph
20:25	0.125 dB	8.04 rad	75.3ºF	75.3ºF	1 mph
20:40	0.213 dB	9.33 rad	75.3ºF	75.3ºF	1 mph

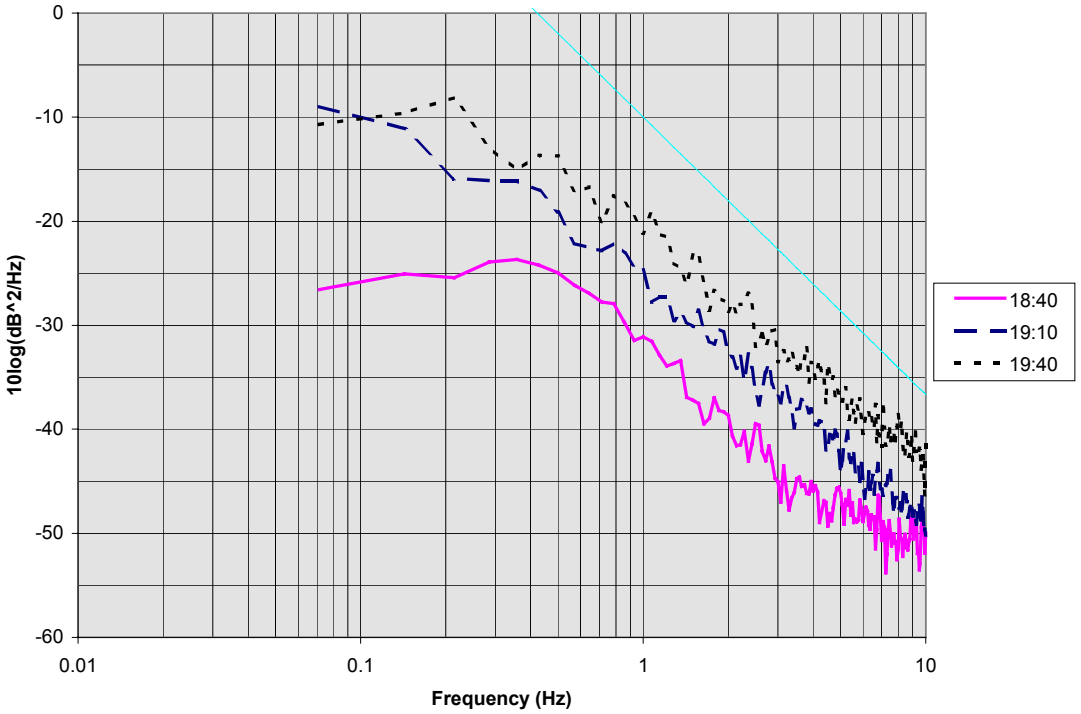

Figure 4.20 Carrier Amplitude Spectra from Afternoon July 22

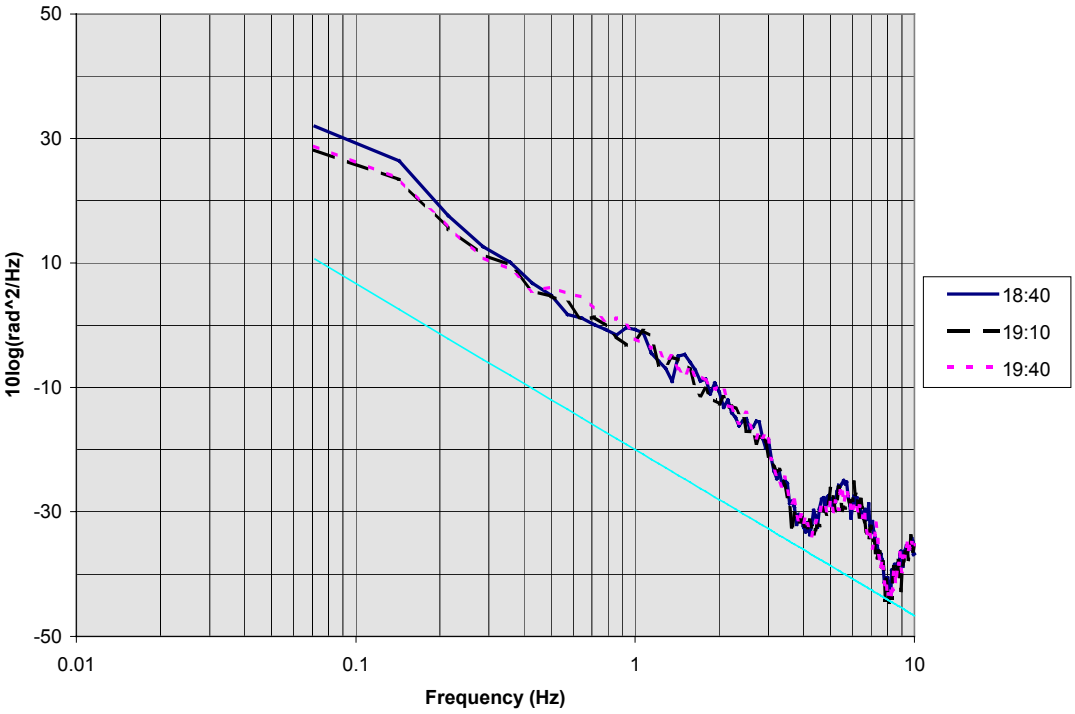

Figure 4.21 Carrier Phase Spectra from Afternoon July 22

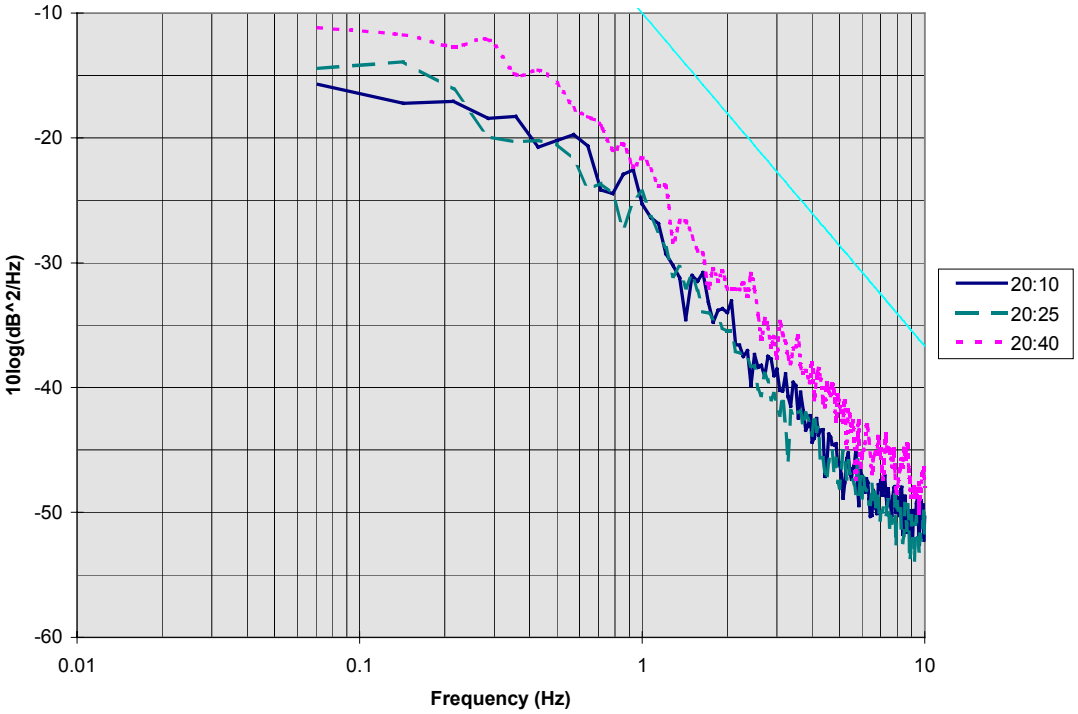

Figure 4.22 Carrier Amplitude Spectra from Evening July 22

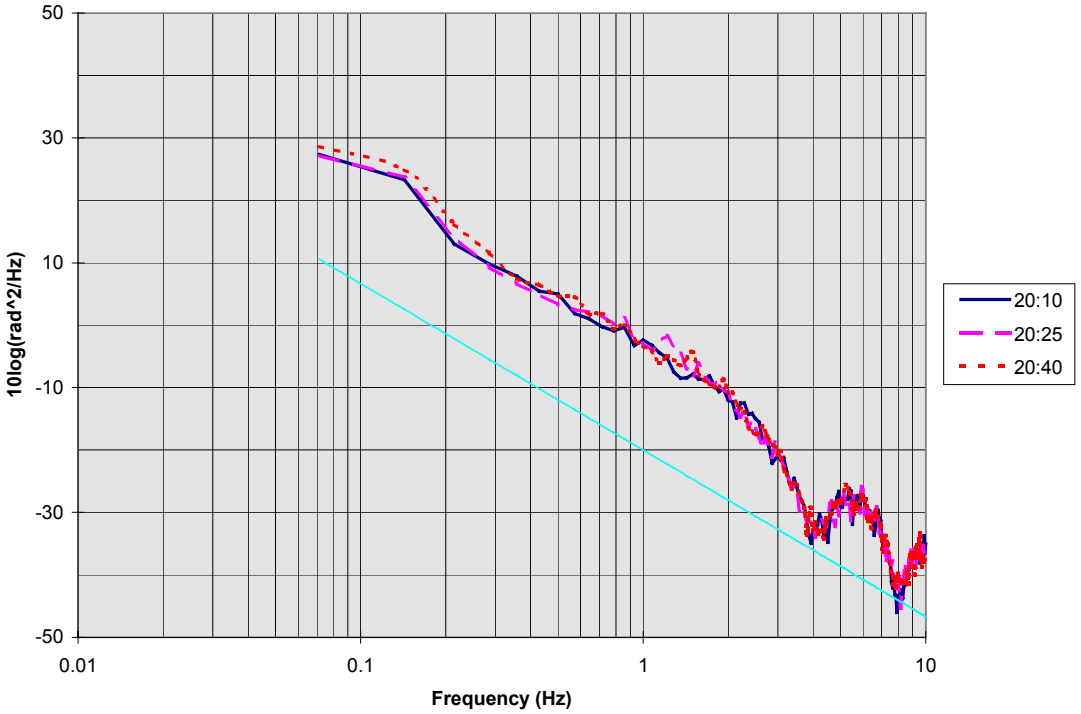

Figure 4.23 Carrier Phase Spectra from Evening July 22

4.2.2 Carrier Measurements from August 20

The weather on August 20 was warm and humid, with rain briefly during the afternoon. Heavy rain was measured at the site at about 14:00EDT. Six measurements are presented here from both before and after the rain storm. The first set of three measurements from before the rain were taken with temperatures near 87ºF and winds up to 10mph. After the rain passed through, temperatures dropped by about 10ºF, and the

winds became calmer. Conditions during the six measurements are summarized in Table 4.8.

The amplitude spectra for these measurements are presented in Figure 4.24 and Figure 4.26. The first set from before the rain show high levels of amplitude scintillation, but after the rain the scintillation levels were greatly reduced. The measured frequency dependence for the 15:40 data was $f^{-2.2}$. The phase spectra for these measurements are shown in Figure 4.25 and Figure 4.27. The phase data show a trend opposite to the amplitude data. The phase variance observed before the rain is near the norm for these carrier measurements. But, the second set of measurements from after the storm show a marked increase in the low frequency phase deviation. The data from August 20 show that both amplitude and phase scintillation were present, but not simultaneously. Also, the Fresnel frequency for phase and amplitude scintillation do not seem to match in this case. For the second set of measurement, the amplitude spectra roll off near 1Hz, but the phase spectra show elevation only below 0.2Hz. This may be due to effects of differing scales of turbulence on the scintillation. Phase scintillation is influenced much more by large-scale turbulence (near the outer scale) than amplitude scintillation, so this measurement may indicate differing turbulent scales at different levels in the troposphere.

Table 4.8 Carrier Measurement Data from August 20

Time (EDT)	Magnitude deviation	Angle deviation	Temperature	Dew point	High wind speed
13:00	0.298 dB	10.9 rad	86.4°F	73.5°F	9 mph
13:20	0.255 dB	8.60 rad	87.1°F	74.1°F	11 mph
13:40	0.374 dB	13.4 rad	87.7°F	73.3°F	11 mph
15:00	0.060 dB	23.9 rad	76.2°F	76.1°F	5 mph
15:20	0.054 dB	38.7 rad	76.8°F	76.8°F	3 mph
15:40	0.062 dB	31.1 rad	77.3°F	77.1°F	6 mph

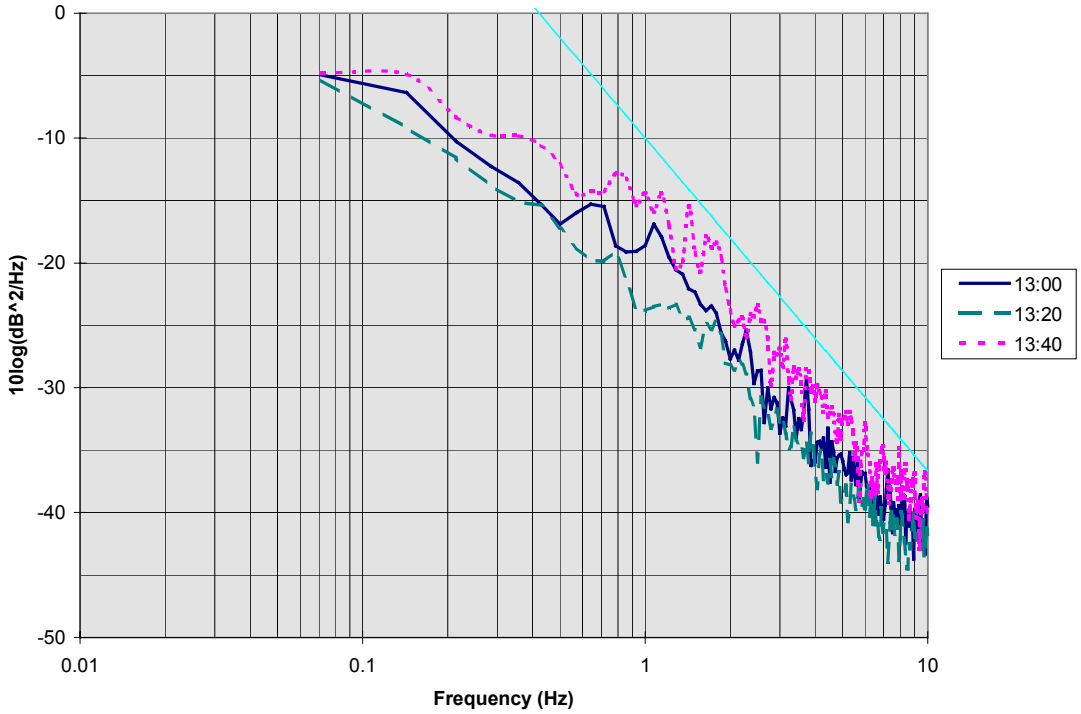

Figure 4.24 Carrier Amplitude Spectra from Midday August 20

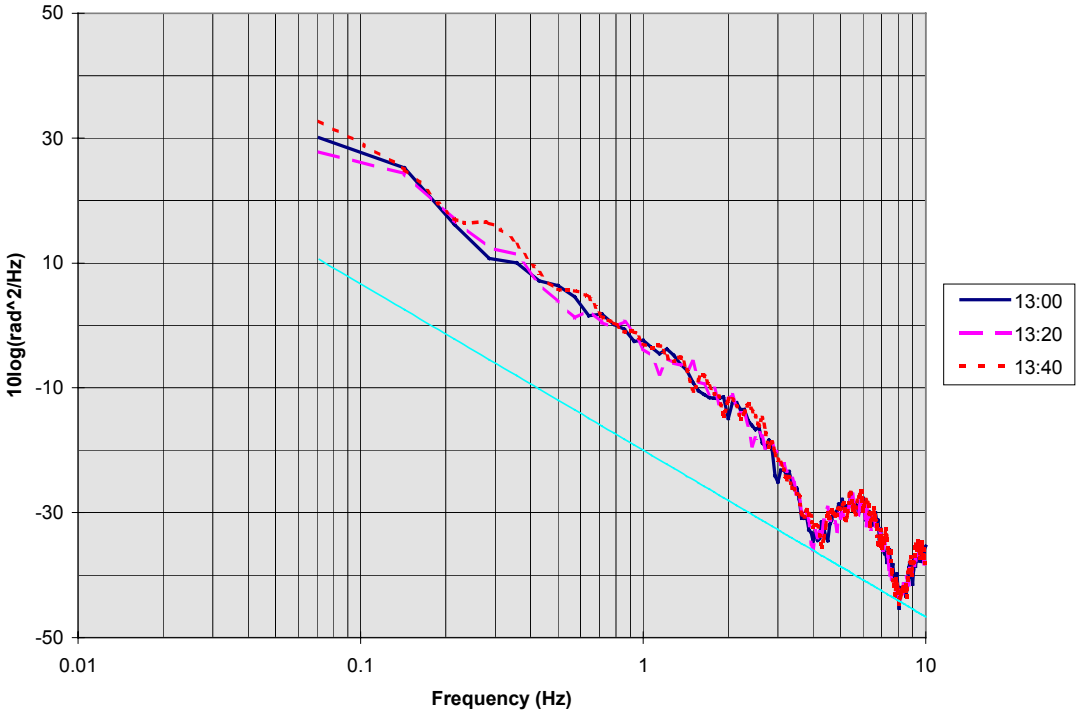

Figure 4.25 Carrier Phase Spectra from Midday August 20

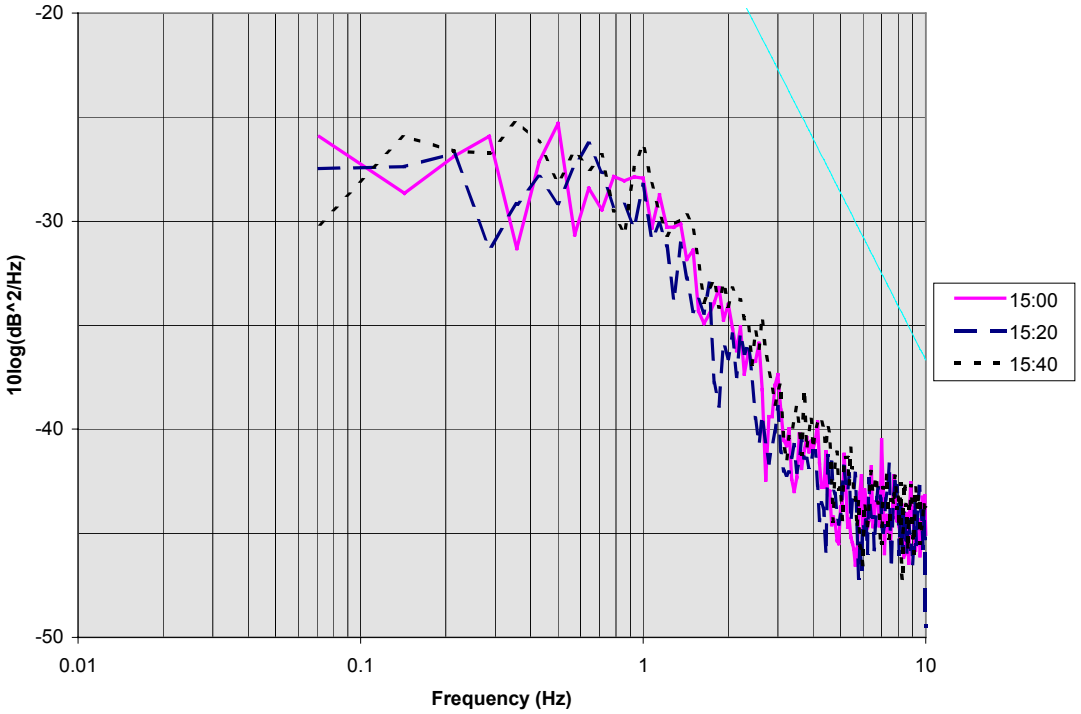

Figure 4.26 Carrier Amplitude Spectra from Afternoon August 20

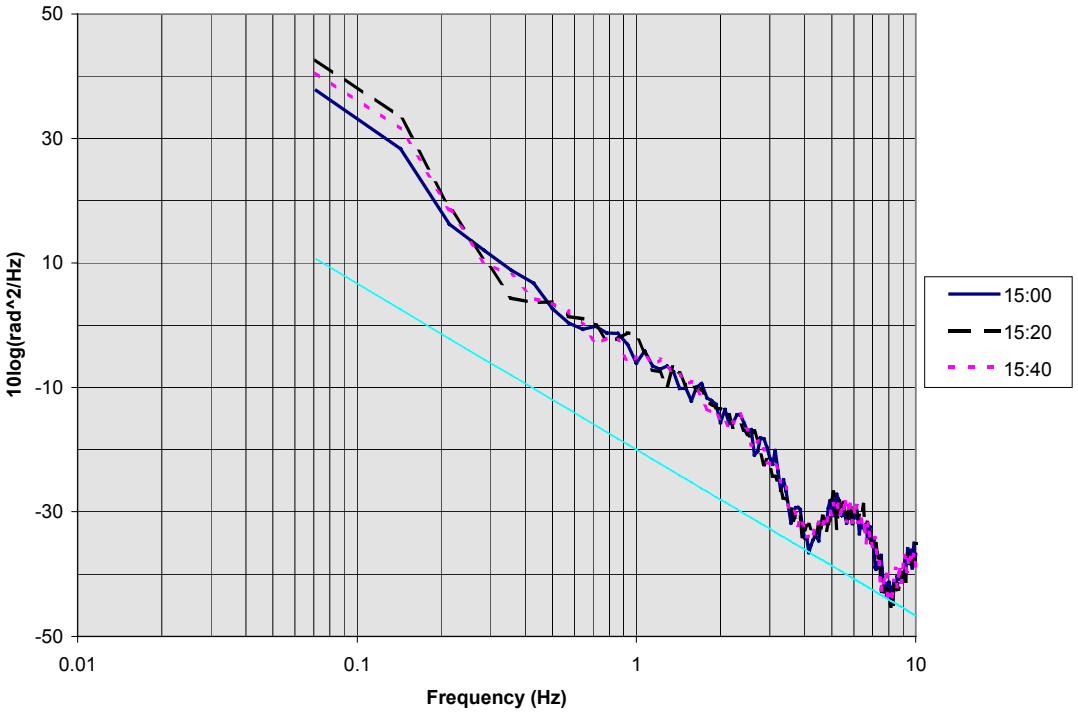

Figure 4.27 Carrier Phase Spectra from Afternoon August 20

4.2.3 Carrier Measurements from September 10

The weather on September 10 was warm and partly cloudy, with a light rain shower recorded at the site around 17:00. Six measurements are presented here from both before and after the rain shower. The first set of three measurements from before the rain were taken with temperatures near 80ºF. After the shower, temperatures dropped by about 10ºF,

and the air became dryer. Winds were moderate throughout the afternoon. Conditions during the six measurements are summarized in Table 4.9.

The amplitude spectra for these measurements are presented in Figure 4.28 and Figure 4.30. High scintillation levels were recorded throughout the day, but especially in the evening after the shower passed through. The measured frequency dependence for the 16:40 data was $f^{-2.5}$. The phase spectra for these measurements are shown in Figure 4.29 and Figure 4.31. The phase scintillation is strongest in the afternoon before the rain, but there are instances where both the amplitude and phase scintillation are fairly strong.

Table 4.9 Carrier Measurement Data from September 10

Time (EDT)	Magnitude deviation	Angle deviation	Temperature	Dew point	High wind speed
16:10	0.177 dB	24.4 rad	81.5ºF	64.1ºF	8 mph
16:40	0.094 dB	17.4 rad	80.7ºF	64.6ºF	4 mph
17:10	0.399 dB	34.1 rad	79.1ºF	66.8ºF	4 mph
19:20	0.297 dB	12.0 rad	69.0ºF	62.2ºF	5 mph
19:50	0.386 dB	12.6 rad	68.3ºF	61.9ºF	3 mph
20:20	0.408 dB	9.81 rad	67.2ºF	62.7ºF	6 mph

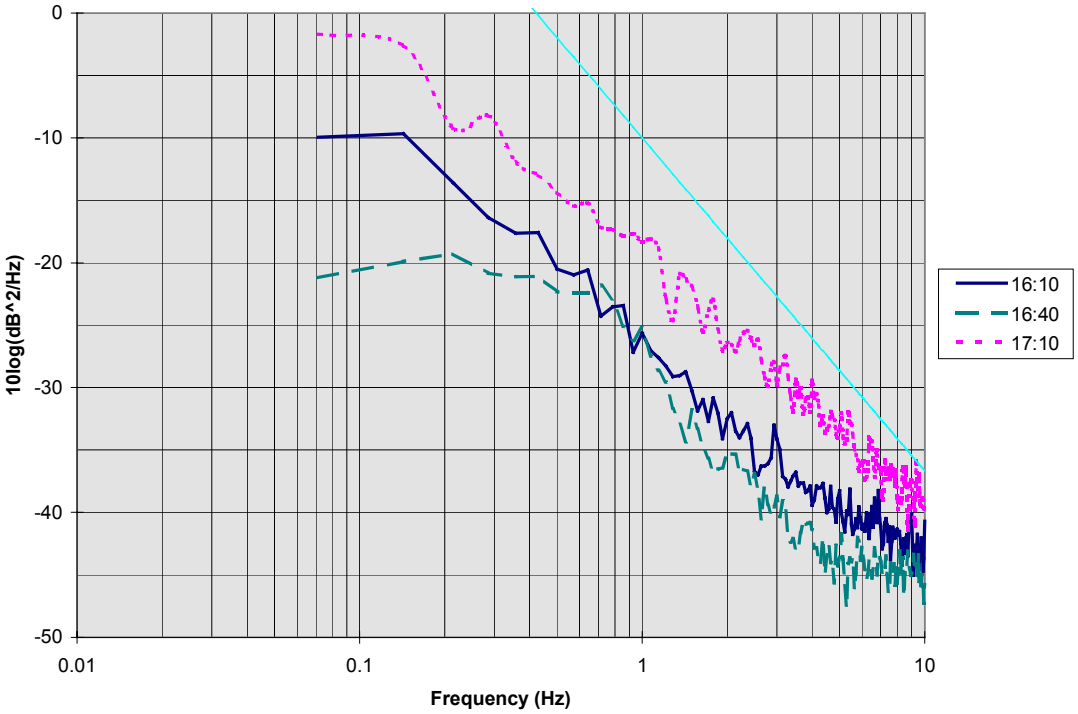

Figure 4.28 Carrier Amplitude Spectra from Afternoon September 10

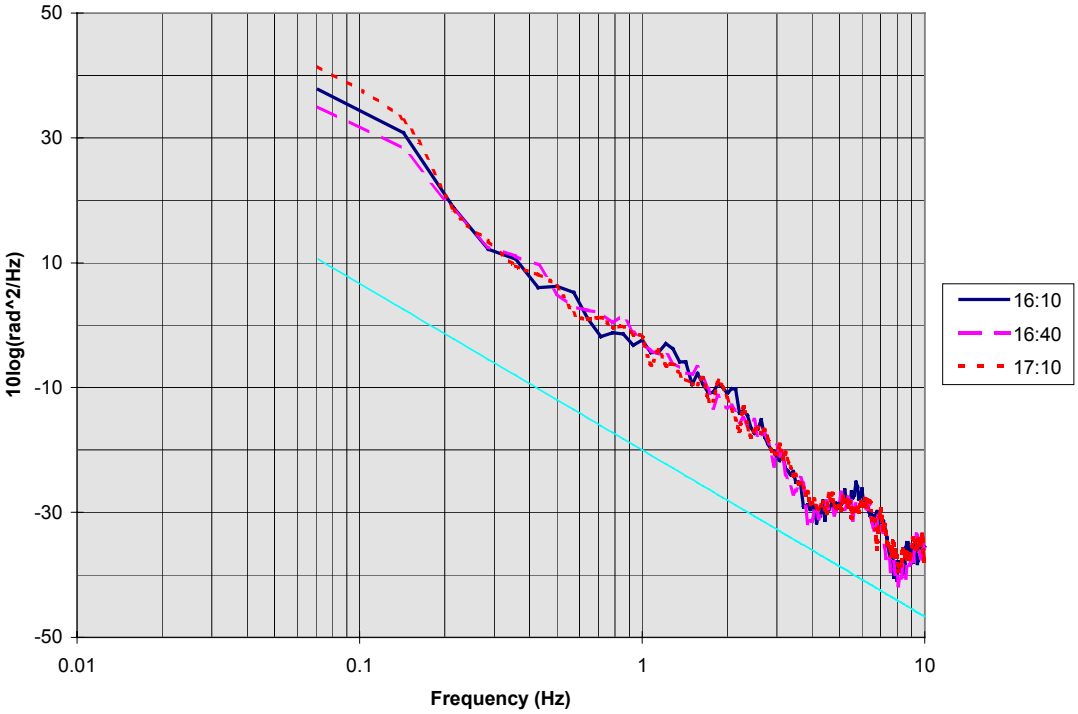

Figure 4.29 Carrier Phase Spectra from Afternoon September 10

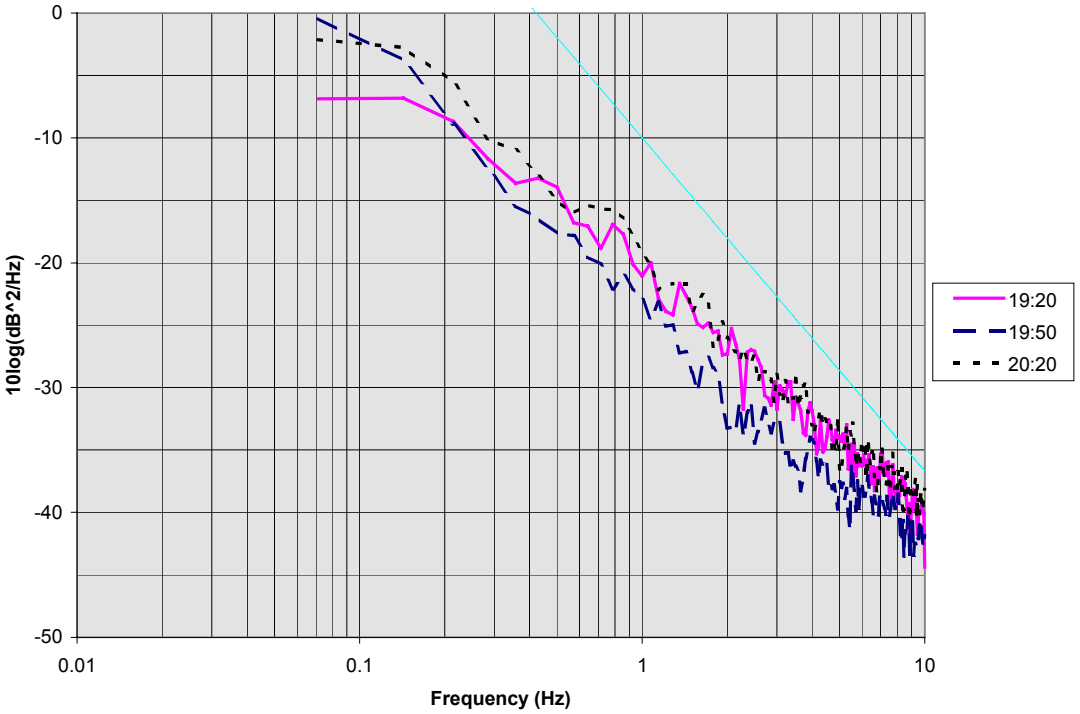

Figure 4.30 Carrier Amplitude Spectra from Evening September 10

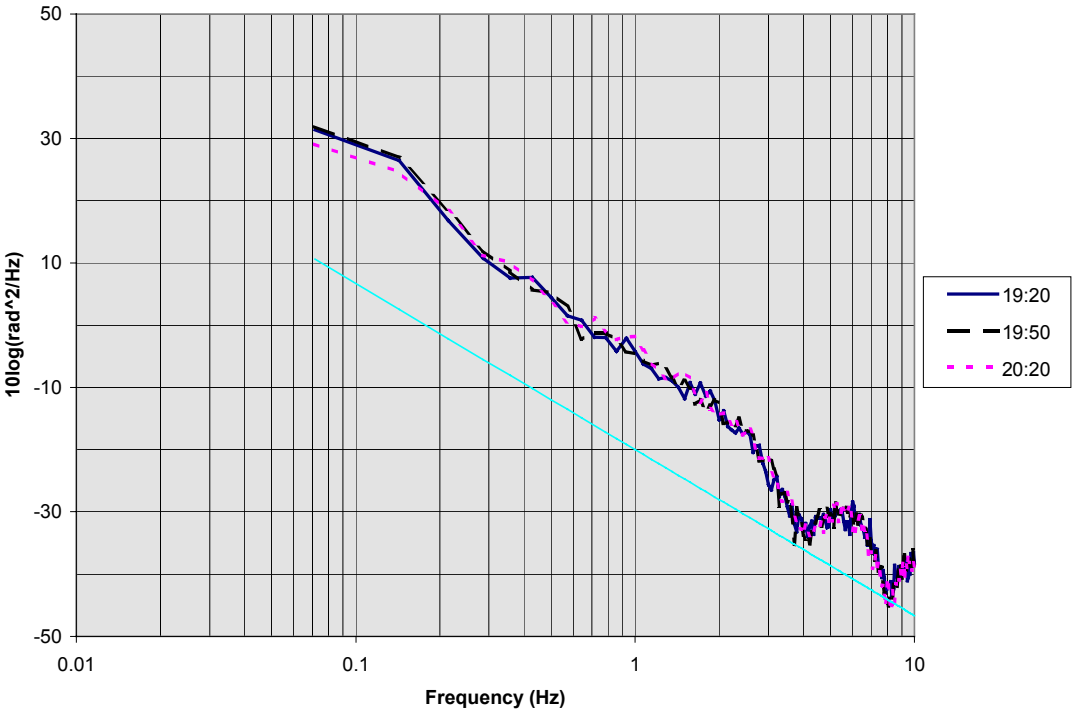

Figure 4.31 Carrier Phase Spectra from Evening September 10

4.3 Spread-Spectrum Modem Measurements

Two types of measurements have been performed with the spread-spectrum modem. The BER of the system has been measured as a function of C/N to compare the overall performance of the modem with theoretical predictions. Also, the BER of the system has been monitored as a function of time at a single C/N level while simultaneously monitoring a pilot carrier signal for scintillation variations.

The noise bandwidth seen by the CDMA demodulator is equivalent to the despread signal bandwidth. For a T1 data stream, the BPSK symbol rate is 1.544Mbps, which corresponds to a signal bandwidth of 3.088MHz. The maximum possible C/N in T1 mode for this system is therefore 12.1dB. The EB-100 modem operates in BPSK mode only, so the E_b/N_o ratio is simply twice the C/N ratio. The system therefore has a maximum E_b/N_o of about 15.1dB in clear conditions. For a BPSK system, the theoretical BER performance is given by (26)

$$\mathrm{BER} = \tfrac{1}{2}\,\mathrm{erfc}\left(\sqrt{E_b/N_o}\right), \tag{4.2}$$

where erfc( ) is the complementary error function.

4.3.1 BER Performance versus E_b/N_o

The performance of the modem in a stand-alone loopback configuration was first determined by combining the modulator output with a 70MHz noise source. The combined signal and noise were then connected to the input of the demodulator. By adjusting the output power from the modulator using a variable step attenuator, the BER can be determined as a function of E_b/N_o. Similarly, the performance through the ACTS transponder was also determined. The modulator has a function for disabling the modulation and measuring the characteristics of the unmodulated carrier wave. Then, using a spectrum analyzer, the C/N for this unmodulated carrier as a function of the attenuator setting is measured. This is then used to translate the attenuator setting to the equivalent E_b/N_o.

Measurements were made of the modem BER performance in T1 mode by attenuating the modulator output in 1dB steps. The tests were performed using 20chips/bit spreading and without spreading. For each option, five sets of measurements were performed. The spread-spectrum measurements through the satellite are tabulated in Table 4.7, along with the calculated averages and standard deviations for each power level. The unspread measurements through the satellite are listed in Table 4.8. Table 4.9 and Table 4.10 list the measurements obtained in the stand-alone loopback tests. The averages for all four cases are plotted in Figure 4.32, along with error bars indicating the standard deviation. The figure shows the measurements in a stand-alone loopback (solid symbols), through the satellite (open symbols), and the theoretical BPSK performance (solid line). The modem has a processing loss in the range of 1.5dB-2.0dB. When measured through the satellite, the

processing loss is slightly larger, most likely due to the effects of oscillator phase noise. The effects of the uplink transmitter compression can be seen when the IF drive level applied to the upconverter corresponds to an E_b/N_o level greater than 14dB. At that point, the BER performance flattens out, and increasing the carrier power drive level to the uplink upconverter does not improve the system BER.

Table 4.10 Spread Spectrum through ACTS Measured BER Data

E_b/N_o	data #1	data #2	data #3	data #4	data #5	std. dev.	Average
14.1dB	4.8E-07	1.6E-07	2.6E-07	5.3E-07	5.6E-07	1.59E-07	3.59E-07
13.1dB	4.5E-06	1.6E-06	1.1E-06	2.3E-06	2.3E-06	1.16E-06	2.11E-06
12.1dB	4.0E-05	1.1E-05	1.1E-05	1.3E-05	1.4E-05	1.12E-05	1.55E-05
11.1dB	1.8E-04	6.2E-05	6.2E-05	5.6E-05	6.4E-05	4.77E-05	7.57E-05
10.1dB	5.9E-04	3.3E-04	3.7E-04	2.6E-04	2.9E-04	1.17E-04	3.52E-04
9.1dB	2.0E-03	1.3E-03	1.4E-03	1.1E-03	7.9E-04	4.00E-04	1.26E-03
8.1dB	7.2E-03	5.3E-03	6.3E-03	3.9E-03	3.7E-03	1.35E-03	5.11E-03
7.1dB	1.5E-02	1.1E-02	1.2E-02	8.8E-03	1.1E-02	2.01E-03	1.14E-02
6.1dB	3.1E-02	2.6E-02	2.5E-02	1.9E-02	2.1E-02	4.18E-03	2.40E-02
5.1dB	4.7E-02	4.8E-02	4.8E-02	3.7E-02	3.5E-02	5.76E-03	4.26E-02

Table 4.11 Non-Spread Spectrum through ACTS Measured BER Data

E_b/N_o	data #1	data #2	data #3	data #4	data #5	std. dev.	Average
14.1dB	1.10E-07	3.20E-08	2.30E-08	3.80E-08	3.80E-08	3.14E-08	4.11E-08
13.1dB	1.30E-06	3.70E-07	5.20E-07	9.20E-07	7.60E-07	3.24E-07	7.06E-07
12.1dB	6.90E-06	2.30E-06	7.90E-06	4.00E-06	6.00E-06	2.02E-06	4.96E-06
11.1dB	5.60E-05	1.90E-05	5.60E-05	2.30E-05	1.20E-05	1.89E-05	2.77E-05
10.1dB	2.40E-04	1.40E-04	2.40E-04	1.30E-04	8.40E-05	6.27E-05	1.55E-04
9.1dB	9.40E-04	5.10E-04	9.60E-04	6.30E-04	5.00E-04	2.03E-04	6.80E-04
8.1dB	4.30E-03	2.80E-03	5.10E-03	2.80E-03	2.10E-03	1.11E-03	3.25E-03
7.1dB	9.10E-03	6.80E-03	1.10E-02	7.30E-03	8.50E-03	1.48E-03	8.42E-03
6.1dB	1.90E-02	1.60E-02	2.20E-02	1.50E-02	1.60E-02	2.58E-03	1.74E-02
5.1dB	3.50E-02	3.10E-02	4.30E-02	3.40E-02	2.80E-02	5.04E-03	3.38E-02

Table 4.12 Spread Spectrum Loopback Measured BER Data

E_b/N_o	data #1	data #2	data #3	data #4	data #5	std. dev.	Average
13.6dB	5.7E-08	3.8E-08	4.1E-08	4.6E-08	6.4E-08	9.83E-09	4.82E-08
12.6dB	1.0E-06	1.4E-06	1.1E-06	1.6E-06	1.2E-06	2.15E-07	1.24E-06
11.6dB	2.5E-05	1.7E-05	1.6E-05	2.1E-05	1.8E-05	3.26E-06	1.91E-05
10.6dB	1.0E-04	1.6E-04	1.4E-04	1.4E-04	1.3E-04	1.96E-05	1.32E-04
9.6dB	4.7E-04	3.1E-04	6.9E-04	6.3E-04	6.3E-04	1.39E-04	5.25E-04
8.6dB	3.3E-03	1.7E-03	2.0E-03	1.8E-03	1.9E-03	5.89E-04	2.07E-03
7.6dB	5.0E-03	5.1E-03	5.7E-03	5.4E-03	5.5E-03	2.58E-04	5.33E-03
6.6dB	1.6E-02	1.3E-02	1.4E-02	1.3E-02	1.3E-02	1.17E-03	1.38E-02
5.6dB	2.7E-02	2.8E-02	3.0E-02	2.9E-02	2.8E-02	1.02E-03	2.84E-02
4.6dB	4.8E-02	5.2E-02	5.1E-02	5.1E-02	5.0E-02	1.36E-03	5.04E-02

Table 4.13 Non-Spread Spectrum Loopback Measured BER Data

E_b/N_o	data #1	data #2	data #3	data #4	data #5	std. dev.	average
13.6dB	2.4E-08	2.3E-08	2.5E-08	1.7E-08	1.6E-08	3.74E-09	2.06E-08
12.6dB	3.0E-07	2.6E-07	3.3E-07	3.6E-07	5.1E-07	8.57E-08	3.43E-07
11.6dB	6.0E-06	5.6E-06	5.3E-06	6.3E-06	6.8E-06	5.25E-07	5.98E-06
10.6dB	6.0E-05	6.4E-05	5.5E-05	6.9E-05	6.6E-05	4.87E-06	6.26E-05
9.6dB	3.5E-04	3.1E-04	3.1E-04	3.3E-04	5.5E-04	9.12E-05	3.61E-04
8.6dB	9.8E-04	1.0E-03	1.1E-03	1.1E-03	1.1E-03	5.43E-05	1.05E-03
7.6dB	2.7E-03	3.5E-03	3.5E-03	3.7E-03	3.8E-03	3.88E-04	3.42E-03
6.6dB	6.6E-03	9.2E-03	9.3E-03	9.4E-03	9.7E-03	1.13E-03	8.76E-03
5.6dB	1.4E-02	2.2E-02	2.1E-02	2.2E-02	2.2E-02	3.12E-03	1.99E-02
4.6dB	2.4E-02	4.1E-02	3.9E-02	4.1E-02	4.1E-02	6.65E-03	3.65E-02

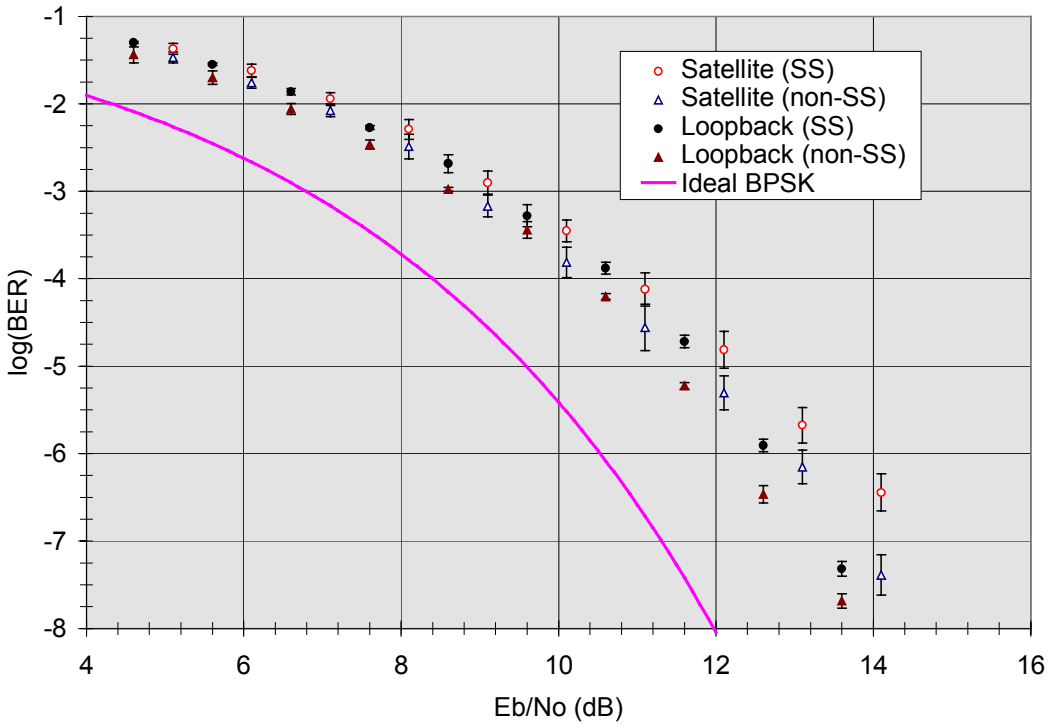

Figure 4.32 Theoretical and Measured CDMA Modem BER Performance

4.3.2 BER Performance versus Scintillation Intensity

Measurements were made of BER through the satellite while the downconverted pilot carrier was recorded on a video cassette recorder for later processing. The modem attenuator was set so that the clear-air E_b/N_o was approximately 12.1dB. The pilot carrier level was about 10dB below the spread spectrum carrier level to minimize interference effects. This carrier was analyzed using the same processing that was used for the beacon carrier. Amplitude and phase spectra were computed over fifteen second intervals, then averaged over five minutes to determine the mean scintillation deviations. The cumulative BER was recorded over the same five minute intervals.

The measured BER values were corrected for variations in the measured C/N on the pilot carrier signal. From the FFT of the carrier, the total carrier power is determined by summing the frequency bins (500 points) containing the peak, and the two sidebands on either side. The C/N for a given five minute interval is then compared to the long-term average level to determine the deviation. This deviation in the carrier C/N is assumed to be the same as the deviation of the modem E_b/N_o from the expected 12.1dB level. The actual BER performance curves for the spread and unspread tests were approximated using the general form

$$\mathrm{BER} = a * \mathrm{erfc}\left(b\sqrt{E_b/N_o}\right), \tag{4.3}$$

where a and b are unknown coefficients. The coefficients were determined by minimizing the least-square error of the logarithm of the BER between Equation 4.3 and the measured

points in Table 4.7 and Table 4.8. The data for E_b/N_o of 14.1dB was not used in this process due to the effects of amplifier compression on the measurements. The spread-spectrum performance of this system was found to be best approximated by

$$BER_{SS} = 0.572\,\mathrm{erfc}(0.737\sqrt{E_b/N_o}), \tag{4.4}$$

while the non-spread-spectrum performance is given by

$$BER_{non-SS} = 0.526\,\mathrm{erfc}(0.774\sqrt{E_b/N_o}). \tag{4.5}$$

The measured BER values were corrected by multiplying by the ratio of the measured BER baseline at the 12.1 E_b/N_o and the BER value calculated from the deviation of the carrier level using Equations 4.3 and 4.4.

From July through December of 1997, over thirty hours of data were recorded and processed. The results from 200 five minute intervals are presented here. Plots have been generated that compare the measured BER, and the amplitude and phase scintillation deviations. During December, some of the measurements were performed with the modem spreading disabled to determine if there was any performance differences between spread and unspread waveforms. Figure 4.33 shows the amplitude scintillation deviation plotted versus the measured BER (corrected for C/N variations) from July, while Figure 4.34 shows the phase scintillation deviation versus BER for the same period. The data for December are plotted in Figure 4.35 and Figure 4.36.

The data in all four plots show that the scintillation intensity varied over a broad range, and there was substantial variation in the measured BER as well. But when the measured BER was corrected for the measured C/N, the variation in BER was reduced to less than two orders of magnitude. The plots of amplitude variation versus BER all show a decreasing BER with increasing scintillation strength. The least-squares method was used to fit lines to the amplitude data, and these are shown on the plots for reference. For the data from July, the best-fit line has the equation

$$\log(\mathrm{BER}_{\mathrm{SS}})_{\mathrm{Jul}} = -3.17\sigma_{\chi} - 4.93. \tag{4.6}$$

The best-fit equation for the SS data from December is

$$\log(\mathrm{BER}_{\mathrm{SS}})_{\mathrm{Dec}} = -3.38\sigma_{\chi} - 3.32, \tag{4.7}$$

and for the non-SS data, the best-fit line is

$$\log(\mathrm{BER}_{\mathrm{non-SS}})_{\mathrm{Dec}} = -3.93\sigma_{\chi} - 3.71. \tag{4.8}$$

All three equations have remarkably similar slopes. Roughly speaking, a 0.1dB increase in the mean amplitude deviation leads to a reduction in the BER by a factor of slightly more than two. This is consistent with the theoretical predictions of Alouini et. al. (24), demonstrating that the performance of a high-margin system is enhanced by the presence of scintillation.

However, there is no strong relationship in the phase scintillation data, and the observed BER is uncorrelated to the phase scintillation strength. Additionally, the December data show that there is approximately a 0.5dB difference between the performance of the spread and unspread waveforms. This result correlates well with the measured performance of the modem in spread and unspread modes.

Another product from this data set is a comparison of the amplitude and phase deviations. Figure 4.37 is a plot of amplitude deviation versus phase deviation for the July and August data, and the September data are shown in Figure 4.38. It is interesting to note that there is little correlation between the amplitude and phase scintillation strength. This is most likely due to different scales of turbulence affecting the transmissions. Phase scintillation is more dependent on large turbulent eddies, while smaller disturbances can result in amplitude scintillation. Also, amplitude scintillation is most intense when the Fresnel frequency is at or below the resolution of the measurement, but in this situation, phase scintillation is usually not detected.

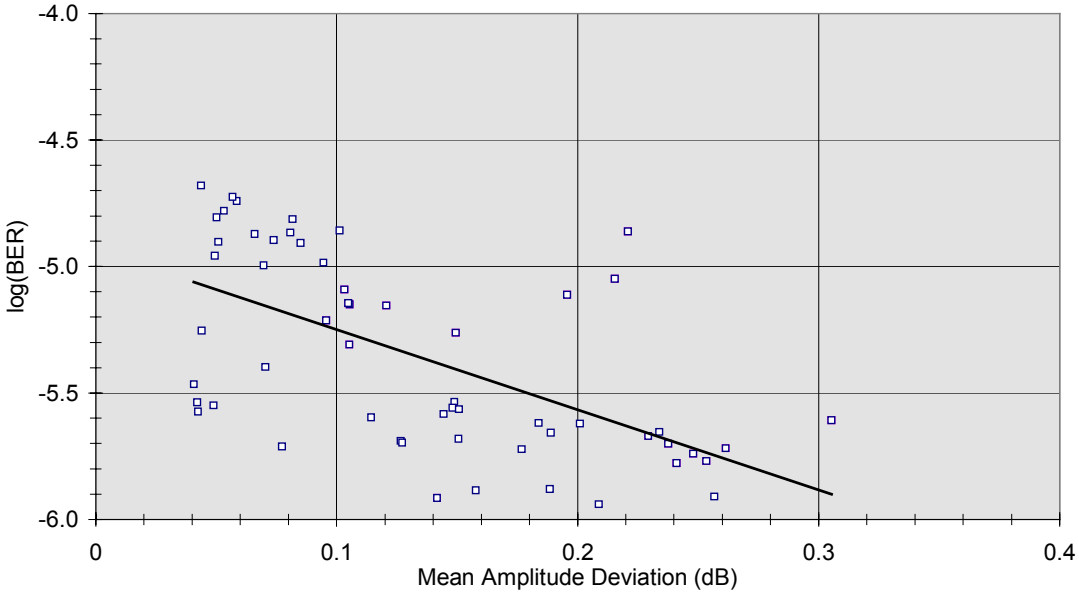

Figure 4.33 Amplitude Scintillation Intensity vs. BER, July and August

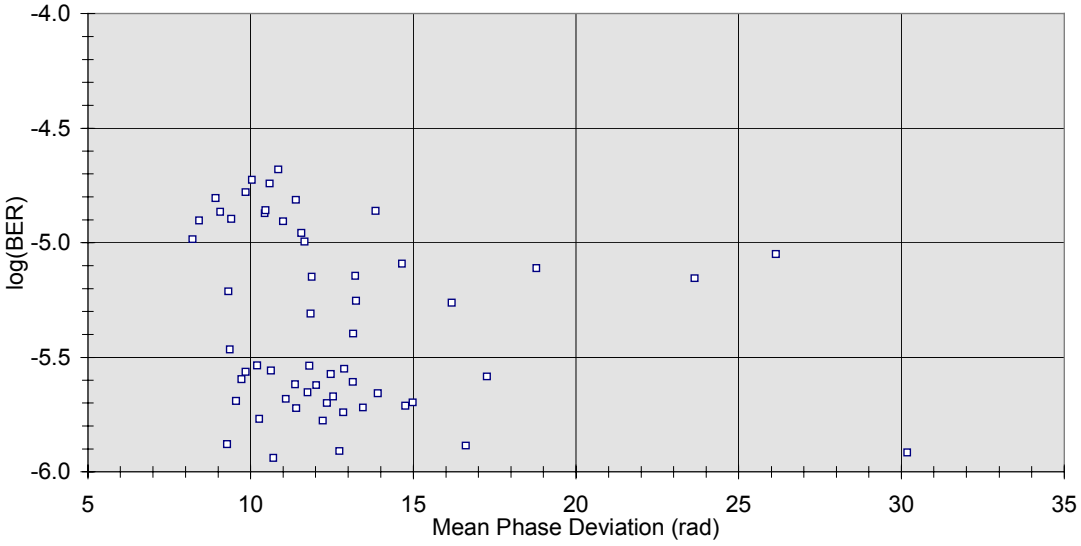

Figure 4.34 Phase Scintillation Intensity vs. BER, July

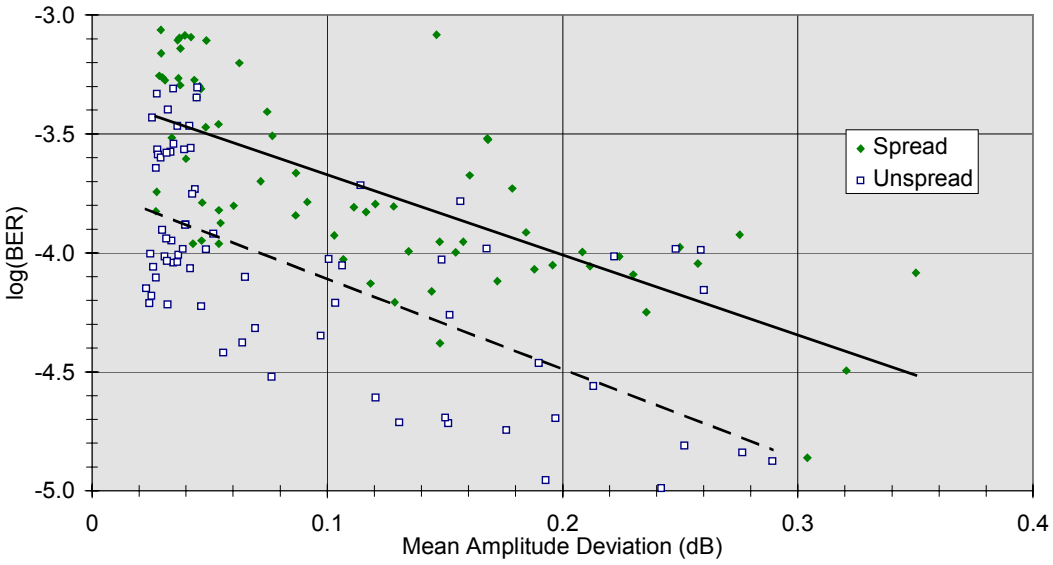

Figure 4.35 Amplitude Scintillation Intensity vs. BER, December

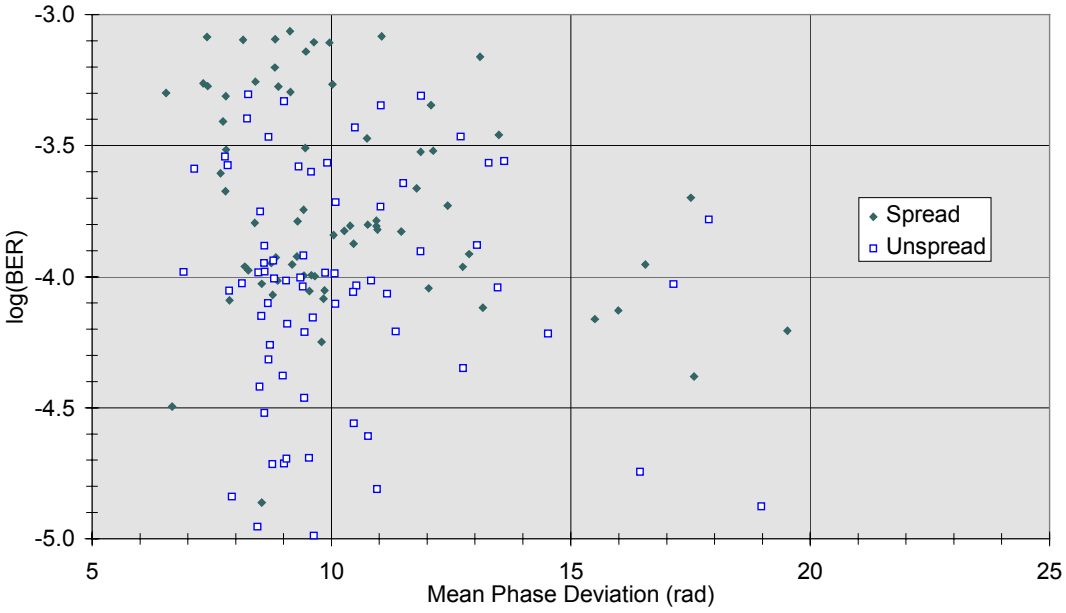

Figure 4.36 Phase Scintillation Intensity vs. BER, December

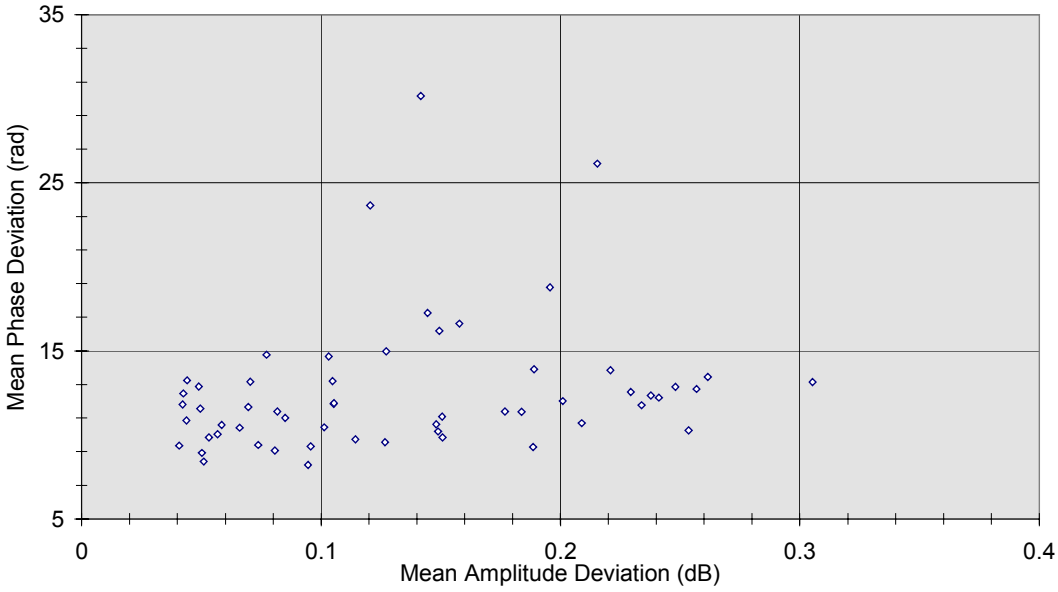

Figure 4.37 Amplitude vs. Phase Scintillation Intensity, July

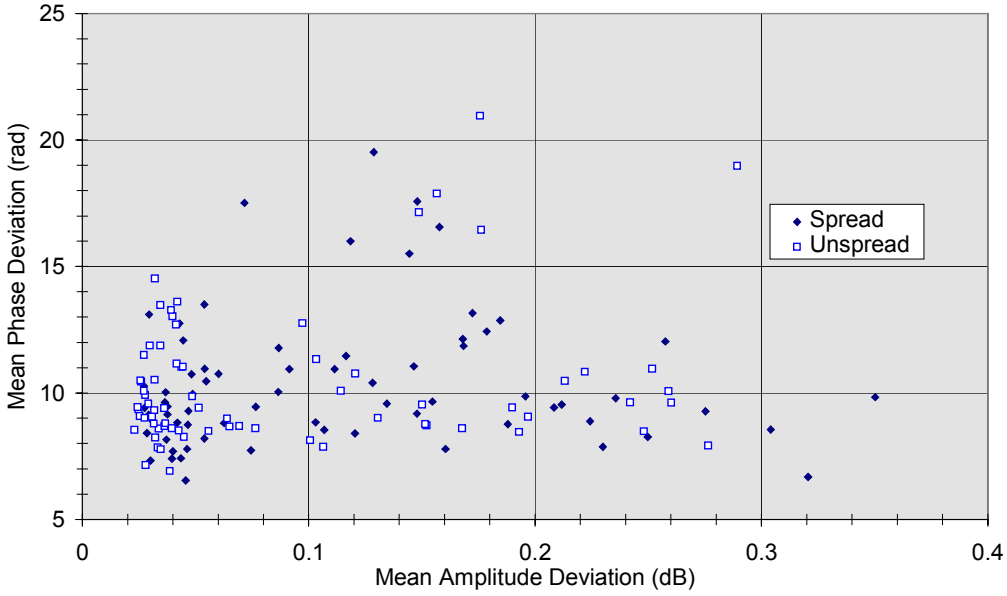

Figure 4.38 Amplitude vs. Phase Scintillation Intensity, December

4.4 Discussion of Measurement Results

Both of the goals of these measurements have been achieved. Carrier measurements have quantified the amplitude scintillation present with the Ka-band ACTS system, and have verified the presence of phase scintillation as well. This is the first reported measurement of tropospheric phase scintillation in a space-to-earth satellite link. Measurements of the BER of digital signals transmitted through ACTS have confirmed that amplitude scintillation does affect the performance of the digital demodulator.

The beacon and carrier loopback measurements produced similar amplitude scintillation results when the five-minute averages were compared. The average of the mean amplitude deviations was near 0.1dB for both types of measurements. The noise floor for the carrier loopback measurements was lower due to the increased carrier power, but otherwise the results were the same as what was observed on the ACTS beacon. The most extreme cases of amplitude scintillation observed were in the range of 0.4-0.5dB.

Enhanced low-frequency phase noise was observed during both beacon and carrier loopback measurements, indicating the presence of phase scintillation. The overall phase noise level was lower for the carrier loopback measurement, again due to the increased carrier power. The actual phase variance measured is very dependent on the total sampling time used for the FFT. All of the measurements presented here represent 15 second sampling time averaged over five minutes. For the loopback measurements, the average of the mean phase deviations was near 10rad, but the most extreme cases were near 30rad.

For the weaker beacon signal, the most extreme phase deviations measured were near 250rad.

The BER measurements conducted concurrently with carrier scintillation measurements demonstrate that there is a dependence between the strength of the amplitude variations and the observed BER. The relatively weak amplitude scintillation observed in this experiment actually improves the modem BER performance. The reason for this lies in the asymmetry of the BPSK performance curve for BER versus E_b/N_o. During scintillation, the C/N (and thus E_b/N_o) varies equally above and below the mean value. But the increase in BER for a given reduction in C/N is less than the decrease in BER for that same improvement in the C/N. When averaged, the net effect is to improve the BER of the system. The relationship is roughly linear, with the BER being reduced by a factor of two for each 0.1dB increase in the mean amplitude deviation of the scintillation. For the range of scintillation measured in this experiment, there is an order of magnitude improvement in the BER due to scintillation. This general trend is consistent with theoretical predictions of a reduction in link outage time in the presence of scintillation for a high-margin VSAT system (24). The difference in performance for spread spectrum versus non-spread waveforms is constant with variations in the mean amplitude deviation. This indicates that the difference in modem processing loss between spread and non-spread waveforms is not affected by the presence or the strength of scintillation.

When the BER variations are compared to phase scintillation strength, there is no apparent relationship. Based on these data, it can be concluded that the phase-locked loop

in the digital demodulator accurately tracks out the slow variations in phase, regardless of their magnitude. Despite the fact that these experiments have demonstrated that there is tropospheric phase scintillation on Ka-band satellite links, it appears that this phenomenon is not an issue in the transmission of digital signals from geostationary satellites.

CHAPTER V

5. SCINTILLATION IN LEO SATELLITE SYSTEMS

Scintillation is created when turbulent regions of the atmosphere (where air masses are mixing) pass though the signal propagation path. The faster these turbulent eddies move through the beam, the more intense the scintillation which is observed. For a GEO satellite system and a fixed ground station, the motion of the turbulence is caused solely by the prevailing winds. But for an LEO satellite or a mobile ground station, the propagation path will move with respect to the atmosphere, adding another component to the velocity of the turbulence. In many cases, this induced motion is much greater than motion generated by atmospheric winds.

A two-part analysis is used to characterize the scintillation which would be expected in a LEO system. First, orbital mechanics is used to compute the motion of the propagation path through the turbulent regions based on the motion of a LEO satellite communicating with a fixed ground station. Once the range of velocities is determined, this is applied to the theoretical and measured scintillation spectra for a GEO system to provide an estimate of the expected LEO scintillation.

5.1 Motion of the Propagation Path in LEO Satellite Systems

As discussed in Section 2.3, the bandwidth of the scintillation spectrum is directly proportional to the mean velocity of the turbulent flow through the propagation path. For a GEO satellite system like ACTS, the satellite remains fixed relative to the ground station, so this velocity is solely due to the prevailing winds in the turbulent layer. In a LEO satellite system, the motion of the satellite with respect to the ground causes the propagation path to move through the atmosphere. This can increase the bandwidth of the scintillation spectrum, as well as the changing the scintillation intensity.

The motion of the propagation path can be modeled by considering the simple case of a LEO satellite in a polar orbit passing over a ground station. The satellite is assumed to be moving in a circular orbit from north to south over an Atlanta-based ground station. Using orbital mechanics, the location of the subsatellite point (where the satellite is directly overhead) may be computed as a function of time. Then, the azimuth and elevation angles from the ground station to the satellite are calculated, and these may be used to compute the motion of the propagation path over time.

The orbital period T for a circular orbit around the Earth is given by (26)

$$T = 2\pi\sqrt{\frac{r_s^3}{\mu}}, \tag{5.1}$$

where r_s is the radius of the orbit and μ is Kepler's constant for the earth (3.9861×10^5 km^3/sec^2). The orbital radius r_s is the sum of the mean radius of the earth (about 6370km)

and the average altitude of the satellite. For a satellite orbiting 700km above the ground, the orbital period is 98.6 minutes, while a satellite which has an altitude of 300km will orbit the earth in 90.4 minutes. The angular velocity of the satellite in rad/sec is given by $2\pi/T$. Since the satellite is in a polar orbit, the angular velocity corresponds to the rate of change in the latitude of the subsatellite point. The change in the longitude of the subsatellite point is solely due to the rotation of the earth (7.27×10^{-5} rad/sec).

To calculate the elevation angle, the central angle γ is first computed. The central angle is the angle between the vectors leading to the satellite and the ground station from the center of the earth. It is defined in terms of the earth station north latitude L_e and west longitude l_e and the subsatellite point north latitude L_s and west longitude l_s as (26)

$$\cos(\gamma) = \cos(L_e)\cos(L_s)\cos(l_s - l_e) - \sin(L_e)\sin(L_s)\,. \tag{5.2}$$

The distance d from the earth station to the satellite is given by (26)

$$d = r_s\left[1 + \left(\frac{r_e}{r_s}\right)^2 - 2\left(\frac{r_e}{r_s}\right)\cos(\gamma)\right]^{\frac{1}{2}}, \tag{5.3}$$

where r_e is the radius of the earth, and r_s is the radius of the satellite orbit. The elevation angle may then be found using (26)

$$\cos(El) = \frac{r_s \sin(\gamma)}{d}. \tag{5.4}$$

The geometry of the elevation angle computation is shown in Figure 5.1.

The azimuth angle is defined in terms of the angle α, the azimuth offset from the longitude line, which is defined by (26)

$$\alpha = \sin^{-1}\left[\frac{\sin|l_e - l_s|}{\sin\gamma}\right]. \tag{5.5}$$

To find the azimuth angle from α, the direction of the satellite from the ground station must be known. The formulas for azimuth in the four quadrants are listed in Table 5.1.

Once the elevation and azimuth angles to the satellite are known as a function of time, it is relatively simple to compute the motion of the propagation path through a turbulent layer. The layer is assumed to be at a height h above the ground at the 'subturbulence point.' The distance from the ground station to the subturbulence point is h/tan(El), neglecting the effect of the earth's curvature. The x-y coordinates of the subturbulence point relative to the ground station are

$$x = h\left(\frac{\cos(Az)}{\tan(El)}\right) \tag{5.6}$$

$$y = h\left(\frac{\sin(Az)}{\tan(El)}\right). \tag{5.7}$$

From the motion of the subturbulence point, it is easy to find the translational velocity of the propagation path though the turbulence.

A few examples based on existing or proposed LEO satellites illustrate the range of path velocities which are possible. The Teledesic Ka-band satellite system will utilize 288 satellites in polar orbits at an average altitude of 700km. Ground station elevation angles are constrained to be greater than 40°. If the satellite passes directly over the ground station, it will spend about 200 seconds above 40° in elevation. The height of the turbulent layer will vary with local atmospheric conditions, so the simulation was performed with altitudes of 1km, 2km, and 4km. For a turbulent layer at an altitude of 2km, the propagation path moves through the layer at 20-30m/sec, while at 4km the path is moving at 40-55m/sec. Figure 5.2 shows the path velocity as a function of time for each altitude, along with the elevation and azimuth angles to the satellite.

Another example was calculated assuming a satellite altitude of 300km. This is approximately the altitude used in most manned space flights. In this case, the satellite is moving much faster with respect to the ground. Over 200 seconds, the satellite goes from below 20° in elevation to passing overhead and back to a 20° elevation angle. Again, the simulation was run with turbulent altitudes of 1km, 2km, and 4km, and the results are plotted in Figure 5.3. In the most extreme situation where the turbulence is at 4km and the elevation is 20°, the path velocity is over 160m/sec.

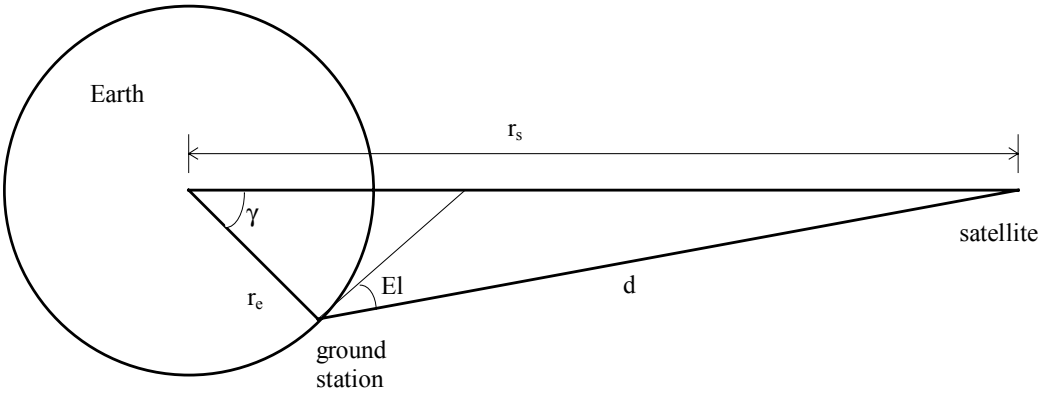

Figure 5.1 Elevation Angle Geometry

Table 5.1 Computing Azimuth Angle from α

Direction	Azimuth
Satellite NE of Ground Station	$Az = \alpha$
Satellite NW of Ground Station	$Az = 2\pi - \alpha$
Satellite SE of Ground Station	$Az = \pi - \alpha$
Satellite SW of Ground Station	$Az = \pi + \alpha$

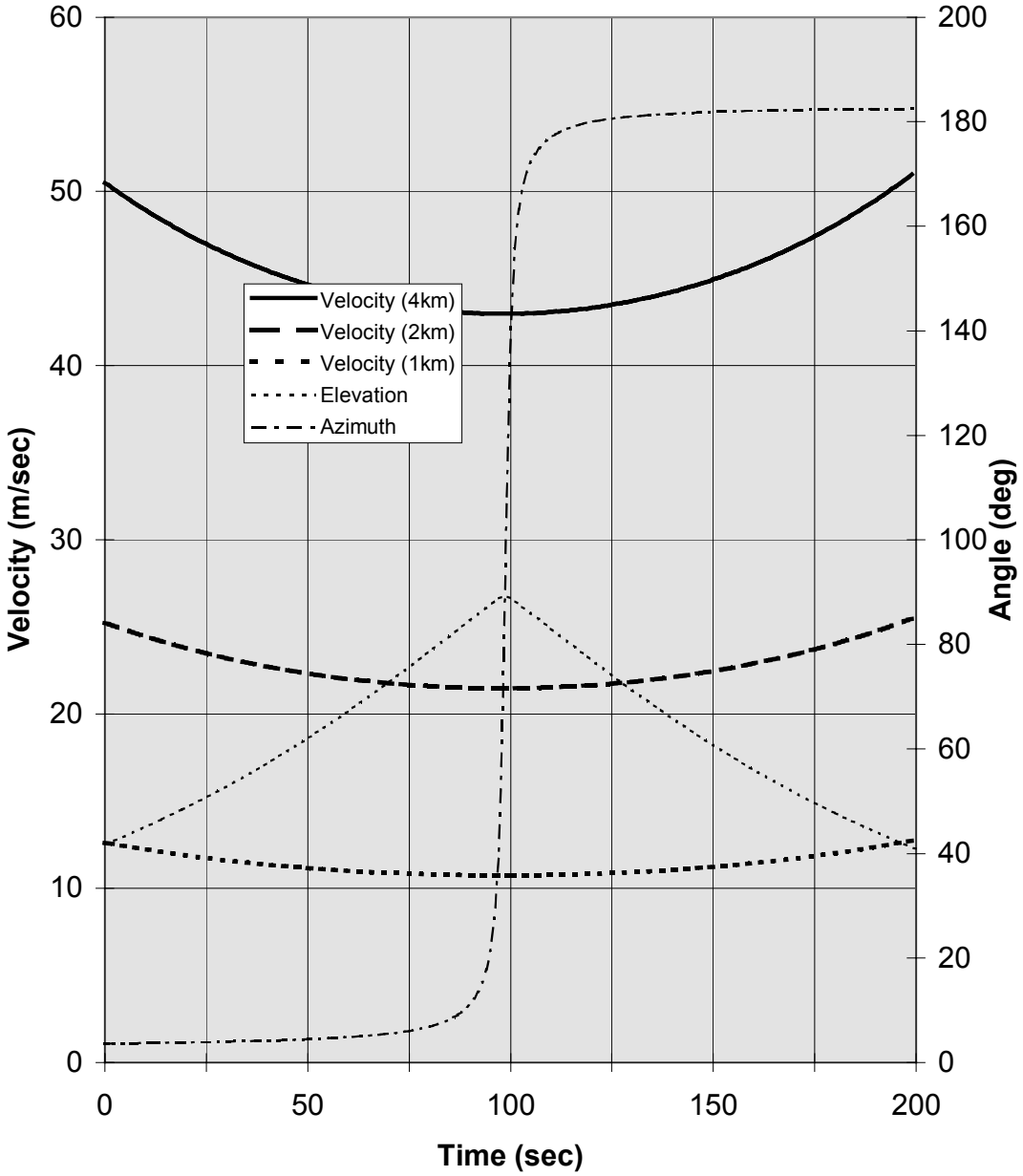

Figure 5.2 Path Velocity Through Turbulence for a 700km LEO

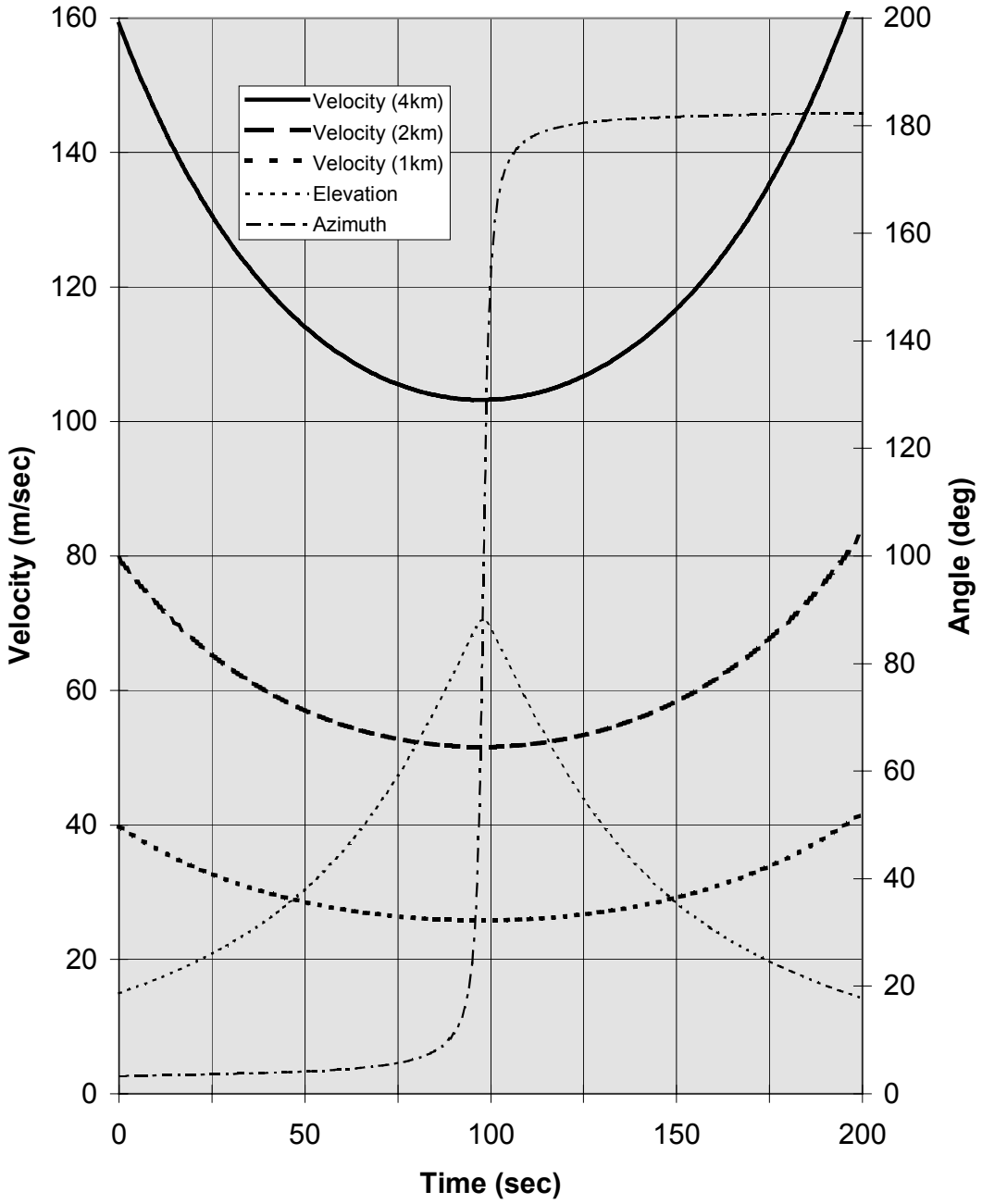

Figure 5.3 Path Velocity Through Turbulence for a 300km LEO

5.2 Effects of Satellite Motion on Scintillation Spectra

The motion of the satellite with respect to the ground station can enhance scintillation effects in several different ways. The velocity of the turbulent flow, the distance from the ground station to the turbulent layer, and the perceived intensity of the turbulence may all be affected. The velocity and distance discrepancies affect the scintillation spectrum, while changes in the turbulent intensity affect the scintillation magnitude.

The velocity of the turbulent flow through the propagation path has two components: the mean wind velocity of the turbulent layer and the velocity of the propagation path through the turbulent layer. The net velocity of the turbulence is the vector sum of these two components. If the propagation path is moving in the opposite direction of the mean wind, then the magnitudes of the two effects will add. The wind velocity in the lower troposphere is typically on the order of 10m/sec, and it can reach speeds near 50m/sec in extreme conditions. The simulations presented in the previous section demonstrated that the propagation path velocity can be as much as an order of magnitude greater than the wind velocity.

In addition to the variation in the velocity of the turbulence, the distance to the turbulent layer will also vary as the satellite moves; even if the layer is at a constant altitude. As the path length between the ground station and the turbulence increases, the Fresnel frequency decreases. Conversely, as the velocity of the turbulence through the propagation

path increases, the Fresnel frequency increases. Figure 5.4 shows how the Fresnel frequency varies for a 30GHz transmission as a function of the velocity of the turbulence though the propagation path and distance from the ground station to the turbulence. Note that higher velocities tend to occur at only at longer distances, so the very high Fresnel frequencies shown in the figure for the combination of short path distances and high turbulent velocities are rarely encountered in practice.

From scintillation theory, the intensity of the scintillation is related to the severity of the turbulence through the structure constant C_n. For a GEO satellite system, it is generally assumed that the turbulence structure varies much more slowly than the scintillation. But for a LEO system, the propagation path can move through many different zones of turbulent intensities, and the validity of this assumption is questionable. The net effect of this variation in C_n is to increase the overall intensity of the observed scintillation.

The LEO satellite system poses a challenge to receiver systems. The antennas used must be less directional than those used in GEO systems. Therefore the received signal will be weaker, and will also be constantly varying if tracking is not used. The motion of the satellite will also impart a Doppler shift to the transmitted signal, requiring frequency tracking. Excessive scintillation in LEO satellite systems is just one more impairment that must be overcome in the design of a successful system.

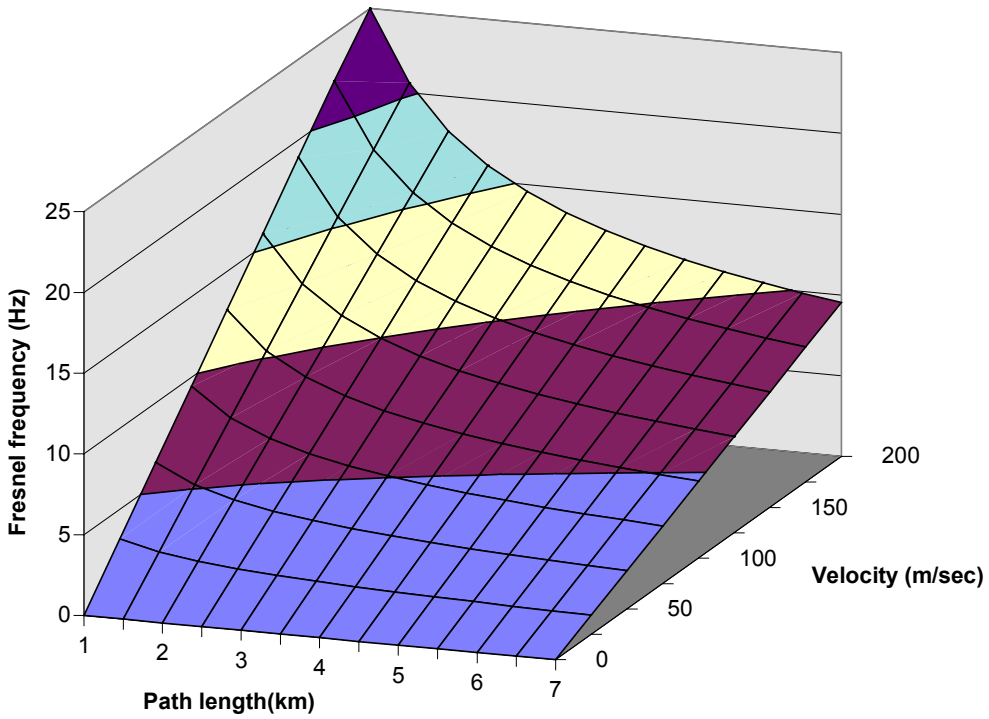

Figure 5.4 Fresnel Frequency vs. Turbulence Velocity and Distance

5.3 Applying ACTS Measurements to a LEO Environment

Estimates of the scintillation spectra for a LEO satellite system may be obtained by extrapolating from the measurements of scintillation on the ACTS propagation beacon presented in section 4.1. From each amplitude spectra plot, the low frequency magnitude, W_χ^0, and the Fresnel frequency, f_o, can be determined. Equations 2.12 and 2.13 for the amplitude scintillation spectrum can be written in terms of the Fresnel frequency as

$$W_\chi^0(f) = 87.17 \frac{C_n^2 L^{11/6}}{\lambda^{7/6}} \left(\frac{1}{f_o}\right) \quad dB^2/Hz, \quad (\text{as } f \to 0), \tag{5.8}$$

$$W_\chi^\infty(f) = 224.6 \frac{C_n^2 L^{11/6}}{\lambda^{7/6}} \left(\frac{f_o^{5/3}}{f^{8/3}}\right) \quad dB^2/Hz, \quad (\text{as } f \to \infty). \tag{5.9}$$

The wavelength of the transmission, λ, is known (0.0149m for the ACTS beacon), leaving the only unknown quantity the product $C_n^2 L^{11/6}$, given by

$$C_n^2 L^{11/6} = 0.01147 W_\chi^0 \lambda^{7/6} f_o \ m^{7/6}. \tag{5.10}$$

Similarly, knowing the Fresnel frequency and the wavelength, the product $vL^{-1/2}$ can be determined by rearranging Equation 2.11 as

$$v/\sqrt{L} = f_o \sqrt{2\pi\lambda} \ m^{1/2}/sec. \tag{5.10}$$

Based on the measurements performed, both the turbulent intensity and the transverse velocity can be computed as a function of the path length L. Computed values for $C_n^2L^{11/6}$ and $vL^{-1/2}$ are given in Table 5.2 for some of the beacon amplitude spectra measurements which are presented in section 4.1.

The path length through the turbulent layer, L, can not be measured directly with this experiment. However it can be estimated. The altitude at the top of the turbulent boundary layer of the troposphere is in the range of 0.5km to 5km. For the ACTS system at a elevation angle of 47.3° from Atlanta, this corresponds to path length range of 0.74km to 7.4km. For the purpose of simulating the effects of scintillation on a LEO system, three different altitudes were assumed. Simulations were performed with turbulent layers at 1km, 2km, or 4km. Three sets of parameters from Table 5.2 were are presented here. Case 1 is the data from 3/13 (15:20), case 2 is the 4/17 (14:34) data, and for case 3 the 6/24 (20:42) data was used.

As in the previous section, the altitude of the satellite was assumed to be either 300km or 700km. The turbulent intensity, C_n, was assumed to be constant throughout the boundary layer. This may not be an accurate assumption, but in the absence of information about the spatial distribution of C_n, this allows the computation of a first approximation to the expected scintillation effects. If variations in C_n do exist, then the observed scintillation would be enhanced. The wavelength used was 0.01m, which corresponds to the transmit frequency of 30GHz.

The mean amplitude scintillation deviation varies with elevation angle, and is highest when the elevation is the lowest. The mean deviation does not depend on the height of the turbulent layer, but the Fresnel frequency and the spectral intensity, W_{χ}^{0}, do vary with both the layer height and elevation angle. The Fresnel frequency is maximum when the elevation angle and layer height are highest and the angular speed of the satellite is the greatest. The spectral intensity varies inversely with the Fresnel frequency. The next two figures show how the strength of the amplitude scintillation, in terms of the mean amplitude deviation, varies with the motion of the satellite for the three cases selected. Figure 5.5 shows how the mean amplitude deviation varies for a 700km LEO satellite, and the variation of the deviation for a 300km LEO is shown in Figure 5.6. The following two figures show the changes in the Fresnel frequency for different layer heights using the case 3 atmospheric parameters. Figure 5.7 shows the Fresnel frequency versus satellite motion for a 700km LEO, and Figure 5.8 shows the Fresnel frequency variations for a 300km LEO.

The results of this analysis demonstrate that the scintillation expected for an LEO satellite system is several times that which is observed in a GEO system. The effects are most pronounced for lower elevation angles, while scintillation is reduced when the satellite is directly overhead. Since signal acquisition and handoff between satellites most likely occurs at the lower elevations, and not when the satellite is overhead, this increase in scintillation should be an important design consideration for LEO receivers. The rate of variation in amplitude and phase is greatest as the LEO passes overhead. The Fresnel frequency can be one or two orders of magnitude greater during this peak than the typical GEO value. Even though measurements performed with ACTS showed that phase

scintillation has no effect on system performance, it is possible that the much faster phase variations expected in a LEO system could degrade the performance of the digital demodulator.

For some circumstances, the mean amplitude deviation can go higher than 1.5dB. But this is only the mean deviation, and occasionally scintillation may induce signal variations several times the mean value, perhaps as high a 5dB. While it is difficult to predict how this may affect a digital demodulator, several scenarios are possible. If the system is operating on a relatively low link margin, these drastic drops in signal strength could cause the modem to lose lock on the signal. Sudden increases in signal strength at the satellite could result in distortion problems if the satellite transmitter is operating near the saturation point. And even if the system has adequate margin in both directions, 5dB swings in the carrier level can result in BER variations of three or more orders of magnitude. Carrier variations this extreme can cause difficulties in the initial acquisition of the signal, and could make it difficult for some modems to maintain signal lock.

Table 5.2 Computed Parameters from ACTS Beacon Measurements

Date	Time	W_χ^0 (dB^2/Hz)	f_o (Hz)	Mean (dB)	$vL^{-1/2}$ ($m^{1/2}/sec$)	$C_n^2L^{11/6}$ ($m^{7/6}$)
3/13	11:50	0.002	1.0	0.081	0.306	1.69×10^{-7}
3/13	15:20	0.01	1.0	0.144	0.306	8.48×10^{-7}
4/17	14:34	0.63	0.2	0.458	0.061	1.07×10^{-5}
4/21	12:16	0.005	1.0	0.093	0.306	4.25×10^{-7}
6/18	12:12	0.006	0.8	0.102	0.245	4.28×10^{-7}
6/18	14:37	0.25	0.3	0.332	0.092	6.39×10^{-6}
6/24	13:32	0.013	0.6	0.111	0.184	6.40×10^{-7}
6/24	15:56	0.01	0.4	0.102	0.122	3.39×10^{-7}
6/24	20:42	0.32	0.2	0.313	0.061	5.36×10^{-6}

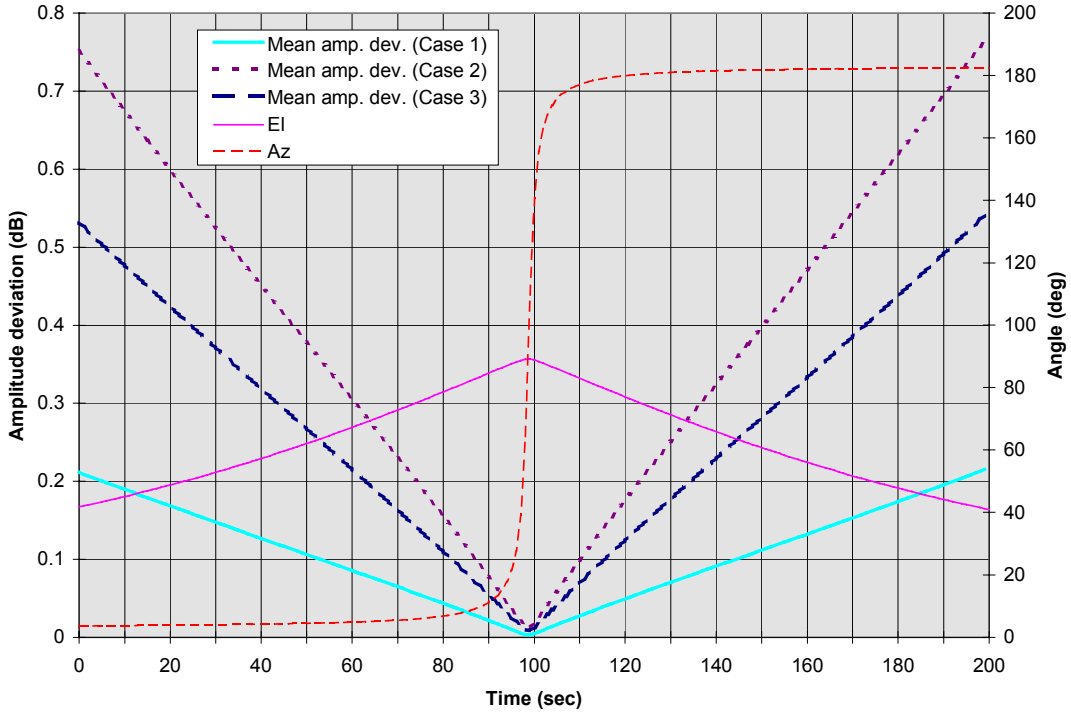

Figure 5.5 Mean Amplitude Deviation for a 700km LEO

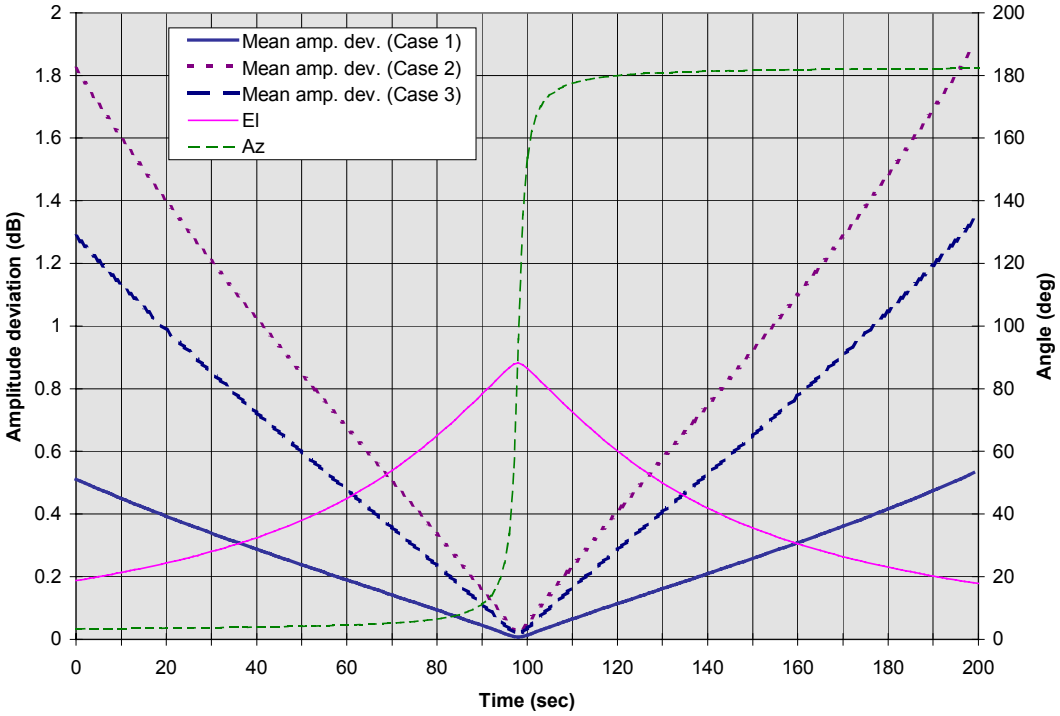

Figure 5.6 Mean Amplitude Deviation for a 300km LEO

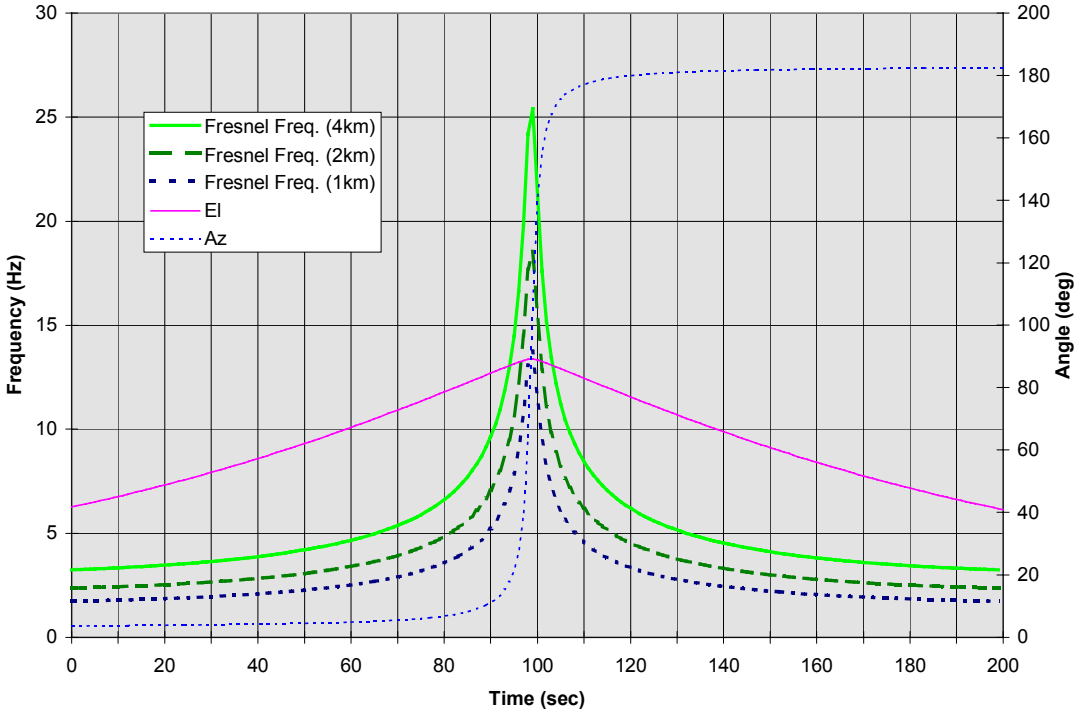

Figure 5.7 Fresnel Frequency versus Layer Height for a 700km LEO

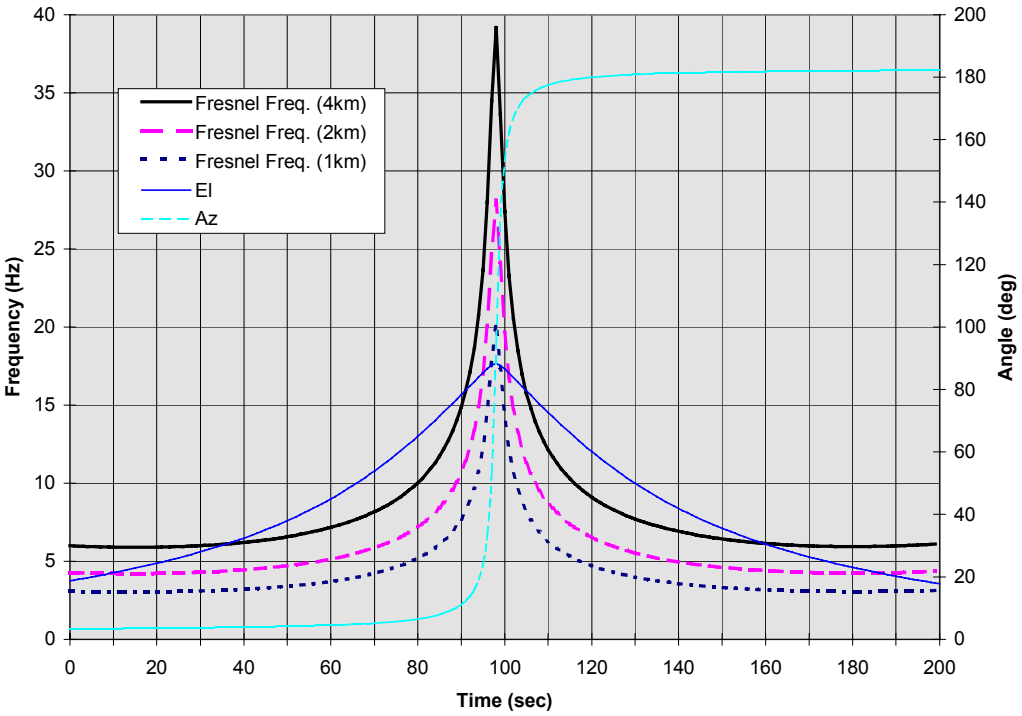

Figure 5.8 Fresnel Frequency versus Layer Height for a 300km LEO

CHAPTER VI

6. SUMMARY AND CONCLUSIONS

The ACTS satellite was launched in order to test new technologies for Ka-band communication systems in geosynchronous orbit. An important component of this investigation is the study of atmospheric propagation at Ka-band frequencies. Many of the impairments associated with atmospheric propagation in satellite systems, such as rain attenuation and amplitude scintillation, are known to be more severe at Ka-band than at lower frequencies. This research has shown that at the higher Ka-band frequencies phase scintillation is enhanced as well.

The goal of this research has been to measure the effects of atmospheric scintillation in Ka-band satellite communications. Two types of measurements have been utilized to characterize the scintillation effects. Amplitude and phase spectra of unmodulated carrier tones were monitored to resolve the differences which occur when scintillation is present. These measurements have verified the presence of amplitude scintillation at Ka-band, and quantified the effects for a typical geostationary satellite system. Additionally, tropospheric phase scintillation has been measured for the first time in a satellite communications link. These measurements confirm theoretical predictions that phase scintillation exists at Ka-band frequencies.

Also, measurements of phase-modulated spread-spectrum signals were performed to watch for degradation in the bit error rate as a result of scintillation. Bit error rate data were compared with data on amplitude and phase scintillation strength to determine if the processes are correlated. The measurements have shown that the weak amplitude scintillation results in an improvement in the bit error rate of a digital signal for a high link margin system due to the asymmetry of the modem performance curve. The same measurements show that there is no correlation in the bit error rates and the measured phase scintillation level, and it is not a concern in Ka-band geostationary satellite systems. The carrier and bit error rate measurements have successfully quantified the effects of Ka-band scintillation in amplitude and phase.

The scintillation effects measured for this geostationary satellite system are relatively weak in comparison to those that would be seen in a communications system with satellites in low-earth orbit. The other unique component of this research is the modeling of the scintillation which would be observed in a low-earth orbiting satellite system. The measurements obtained for the ACTS geostationary system have been applied to the low-earth orbiting environment to obtain estimates of the expected scintillation spectra. The results show that scintillation should be several times stronger in a low-earth orbiting system than the observations obtained with ACTS. These effects become more pronounced as the elevation angle to the satellite decreases. Since signal handoff between satellites in a constellation typically occurs when the satellites are at lower elevation angles, the modems in these systems must be capable of handling intensely scintillating signals. Several

constellations of Ka-band communication satellites in low-earth orbit have been proposed recently, and this data will be useful in the design of these systems.

BIBLIOGRAPHY

[1] F. M. Naderi and S. J. Campanella, *NASA's Advanced Communications Technology Satellite (ACTS): An Overview of the Satellite, the Network, and the Underlying Technologies,* NASA Publication, March 1988.

[2] L. J. Ippolito, *Radiowave Propagation in Satellite Communications*, New York: Van Nostrand Reinhold, 1986.

[3] A. Ishimaru, *Wave Propagation and Scattering in Random Media*, vol. 2, New York: Academic Press, 1978.

[4] E. Vilar and J. Haddon, "Measurement and Modeling of Scintillation Intensity to Estimate Turbulence Parameters in an Earth-Space Path," *IEEE Transactions on Antennas and Propagation*, vol. AP-32, no. 4, 1984.

[5] D. C. Cox, H. W. Arnold, and H. H. Hoffman, "Observations of Cloud-Produced Amplitude Scintillation on 19- and 28-GHz Earth-Space Paths," *Radio Science*, vol. 16, no. 5, 1981.

[6] I. E. Otung and M. S. Mahmoud, "Rain-Induced Scintillation on Satellite Downlinks," *Electronic Letters*, vol. 32, no. 1, 1996.

[7] D. C. Livingston, *The Physics of Microwave Propagation*, Englewood Cliffs, NJ: Prentice-Hall, 1970.

[8] Y. Karasawa and T. Matsudo, "Characteristics of Fading on Low-Elevation Angle Earth-Space Paths with Concurrent Rain Attenuation and Scintillation," *IEEE Transactions on Antennas and Propagation*, vol. 39, no. 5, 1991.

[9] G. K. Batchelor, *The Theory of Homogeneous Turbulence*, Cambridge, England: Cambridge University Press, 1953

[10] R. S. Cole, K. L. Ho, and N. D. Mavrokoukoulakis, "The Effect of the Outer Scale of Turbulence and Wavelength on Scintillation Fading at Millimeter Wavelengths," *IEEE Transactions on Antennas and Propagation*, vol. AP-26, no. 5, 1978.

[11] J. W. Strohbehn, "Line-of-Sight Wave Propagation Through the Turbulent Atmosphere," *Proceedings of the IEEE*, vol. 56, no. 8, 1968.

[12] R. B. Stull, *An Introduction to Boundary Layer Meteorology*, Dordrecht: Kluwer Academic Publishers, 1988.

[13] H. Vasseur and D. Vanhoenacker, "Simulation of Atmospheric Turbulence Effects on Terrestrial Millimeter Wave Links," presented at the 8th International Conference on Antennas and Propagation, 1993.

[14] V. I. Tatarski, *Wave Propagation in a Turbulent Medium*, New York: McGraw-Hill, 1961.

[15] M. S. Alouini, *Impact of the Atmosphere on K_a-band Satellite Communication Systems,* Masters thesis, School of Electrical and Computer Engineering, Georgia Institute of Technology, 1995.

[16] R. K. Crane, "Propagation Effects at Millimeter Wavelengths," presented at the1985 IEEE Military Communications Conference.

[17] J. Haddon and E. Vilar, "Scattering Induced Microwave Scintillations from Clean Air and Rain on Earth Space Paths and the Influence of Antenna Aperture," *IEEE Transactions on Antennas and Propagation*, vol. AP-34, no. 5, 1986.

[18] E. Vilar and H. Smith, "A Theoretical and Experimental Study of Angular Scintillations in Earth Space Paths," *IEEE Transactions on Antennas and Propagation*, vol. AP-34, no. 1, 1986.

[19] W. L. Stutzman and G. A. Thiele, *Antenna Theory and Design*, New York: John Wiley & Sons, 1981.

[20] D. C. Cox, H. W. Arnold, and R. P. Leck, "Phase and Amplitude Dispersion for Earth-Satellite Propagation in the 20- to 30-GHz Frequency Range," *IEEE Transactions on Antennas and Propagation*, vol. AP-28, no. 3, 1980.

[21] W. L. Stutzman, T. Pratt, D. M. Imrich, W. A. Scales, and C. W. Bostian, "Dispersion in the 10-30 GHz Frequency Range: Atmospheric Effects and Their Impact on Digital Satellite Communications," *IEEE Transactions on Communications,* vol. COM-34, no. 3, 1986.

[22] A. Vander Vorst and D. Vanhoenacker, "Propagation Limitations for Transionospheric Systems from 10 to 300 GHz," *AGARD Lecture Series 172: Propagation Limitations for Systems Using Band-Spreading,* NATO Publication, 1990.

[23] D. Vanhoenacker, H. Vasseur, and C. Amaya-Byrne, "Simulation of the Effects of Atmospheric Scintillation on Digital Transmissions at Centimeter and Millimeter Wavelengths," *International Journal of Infrared and Millimeter Waves,* vol. 12, no. 10, 1991.

[24] M. S. Alouini, S. A. Borgsmiller, and P. G. Steffes, "Channel Characterization and Modeling for Ka-band Very Small Aperture Terminals," *Proceedings of the IEEE*, vol. 85, no. 6, 1997.

[25] R. Bauer, "Ka-band Propagation Measurements: An Opportunity with the Advanced Communication Technology Satellite," *Proceedings of the IEEE*, vol. 85, no. 6, 1997.

[26] T. Pratt and C. W. Bostian, *Satellite Communications*, New York: John Wiley & Sons, 1986.

[27] E. Vilar, S. Senin, J. Waight, J. Austin, K. W. Wan, and H. McPherson, "An Experimental mm-wave Receiver System for Measuring Phase Noise due to Atmospheric Turbulence," presented at the 1995 European Microwave Conference.

VITA

Scott A. Borgsmiller was born on May 2, 1967 in Murphysboro, IL. After graduating from Murphysboro High School in 1985, he attended the University of Illinois in Urbana-Champaign, where he received the B.S. degree in electrical engineering in 1989. From 1989 to 1994, he worked at the General Electric/Martin Marietta Ocean and Radar Systems Division in Syracuse, NY. He was in the Edison Engineering Program, and worked in microwave circuit design, sonar systems, and radar software engineering. In 1992, he completed the program and received the M.S. degree in electrical engineering from Syracuse University. From 1992 to 1994, he worked on the integration of the weapon launch system for the Seawolf submarine. Since 1994, he has been a student and graduate research assistant at the Georgia Institute of Technology in Atlanta, working toward the degree of Ph.D. in electrical engineering. His research has involved the characterization of the effects of atmospheric propagation in Ka-band satellite communication systems. After graduation, he will be employed by COMSAT Laboratories in Clarksburg, MD.